University of Texas at El Paso
DigitalCommons@UTEP

Open Access Theses & Dissertations

2018-01-01

Investigation of Material Response to Atmospheric Re-entry Exposure for Sub-structural Ti-6Al-4V, Inconel 718, A-286 and Al 2024 Components Recovered from the Space Shuttle Columbia Accident

Ngozi Chinoyerem Ochoa
University of Texas at El Paso, ngoziochoa@gmail.com

Follow this and additional works at: https://digitalcommons.utep.edu/open_etd

Part of the Materials Science and Engineering Commons, and the Mechanics of Materials Commons

Recommended Citation
Ochoa, Ngozi Chinoyerem, "Investigation of Material Response to Atmospheric Re-entry Exposure for Sub-structural Ti-6Al-4V, Inconel 718, A-286 and Al 2024 Components Recovered from the Space Shuttle Columbia Accident" (2018). *Open Access Theses & Dissertations*. 1501.
https://digitalcommons.utep.edu/open_etd/1501

This is brought to you for free and open access by DigitalCommons@UTEP. It has been accepted for inclusion in Open Access Theses & Dissertations by an authorized administrator of DigitalCommons@UTEP. For more information, please contact lweber@utep.edu.

INVESTIGATION OF MATERIAL RESPONSE TO ATMOSPHERIC RE-ENTRY EXPOSURE FOR SUB-STRUCTURAL Ti-6Al-4V, INCONEL 718, A-286 and Al 2024 COMPONENTS RECOVERED FROM THE SPACE SHUTTLE *COLUMBIA* ACCIDENT

NGOZI CHINOYEREM UBANI OCHOA

Doctoral Program in Materials Science and Engineering

APPROVED:

Stephen Stafford, Ph.D., Chair

Peter Golding, Ph.D.

David Roberson, Ph.D.

Aaron Velasco, Ph.D.

Charles Ambler, Ph.D.
Dean of the Graduate School

Copyright ©

by

Ngozi Chinoyerem Ubani Ochoa

2018

Dedication

In memory of the Space Shuttle *Columbia* STS-107 crew: Payload commander Michael Anderson, Mission Specialists David Brown, Kalpana Chawla and Lauren Clark, Commander Rick Husband, Pilot Willie McCool and Payload Specialist Ilan Ramon.

INVESTIGATION OF MATERIAL RESPONSE TO ATMOSPHERIC RE-ENTRY EXPOSURE FOR SUB-STRUCTURAL Ti-6Al-4V, INCONEL 718, A-286 and Al 2024 COMPONENTS RECOVERED FROM THE SPACE SHUTTLE *COLUMBIA* ACCIDENT

by

NGOZI CHINOYEREM UBANI OCHOA, BA/BS

DISSERTATION

Presented to the Faculty of the Graduate School of

The University of Texas at El Paso

in Partial Fulfillment

of the Requirements

for the Degree of

DOCTOR OF PHILOSOPHY

Department of Metallurgical, Materials and Biomedical Engineering

THE UNIVERSITY OF TEXAS AT EL PASO

May 2018

Acknowledgements

The author would like to thank her dissertation committee and to acknowledge, with sincere gratitude, Dr. Stephen Stafford for introducing her to the field of metallurgy, for his academic support and for the opportunity to participate in *Columbia* research through the Center for the Advancement of Space Safety and Mission Assurance Research (CASSMAR). The author thanks Danny Olivas for his dedication to CASSMAR and she would like to extend her appreciation to her research mentor Darren Cone for his academic guidance.

Funding and support provided by the Louis Stokes Alliance for Minority Participation made this work possible and the author would also like to thank The University of Texas at El Paso Graduate School. Drs. Christopher Bradley, Shalayna Smith and Brenda Machado of Herrera Stafford and Associates provided laboratory and technical support for which the author is indebted.

The author would also like to acknowledge her parents, Rosemond and Ephraim, both of whom serve as great inspirations in her life, continually setting a strong example of humility, hard work and determination. Finally, the author's deepest gratitude is endowed to her beloved husband, Jarrod, for his inexhaustible encouragement, patience and support.

Abstract

Investigations of Space Shuttle *Columbia* debris hold great relevance for understanding material response to re-entry environment in the case of thermal protection system (TPS) compromise. The X_o 582 ring-frame bulkhead and attached payload bay door (PLBD) rollers exhibited highly localized thermal degradation and material loss. This research presents examination of these components that provided a unique opportunity to examine multiple alloy systems located in close proximity of one another. These artifacts were of great interest due to their possible involvement in the thermal event responsible for the char layer deposition discovered on overhead windows. Located adjacent to the PLBD roller and bulkhead, post-accident investigation of the char-layer deposition on overhead windows revealed indications of unexpected material response. Inconsistent with the relative melting temperatures of titanium and aluminum, it was observed that titanium melted and deposited onto the windows before aluminum. The unusual arrangement of the char layer was hypothesized to have occurred due to localized elevated heating and deposition of titanium due to shock-shock interaction or titanium combustion. The latter hypothesis takes central focus of the PLBD roller investigation, as the ignition and

combustion response of titanium in a re-entry environment was previously investigated by arc-jet testing of Ti-6Al-4V plates in simulated low-pressure, high-enthalpy conditions. Researchers observed and classified titanium reactivity, identifying discriminatory behavior among the reacting specimens. Analysis of the PLBD roller revealed features suggestive of titanium combustion and possessed microstructural similarities to the arc-jet specimens that reacted more aggressively to the simulated environment. Observation of the ring-frame bulkhead, and other aluminum debris recovered from the *Columbia* accident, revealed unique delamination features on fracture surfaces. The unique nature of the fracture surface, termed broom-straw fracture, is not broadly described in literature. Examination of the bulkhead substantiated and expanded upon the previous notions that broom-straw fracture is the result of grain boundary liquation and the influence of microstructure and thermo-mechanical processing was postulated. The findings included in this dissertation, along with other post-accident analyses, further demonstrate the critical need for a comprehensive characterization of behavioral properties for reactive aerospace materials in the high-temperature, low-O_2, low-pressure re-entry environment.

Contents

Acknowledgements v

Abstract vi

Contents viii

List of Tables xiii

List of Figures xiv

Chapter 1 Introduction 1

1.1. Space Shuttle *Columbia* Accident 1

1.2. Atmospheric Re-entry 5

1.3. Space Shuttle *Columbia* Debris Hardware 6

1.4. Overview of Ti-6Al-4V, Inconel 718 and A-286 Alloys 12

1.4.1. Titanium and Titanium Alloys 12

1.4.1.1. Titanium Alloy Ti-6Al-4V 16

1.4.2. Superalloy Metallurgy 23

1.4.2.1. Nickel-based Superalloy Inconel 718 25

1.4.2.2. Iron-based Superalloy A-286 25

1.4.3. Aluminum and Aluminum Alloys 26

1.4.3.1. Aluminum Alloy 2024 28

Chapter 2 Literature Review 30

2.1. Post-accident Investigations of Ti-6Al-4V Response to Atmospheric Re-entry 30

2.1.1. Discovered Char Layer Deposits on Overhead Windows 30

2.1.2. Computational Fluid Dynamics Thermal Analysis of Payload Bay Door Rollers 32

2.1.3. Study of Titanium Combustion in Simulated Entry Environments 34

2.2. Broom-straw Fracture & Aluminum Debris Analysis from *Columbia* 37

2.3. Titanium Oxidation 39

2.4. Titanium and Gaseous Nitrogen 44

2.5. Titanium Ignition and Combustion Behavior 45

2.5.1. Temperature Influence on Ignition 46

2.5.2. Added Energy (fracture) Influence on Ignition 48

2.5.3. Gravity Effects 49

2.5.4. Gas Velocity Influence on Ignition 50

2.5.5. Particles in Air Flow 53

Chapter 3 PLBD Roller Examination 57

3.1. Experimental Methods 57

3.1.1. PLBD Roller Surface Characterization 57

3.1.2. PLBD Roller Microstructural Analysis 60

3.1.3. Arc-jet Test Specimen Microstructural Analysis 66

3.2. Results 67

3.2.1. PLBD Roller Surface Analysis 67

3.2.2. PLBD Roller Construction 74

3.2.3. Re-solidified Molten Material (RSMM) 75

3.2.4. Ti-6Al-4V Oxides and α-case Microstructural Analysis 79

3.2.5. Ti-6Al-4V Sleeves Bulk Microstructural Analysis 89

3.2.6. A286 Microstructural Analysis 98

3.2.6.1. A286(A) 98

3.2.6.2. A286(H) 101

3.2.7. IN718 Microstructural Analysis 102

3.2.7.1. IN718(B) and IN718(C) 104

3.2.7.2. CrIN718(D) and IN718(G) 108
3.2.8. Microstructural Analysis of Arc-jet Specimens 112
3.3. Discussion 116
3.3.1. PLBD Roller Surface Features 116
3.3.2. High Temperature Oxidation 118
3.3.3. Geometrical Factors Shown to Influence Ignition 120
3.3.4. Microstructural Analysis 122
3.3.5. Comparison to Arc-jet Specimens 125
3.4. Conclusions 126
Chapter 4 X_o 582 Bulkhead Examination 129
4.1. Experimental Methods 129
4.1.1. X_o 582 Bulkhead Surface Characterization 129
4.1.2. X_o 582 Bulkhead Microstructural Evaluation 130
4.2. Results 132
4.2.1. X_o 582 Bulkhead Fractographic Analysis 132
4.2.2. X_o 582 Bulkhead Microstructural Evaluation 132
4.3. Discussion 147
4.4. Conclusions 149

Chapter 5 Future Work 151

References 152

Vita 168

List of Tables

Table 1.1. Alloy type of each sleeve. 8

Table 1.2. Thermal material properties of alloys comprising of the PLBD roller and X_o 582 bulkhead. 9

Table 1.3. Ranges and effects of alloying elements used in titanium alloys. [3]. 14

Table 1.4. Summary of heat treatments for alpha-beta titanium alloys. [3]..... 18

Table 1.5. Designations for wrought aluminum alloys. [4]..... 27

Table 1.6. Temper designations for aluminum alloys. [4] 27

Table 3.1. Average Chemical Composition of Reaction Front - XRF..... 70

List of Figures

Fig. 1.1. Image of orbiter forebody, midbody, and aftbody.....2

Fig. 1.2. Schematic of the X_o 582 ring-frame bulkhead located aft to the crew module.....7

Fig. 1.3. (a) Exemplar configuration of the PLBD latch rollers and crew module overhead Window 7 and Window 8 of Space Shuttle *Endeavor* (b) Close-up view of PLBD roller.....7

Fig. 1.4. (a) Debris components recovered from Space Shuttle *Columbia* positioned in nominal Space Shuttle configuration (b) Close-up view of recovered PLBD port roller and (c) starboard roller positioned in nominal Space Shuttle configuration (d) Titanium deposits on windows indication that the forebody traveled backwards [1]..... 11

Fig. 1.5. Varying broom-straw features seen on fracture surfaces of bulkhead. 12

Fig. 1.6. Schematic of face centered cubic, body centered cubic and hexagonal close-packed planes [4]..... 14

Fig. 1.7. Ti-6Al-4V microstructures, [4] (a) solution treated to 955 ˚C (1750 ˚F) and air cooled; primary α grain with a matrix of acicular α (transformed β),

250X (b) solution treated and water quenched; equiaxed primary α in martensite matrix, 250X (c) solution treated 1 h at 955 ˚C (1750 ˚F), water quenched and annealed 2 h at 705 ˚C (1300 ˚F), equiaxed α grains (light) in matrix of acicular α (dark - transformed β), 500X (d) recrystallization anneal at 925 ˚C (1700 ˚F); equiaxed primary α with intergranular β. 19

Fig. 1.8. Ti-6Al-4V microstructures, [6] (a) Held for 1 h at 1065 ˚C (1950 ˚F), above the β transus, and furnace cooled, plate-like α (light) with intergranular β (dark) [6] (b) Held for 1 h at 1065 ˚C (1950 ˚F) and air cooled, acicular α with prior β grain boundaries [6] (c) β anneal at 1040 ˚C (1900 ˚F); coarse lamellar α and intergranular β [6] (d) Held for 1 h at 1065 ˚C (1950 ˚F) and quenched, martensite (α'), 250X [4]. 20

Fig. 1.9. Ti-6Al-4V microstructures (a) forging, beta annealed 2 h at 705 ˚C (1300 ˚F); basketweave structure, 500X (b) as-forged at 955 ˚C (1750 ˚F), below the β transus; elongated primary α within matrix of acicular α (transformed β), 250X (c) Alpha-case layer observed in Ti-6Al-4V after exposure to 760 ˚C (1400 ˚F) for 90 min (d) Alpha-case layer observed in Ti-6Al-4V after exposure 885 ˚C (1625 ˚F) for 90 min. 21

Fig. 1.10. Ti-Al phase diagram. [7] 23

Fig. 2.1. CFD analysis at the tip of the payload pay door roller for orthogonal geometry into the direction of travel at M = 10.5. 33

Fig. 2.2. (a) Results presented for Ti-6Al-4V samples (with 0.06-in protuberance) within representative boundary regions where passivation, ignition and combustion may result as theorized though testing. Adapted from [12] (b) Arc-jet sample schematic, titanium sample (black) with a flush configuration with wedge holder; (c) Arc-jet sample schematic, titanium sample with 0.06-in protuberance. 34

Fig. 2.3. Schematic representation of variation of oxide thickness with respect to oxidation duration for different oxidation rate laws. [19] 40

Fig. 2.4. Ti-O phase diagram. [7] 43

Fig. 3.1. As-received port roller recovered from Space Shuttle *Columbia*; (a) Sample A outlined in black (deck-facing) - note material loss of outermost A286 sleeve (b) Reaction front (forward-facing) with clock face configuration and quadrants (dashed white line) labeled: quadrant 1 (Q1), quadrant 2 (Q2), quadrant 3 (Q3), and quadrant 4 (Q4) – note material loss of IN718 sleeve shown. 59

Fig. 3.2. Axial bi-sectioning of Sample A yielded Sample A1 to include sub-samples: A1-a, A1-bc, A1-dh; Sleeves contained within each sample identified by alloy type and sequential configuration in parenthesis, (A) to (H), outermost sleeve to innermost sleeve, respectively. 62

Fig. 3.3. Images of Sample A1-a containing A286(A) (a) forward-facing view (top left), ID wall and axial cross-sectional cut surface outlined in white (top right),

(b) transverse cross-sectional cut surface from which microstructural evaluation was performed. Alloy type is indicated and labeled quadrant regions are divided by a dashed white line that also delineates the clock face configuration. 63

Fig. 3.4. Images of Sample A1-bc containing IN718(B) and IN718(C): forward facing view of reaction front (left), ID wall and axial cross-sectional cut surfaces outlined in white (right). Alloy type of each sleeve is indicated and labeled quadrant regions are divided by a dashed white line that also delineates the clock face configuration. 64

Fig. 3.5. Images of Sample A1-dh contained CrIN718(D), Ti6Al4V(E), Ti6Al4V(F), IN718(G), and A286(H): reaction front view (left image), ID wall and axial cross-sectional cut surfaces outlined in white (right image). Note variable wall thickness of the Ti-6Al-4V sleeves. Alloy type of each sleeve is indicated and labeled quadrant regions are divided by a dashed white line that also delineates the clock face configuration. 65

Fig. 3.6. Images of sectioned arc-jet samples: untested, Class I, Class I, and Class III, thickness. 67

Fig. 3.7. Images of Sample A, thermal damage of reaction front (a) Thermal damage in Q1, Q2, and the inside perimeter of Q4; minimal damage observed in Q3 and outside perimeter of Q4 (b) RSMM of reaction front showing slanting

characteristic (c)-(f) magnified images of reaction front corresponding to white boxed regions outlined in (a). 69

Fig. 3.8. SEM image of reaction front (a)-(b) spherical (c)-(d) globular oxide morphology. 71

Fig. 3.9. SEM image of reaction front exhibiting varied surface texture: (a)-(b) Surface ridges (c)-(d) mud-cracked texture. 72

Fig. 3.10. SEM image of reaction front containing (a)-(b) multi-layered scale formation. 73

Fig. 3.11. EDS results of the reaction front corresponding to the outlined region in (a) Q1 and (b) Q3 74

Fig. 3.12. Schematic of external circumferential rim of Ti6Al4V(E) and Ti6Al4V(F). Note overlap of CrIN718(D) by the Ti6Al4V(E) rim. 75

Fig. 3.13. Image of Sample A1-dh with Regions R1-R4 of RSMM and α-case layer Regions AC1-AC3 labeled and outlined in white at the bulk edge surfaces. 76

Fig. 3.14. (a) RSMM deposition onto OD of Ti6Al4V(E)-Q1 at CrIN718(D)/Ti6Al4V(E) inner sleeve-spacing, 100X, (b) RSMM of Ti6Al4V(E) at Ti6Al4V(E)/Ti6Al4V(F) inner sleeve-spacing, 200X (c) RSMM deposition/Ti6Al4V(F) interface, 100X; Kroll's. 77

Fig. 3.15. RSMM deposition in Q1 (a) distinct multi-layered α-case, 100X (b) α-case region with variable width and dark regions and RSMM deposition in Q4

with islands of lath α regions containing, 500X (c) α-case stringers, 100X (d) distinct, uniform α-case layer, 100X; Kroll's 78

Fig. 3.16. EDS results of RSMM deposition. 79

Fig. 3.17. Micrograph of α-case layers observed at the bulk edge surface of Ti6Al4V(E)-Q1 in (a)-(b) AC1, 200X, (c) 500X and (d) Region AC2, 100X; Kroll's.81

Fig. 3.18. Micrograph of porous, deposition (dark) on inner sleeve OD surfaces of Ti6Al4V(E)-Q1 and Ti6Al4V(F)-Q1 in (a) notch region, 150X (b) As-polished micrograph of (a), 150X; (c) inner-sleeve spacing approximately 1-mm (0.04-in.) beyond notch region, 100X; Kroll's. 84

Fig. 3.19. (a)-(b) BSE micrograph of inner-sleeve OD edge surface of Ti6Al4V(F)-Q1 at (a) inner-sleeve spacing approximately 1-mm (0.04-in.) beyond notch region. 86

Fig. 3.20. Image of Sample A1-dh with Regions E1-E4 of Ti6Al4V(E) and F1-F4 of Ti6Al4V(F) labeled and outlined in white..... 87

Fig. 3.21. Micrograph of Ti6Al4V(E)-Q1 in E1 region of bulk; (a) 100X, (b) 200X, (c) 500X; Kroll's..... 88

Fig. 3.22. Micrograph of Ti6Al4V(F)-Q1 in (a) F1.1 region of bulk where microstructural gradient is apparent (approximately 1.5-cm (0.6-in.) from the reaction front edge, 100X; (b) E2 region of bulk approximately 3.3 (1.3-in.) away from reaction front, 100X, and (c) 100X (measurements obtained from the edge surface of Ti6Al4V(F)-Q1); Kroll's. 90

Fig. 3.23. Micrograph of Ti6Al4V(E)-Q4 in (a) E3 region of bulk at the reaction front edge, 100X and (b) 1000X; (c) E4 region of bulk approximately 3.3 cm (1.3-in.) away from reaction front, 100X and (d) 1000X; Kroll's. 91

Fig. 3.24. Micrograph of Ti6Al4V(F)-Q1 in (a) F1.1 region of bulk where microstructural gradient is apparent (approximately 0.76-cm (0.3-in). from the reaction front) 100X and in (b) F2 region of bulk approximately 3.3-cm (1.3-in.) away from reaction front, 100X and (c) 1000X; Kroll's. 93

Fig. 3.25. Micrograph of Ti6Al4V(F)-Q4 in (a) F3 region of bulk at the reaction front edge surface, 100X and (b) 1000X; (c) F4 region of bulk approximately 3.3-cm (1.3-in.) away from reaction front, 100X and (d) 1000X; Kroll's. 94

Fig. 3.26. Diffraction patterns of Ti6Al4V(E) in Q1 region at Regions E1 and E2 as outlined in the provided schematic. 95

Fig. 3.27. Diffraction patterns of Ti6Al4V(F) in Q1 at Regions F1 and F2 as outlined in the provided schematic..... 96

Fig. 3.28. Microhardness results for Ti6Al4V(E) and Ti6Al4V(F) in both Q1 and Q4. Measurements taken along axial length moving away from the reaction front edge..... 97

Fig. 3.29. Image of Sample A1-dh with Regions A1-A3 of A286(A) and H1-H3 of A286(H) labeled and outlined in white. 98

Fig. 3.30. Micrograph of A286(A)-Q1 in the (a)-(b) A1 region of bulk at the reaction front edge surface and in the (c) A2 region and A3 region of Q4. 100

Fig. 3.31. Micrograph of A286(H)-Q1 in (a) H1 region of bulk at the reaction front edge surface and (b) A286(H)-Q4 in H2 region of bulk at the reaction front edge surface and (c) H3 region of bulk away from reaction front; 1000X, Kalling's No. 2 102

Fig. 3.32. Image of Sample A1-bc with Regions B1-B4 of IN718(B) and Regions C1-C4 of IN718(C) labeled and outlined in white..... 103

Fig. 3.33. Image of Sample A1-bc with Regions D1-D4 of CrIN718(D) and Region G1 of IN718(G) labeled and outlined in white..... 103

Fig. 3.34. Micrograph of IN718(B)-Q1 in (a) B1 region of bulk reaction at the front edge surface, 100X, (b) 500X (c) B2 region of bulk away from reaction front, 100X, (b) 500X; Kalling's No. 2. 105

Fig. 3.35. Micrograph of IN718(B)-Q4 in (a) B3 region of bulk reaction at the front edge surface, 100X, (b) 500X (c) B4 region of bulk away from reaction front, 100X, (b) 500X; Kalling's No. 2. 105

Fig. 3.36. Micrograph of IN718(C)-Q1 in (a) C1 region of bulk reaction at the front edge surface, 100X, (b) 500X (c) C2 region of bulk away from reaction front, 100X, (b) 500X; Kalling's No. 2. 106

Fig. 3.37. Micrograph of IN718(C)-Q4 in (a) C3 region of bulk reaction at the front edge surface, 100X, (b) 500X (c) C4 region of bulk away from reaction front, 100X, (b) 500X; Kalling's No. 2. 107

Fig. 3.38. Micrograph of CrIN718(D)-Q1 in (a) D1 region of bulk at the reaction front edge surface, 150X and (b) BSE micrograph in D1 region; micrograph of D2 region of bulk away from reaction front, (c) 150X, (d) 500X; Kalling's No. 2. 109

Fig. 3.39. BSE micrograph of CrIN718(D)-Q1 in (a)-(b) D1 region of bulk at the reaction front edge surface and in (c)-(d) D2 region of bulk away from reaction front. 110

Fig. 3.40. Micrograph of CrIN718(D)-Q1 in (a) D3 region of bulk reaction at the front edge surface, 100X, (b) 500X (c) D4 region of bulk away from reaction front, 100X, (b) 500X; Kalling's No. 2. 111

Fig. 3.41. Micrograph of IN718(G)-Q1 in G1 region of bulk, 100X; Kalling's No. 2. 112

Fig. 3.42. Micrographs of arc-jet samples, (a) unaffected (b) Class I (c) Class II, (d) Class III; Kroll's. 114

Fig. 3.43. Micrographs of (a) Class II and (b) Class III arc-jet samples; Kroll's.. 115

Fig. 4.1. Portion of X_o 582 ring-frame bulkhead with PLBD latch roller removed. Black dashed lines outline sectioning implemented to isolate samples BhA, BhB and BhC. Black arrows indicate surfaces of which microstructural evaluation was carried out and notation refers to longitudinal "L" surfaces the cross sectional, transverse "T" surfaces. 131

Fig. 4.2. Fractographs of (a) broomstraw features and (b) ductile mode fracture features observed on BhA. 133

Fig. 4.3. Transverse broom-straw microstructure, BhA-T; etched with Keller's reagent (a) 100X and (b) 1000X; longitudinal broom-straw microstructure, BhA-L; etched with Keller's reagent (c) 100X and (d) 500X. 135

Fig. 4.4. Micrograph of broom-straw microstructure observed on sample BhA-T: (a) 100X (b) 500X and sample BhC-T: (c) 250X (d) 500X; etched with Keller's reagent. 136

Fig. 4.5. Light optical micrograph of sample BhA-T: deposition on backside surface of bulkhead (b) microstructure adjacent to deposition; etched with Keller's reagent, 1000X. 137

Fig. 4.6. Micrograph of samples located away from fracture: (a) BhB-L and (b) BhB-T; etched with Keller's reagent, 100X. 138

Fig. 4.7. (a) Backscatter electron micrograph of liquated grain boundaries observed at broom-straw fracture (BhA-T) with EDS analysis regions outlined in black boxes (b)-(d) EDS spectrum of associated regions outlined in (a). 139

Fig. 4.8. Backscatter electron micrograph of BhA-T; EDS analysis was performed on precipitates outlined in black. 140

Fig. 4.9. (a) Backscatter electron micrograph of coarse, irregular precipitate observed at broom-straw fracture (BhA-T); (b)-(f) EDS spectrum of corresponding regions outline in (a). 141

Fig. 4.10. (a) Backscatter electron micrograph of coarse, irregular precipitates and liquated grain boundaries observed at broom-straw fracture (BhA-T); (b)-(f) EDS spectrum of corresponding regions outline in (a). 142

Fig. 4.11. (a) Backscatter electron micrograph of coarse, irregular precipitates and liquated grain boundaries observed at broom-straw fracture (BhA-T); (b)-(f) EDS spectrum of corresponding regions outline in (a). 143

Fig. 4.12. (a) Backscatter electron micrograph of coarse, irregular precipitates and liquated grain boundaries observed at broom-straw fracture (BhA-T); (b)-(f) EDS spectrum of corresponding regions outline in (a). 144

Fig. 4.13. (a) Backscatter electron micrograph of coarse, irregular precipitates and liquated grain boundaries observed at broom-straw fracture (BhA-T); (b)-(f) EDS spectrum of corresponding regions outline in (a). 145

Fig. 4.14. (a) Backscatter electron micrograph of deposition located on backside of bulkhead; (b)-(f) EDS spectrum of associated regions outlined in (a). 146

Chapter 1

Introduction

1.1. Space Shuttle *Columbia* Accident

Shuttle Transportation System Mission 107 (STS-107) lifted off from the Kennedy Space Center (KSC) on January 16, 2003 for a 16-day Earth science and microgravity research mission. During the shuttle's deorbit on February 1, damage to the left wing caused major structural breakup of the vehicle and the seven crewmembers aboard Space Shuttle *Columbia* lost their lives. [1] The *Columbia* Accident Investigation Board (CAIB), commissioned by the National Aeronautical and Space Administration (NASA), conducted a review of the organizational and technical causes of the disaster. The accident investigation found that a large piece of insulating foam broke off from the external tank and struck the leading edge of the left wing, causing a compromise to the thermal protective system (TPS). This compromise, undetected during flight, allowed hot gasses to enter the wing and penetrate into the vehicle, leading to breakup of the orbiter, as the gas travelled aft and inboard, toward the midbody fuselage and

left main landing gear well, causing critical internal damage. Fig. 1.1 provides a schematic of the orbiter forebody, midbody and aftbody.

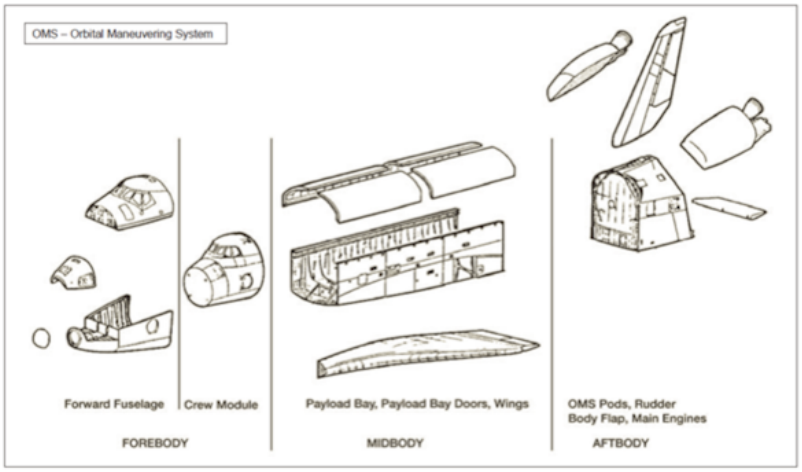

Fig. 1.1. Image of orbiter forebody, midbody, and aftbody.

Based on the findings and recommendations provided by the CAIB, the Space Shuttle Return to Flight Implementation Plan made changes to enhance the organization structure of NASA and increase knowledge and understanding of flight environment. The Spacecraft Crew Survival Integrated Investigation Team (SCSIIT) was commissioned by NASA to perform a comprehensive analysis of the incident to provide recommendations to improve the safety of future space vehicles. The report of their analysis outlined all events of the accident that were determined to be lethal from the time of deorbit until the spacecraft made ground impact:

1. That the crew module lost pressure rapidly, not allowing adequate time for the crew to configure the pressure suits that would provide full protection from the loss of cabin pressure.
2. The crew member harnesses were not locked, so when the orbiter lost control and the forebody (containing the crew module and forward fuselage) separated from the vehicle, the unconscious and/or deceased crew was exposed to cyclical rotational motion, causing lethal trauma.
3. Crew member became exposed to exceedingly high temperatures from re-entry, which is not survivable beyond the TPS.
4. The suit system worn by the crew members serves to protect crew members to a maximum altitude of 30,480-m (100,000-ft) and a velocity of 560 knots (644 mph), thus survivability even after exposure to hypersonic entry conditions is not possible.
5. The forces associated with ground impact are lethal. The ascent and entry suit system contains a parachute system, protecting the crew member from ground impact, but requires manual activation to employ.

Key recommendations were provided by the SCSIIT to increase protection of the crew during space flight. These include placing greater emphasis on optimizing crew procedures, including survival operations and also enhancing the design of the spacecraft for improvement of suit and seat systems. It was also recommended that engineers and scientists incorporate comprehensive

analysis of orbiter break up and loss of control events in order to optimize spacecraft design for graceful, and somewhat predictable, degradation under failure. A slow breakup may afford the crew additional time to problem solve and execute survival strategies, increasing survivability potential.

From the accident investigation, it was observed that some sub-structural titanium components exhibited significant thermal erosion that was not likely to have occurred from re-entry heating alone. Investigators determined that shock wave interactions could be a possible cause of this damage and later testing showed that combustion may have played a major role. Titanium combustion in low-pressure, high temperature environments is not well understood, and the potential reaction of this alloy was not a vehicle design consideration for any space programs at the time. To improve understanding, a thorough characterization of this material behavior under entry conditions was recommended by the SCIIT investigators.

A comprehensive understanding of material response to re-entry is critical for all materials, including those used for sub-structural components, in order to fully evaluate safe applicability of materials for crew exploration vehicle construction. Increased knowledge can promote innovation in design that may prevent future failures and may ensure that the underlying spacecraft structure provides some margin of protection for the crew in the event that the TPS is compromised.

The present work serves to provide analysis of debris recovered from the *Columbia* accident to investigate material behavior of sub-structural aerospace alloys exposed to re-entry conditions. This study involves a materials characterization of one port-side payload bay door (PLBD) latch roller and a section of the forward ring-frame bulkhead to which the port-side PLBD latch roller is attached.

1.2. Atmospheric Re-entry

Atmospheric re-entry from orbital velocities involve high energy that produces an extreme thermal and chemical environment. Atmospheric composition at the altitude of re-entry, approximately 120,700-m (396,000-ft), is similar to that at sea level (79% N_2, 21% O_2, 0.93% Ar, and 0.04% CO_2). The strong shock waves that form as a result of hypersonic entry velocities compress ambient air to produce a high-temperature, high-pressure environment in which molecules are more likely to dissociate into charged particles (e.g. $O_2 \rightarrow O + O$, $N_2 \rightarrow N + N$). The existence of dissociated atoms (plasma) intensifies heat transfer at the orbiter surface as the exothermic reactions, atomic recombination and oxidation, occur. [1]

1.3. Space Shuttle *Columbia* Debris Hardware

The focus of this research includes the analysis of forward PLBD latch roller components and the X_o 582 ring-frame bulkhead of the orbiter to which the PLBD rollers were attached. The PLBD rollers serve as a part of the latch mechanism for securing the PLBDs of the midbody and the X_o 582 bulkhead is one of the partitions that separates the midbody from the forebody, Fig. 1.2.

Fig. 1.3a provides an exemplar Space Shuttle configuration of the forward PLBD port rollers, the X_o 582 ring-frame bulkhead and crew module overhead Window 7 and Window 8 of Space Shuttle *Endeavor*. From post-accident analysis [1], the amount of time the forward PLBD roller and bulkhead may have been exposed to re-entry heating after the PLBDs separated from the mid-fuselage, can be estimated to be 36 seconds, measuring from an altitude of approximately 55,105-m (180,792-ft) to ground impact. A close-up of an exemplar PLBD roller is displayed in Fig. 1.3b, also obtained from Space Shuttle *Endeavor*. The PLBD roller construction is comprised of nine concentric sleeve-type components designed such that the sleeve components may each slide axially and telescope, as illustrated in Fig. 1.3b.

Table 1.1 provides a sequential list of each sleeve alloy type and position as confirmed by chemical analysis using XRF and EDS. Thermal properties of the alloys that comprise the PLBD roller and X_o 582 bulkhead are included in Table 1.2

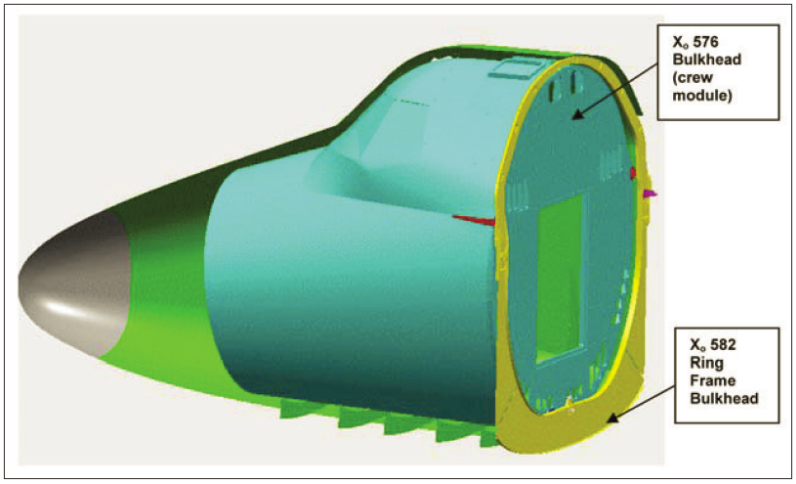

Fig. 1.2. Schematic of the X_o 582 ring-frame bulkhead located aft to the crew module.

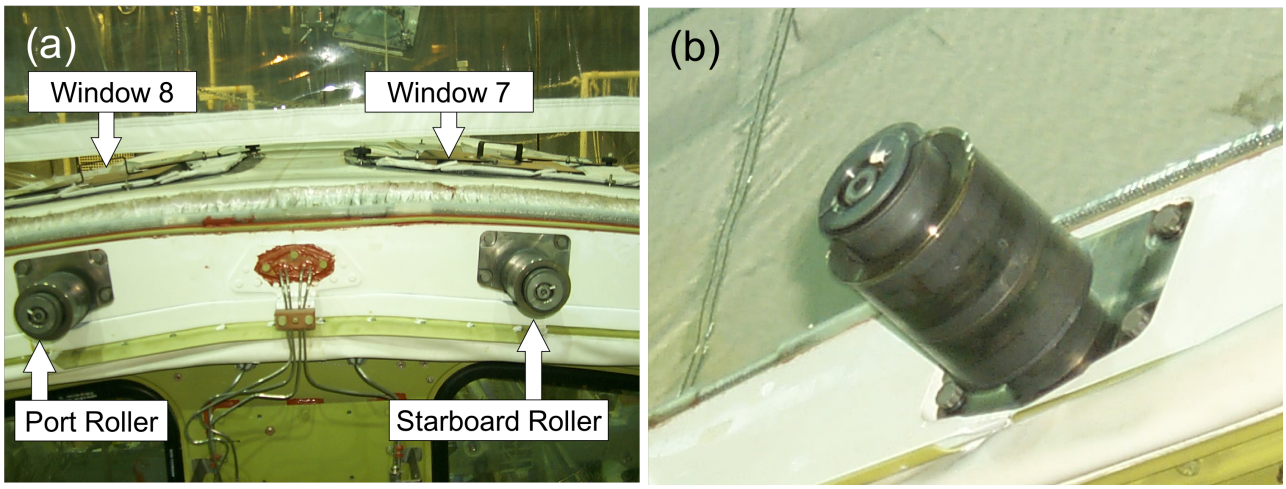

Fig. 1.3. (a) Exemplar configuration of the PLBD latch rollers and crew module overhead Window 7 and Window 8 of Space Shuttle *Endeavor* (b) Close-up view of PLBD roller.

Table 1.1. Alloy type of each sleeve.

Position Number[1]	Sleeve Name	Position Label
1	A286[2]	A
2	CrIN718[3]	B
3	IN718[4]	C
4	IN718	D
5	Ti6Al4V[5]	E
6	Ti6Al4V	F
7	A286	G
8	IN718	H

[1]Listed sequentially 1 (outermost sleeve) through 8 (innermost sleeve)

[2]Iron-based superalloy A-286

[3]Chromium-plated, nickel-based superalloy Inconel 718

[4]Titanium alloy Ti-6Al-4V

[5]Nickel-based superalloy Inconel 718

Table 1.2. Thermal material properties of alloys comprising of the PLBD roller and X_O 582 bulkhead.

Material	Melting Temperature, ˚C (˚F)	Thermal Conductivity, W/m-K (BTU-in/hr-ft^2-˚F)	Specific Heat Capacity, J/g-˚C (BTU/lb-F˚)
Ti6Al4V	1604-1660 (2919-3020)	6.7 (46.5)	0.5263 (0.1258)
A286	1370-1430 (2500-2610)	12.7 (88.1)	0.419 (0.100)
IN718	1260-1336 (2300-2437)	11.4 (79.1)	0.435 (0.104)
AA2024	502-638 (935-1180)	121 (840)	0.875 (0.209)
Cr	1860 (3380)	69 (480)	0.461 (0.110)

Fig. 1.4a shows recovered port and starboard PLBD rollers, in an exemplar arrangement with Window 7 and Window 8. Fig. 1.4b-c show deterioration of both rollers, illustrating similar localized damage to the titanium regions, as well as similarities in damage severity and appearance. This observation, along with the close proximity of the PLBD rollers to overhead windows, led investigators [1] to identify the PLBD rollers as a likely source of the window char layer deposition. It should be noted that the slanting feature of the damage seen on both rollers is suggestive of backwards travel of the forebody for a period of time after its separation from the orbiter, Fig. 1.4d, a point that was outlined in post-accident analyses and will be further discussed in later sections.

Also apparent in Fig. 1.4a-c, was localized material loss of the X_o 582 ring-frame bulkhead. The extensive, localized material loss, seen on adjacent sides of the two recovered PLBD rollers appeared as 'holes' suggesting impact to the regions. From CFD analysis it was determined that shock-shock interaction impingement could be responsible for the material loss. [1] Illustrated in Fig. 1.5a-d, the fracture surfaces outlining the 'holes' exhibited unique fracture surfaces, termed broom-straw fracture. In addition to characterizing the broom-straw feature, examination of the bulkhead also involved evaluation of gray-colored, spray-like deposition observed on the backside of the bulkhead, as seen in Fig. 1.5d.

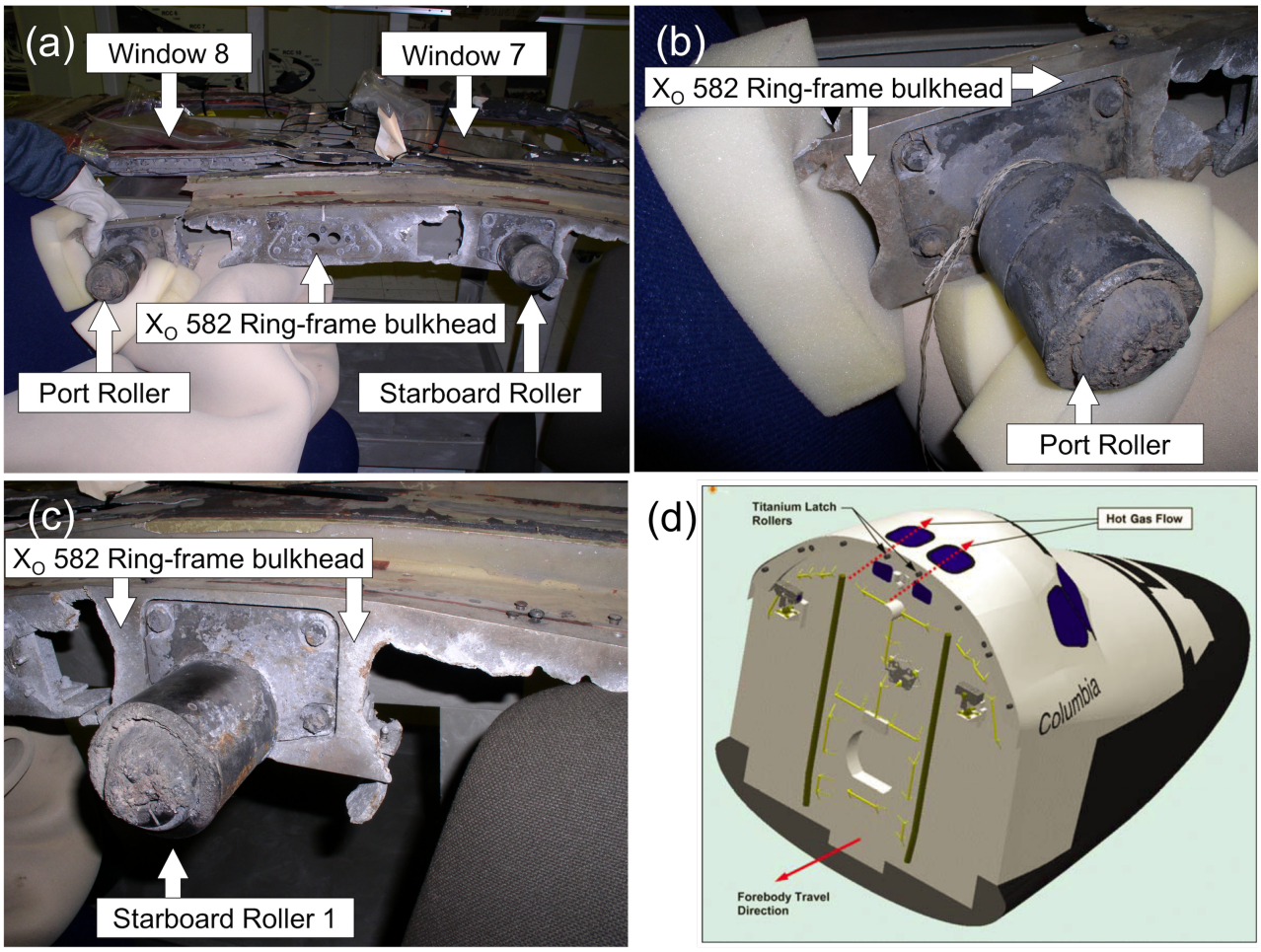

Fig. 1.4. (a) Debris components recovered from Space Shuttle *Columbia* positioned in nominal Space Shuttle configuration (b) Close-up view of recovered PLBD port roller and (c) starboard roller positioned in nominal Space Shuttle configuration (d) Titanium deposits on windows indication that the forebody traveled backwards [1].

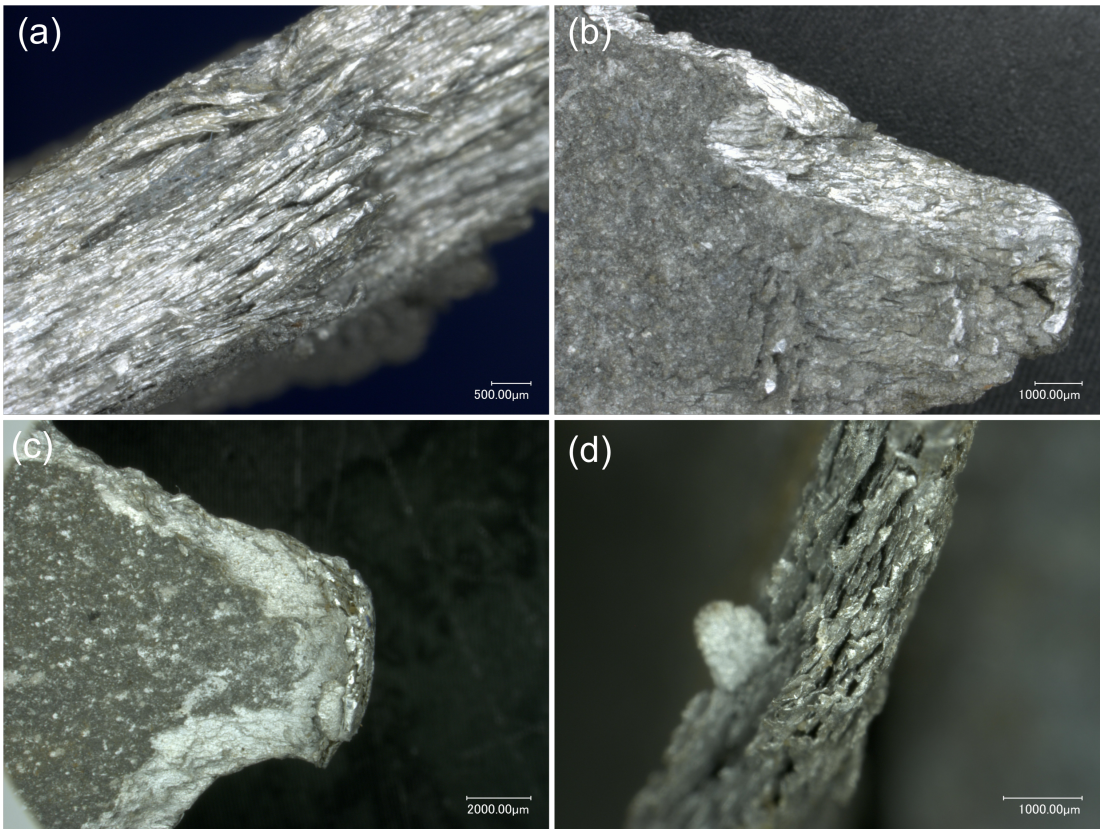

Fig. 1.5. Varying broom-straw features seen on fracture surfaces of bulkhead.

1.4. Overview of Ti-6Al-4V, Inconel 718 and A-286 Alloys

1.4.1. Titanium and Titanium Alloys

Titanium and titanium alloys find extensive aerospace application due to their high strength-to-weight ratio, strength at elevated temperature and excellent corrosion resistance. A stable surface oxide forms instantly when

unoxidized titanium is exposed to air and/or moisture, thus protecting the metal and providing excellent corrosion resistance.

The allotropic behavior of titanium is an important feature, as its ability to exist as hexagonal closed-packed (hcp) alpha-Ti (α) and body centered cubic (bcc) beta-Ti (β), allows for complex variations in microstructure which provided a broad range in material properties dependent upon on thermal and mechanical processing. A schematic of hcp, bcc and face centered cubic planes are provided in Fig. 1.6. Elevated-temperature application is limited to approximately 540-600 ˚C (1000-1100 ˚F) due to degradation in strength and creep resistance, as well as to the pickup of impurities, a result of titanium's high reactivity.

At room temperature, pure titanium exists in the α phase and transforms to the β structure at the β transus, approximately 885 ˚C (1625 ˚F). [2, 3]. Commercially pure grades of titanium are useful when corrosion resistance is needed. Extra-low interstitial (ELI) grades are used for applications of high ductility, as carbon, nitrogen, oxygen and iron lower ductility and cannot be present above a critical concentration.

With the addition of alloying elements, the β transus, maybe increased or decreased, and depending on the amount and type of alloying additions, an α-transus may also exist, below which the alloy is a complete α structure and above which (and below the β transus) both α and β phases are present. These variations in transformation serve as the basis for the three classifications of titanium alloys: α alloys, β alloys and α/β alloys.

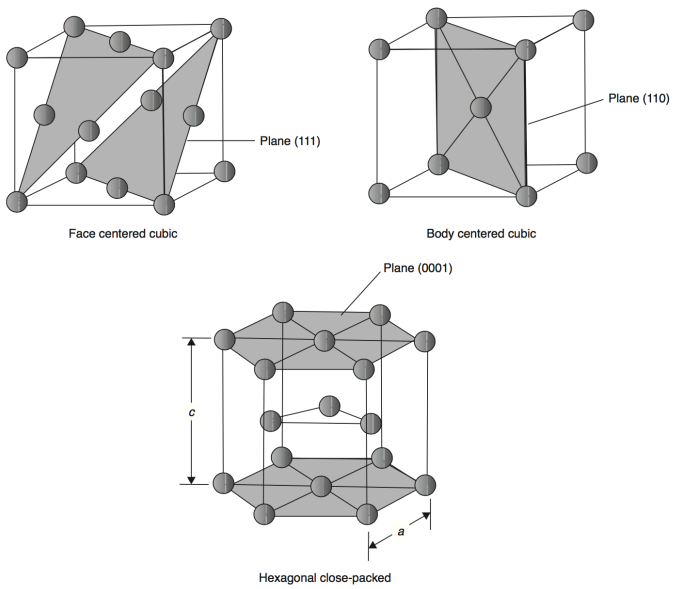

Fig. 1.6. Schematic of face centered cubic, body centered cubic and hexagonal close-packed planes [4].

Table 1.3. Ranges and effects of alloying elements used in titanium alloys. [3].

Alloying elements	Approximate range, wt%	Effect on microstructure
Aluminum	2-7	Alpha stabilizer
Tin	2-6	Alpha stabilizer
Vanadium	2-20	Beta stabilizer
Molybdenum	2-20	Beta stabilizer
Chromium	2-12	Beta stabilizer
Copper	2-6	Beta stabilizer
Zirconium	2-8	Alpha and beta strengthener
Silicon	0.05-1	Improves creep resistance

Alpha alloys, possessing high ductility and slightly less corrosion resistance than pure titanium, essentially contain a full α structure, and cannot be strengthened by heat treatment due to the stability of the α phase. Certain alloys, classed as near-α alloys, contain small amounts of β-stabilizing elements, thus can exhibit variations in microstructure, but behave more like conventional α alloys during thermal processing. Near-α alloys exhibit good strength and creep resistance at elevated temperature and provide good mechanical properties at cryogenic temperatures.

Beta alloys contain mostly β stabilizers with small amounts of α stabilizer to provide strengthening. Beta and near-β alloys are metastable and demonstrate good fracture toughness, and also have limited weldability and increased density, as the amount of heavy β stabilizer additions increase. Typically, β alloys provide high strength and are highly resistant to stress-corrosion cracking, but their application is limited to a temperature of 370-700 ˚C (700-1290 ˚F) due to creep.

Alpha-beta alloys contain both α and β stabilizers, benefiting from a mixture of α and transformed β when a solution heat treatment is followed by aging. The addition of aluminum and vanadium strengthens and stabilizes the α phase and β phase, respectively. The α phase of titanium is achieved at lower temperatures and at higher temperatures, the β phase predominates.

1.4.1.1. Titanium Alloy Ti-6Al-4V

Ti-6Al-4V is a widely used α/β alloy and is considered the workhorse of the titanium industry, accounting for up to 60% of production. The microstructure of α/β alloys, like Ti-6Al-4V, can be equiaxed, acicular or a combination of both. The following provides an overview of the heat treatments employed for α/β titanium alloys, with a summary included in Table 3.2.

As illustrated in Fig. 1.7a-d, a microstructure of globular, equiaxed α is achieved when heating occurs in the α/β range, 955 ˚C (1750 ˚F). When air cooled from within the α/β region, primary α within a matrix of transformed β is yielded as shown in Fig. 1.7a and Fig. 1.7c. When quenching takes place from high in the α/β region, the resulting structures are characterized by equiaxed primary α and α', Fig. 1.7b. When slow cooling occurs from the α/β range, globular, primary α is formed with intergranular retained β, Fig. 1.7d. The α/β range from which slow cooling occurs, determines the coarsening effect [5]. When heated into the high end of the α/β range, the fraction of β phase that is available to transform into primary α increases. The ideal microstructure, providing the best combination of properties is the result of solution heat treating, then quenching from just below the β transus, followed by aging.

Heating above the β transus yields a microstructure of lamellar α within β grains upon cooling, Fig. 1.8a-d. A slow cooling rate produces plate-like, lamellar α (Fig. 1.8a and Fig. 1.8c) while a moderate cooling rate results in decreased

thickness of the lamellar structure, α appearing more acicular, Fig. 1.8b. Rapid cooling (quenching) from above the β transus yields α' as displayed in Fig. 1.8d.

The microstructures in Fig. 1.9a provide an example of a basketweave, lamellar structure, termed Widmanstätten, produced by moderate to slow cooling from above the β transus, Fig. 1.9a. The as-forged structure of Fig. 1.9b contains elongated primary α grains within a matrix of transformed β.

At titanium surfaces, within an oxidizing environment, an α-case layer (Fig. 1.9c-d) forms simultaneously with the formation of the oxide layer at elevated temperatures, as interstitial oxygen (or nitrogen) migration in this area stabilizes the α phase leading to a brittle supersaturated α region, as well as increased hardness within and beyond the depth of the α-case layer.

Table 1.4. Summary of heat treatments for alpha-beta titanium alloys. [3]

Heat treatment designation	Heat treatment cycle	Microstructure
Duplex anneal	Solution treat at 50 – 75 ˚C (120 – 170 ˚F) below Tβ, air cool and age for 2-8 h at 540 – 675 ˚C (1000 – 1250 ˚F)	Primary alpha, plus Widmanstätten alpha + beta regions
Solution treat and age	Solution treat at ~40 ˚C (100 ˚F) below Tβ, water quench and age for 2 – 8 h at 535 – 675 ˚C (995 – 1250 ˚F)	Primary alpha, plus tempered alpha' or beta + alpha mixture
Beta anneal	Solution treat at ~15 ˚C (60˚ F) above Tβ, air cool and stabilize at 650 – 760 ˚C (1200 – 1400 ˚F) for 2 h	Widmanstätten alpha + beta colony microstructure
Beta quench	Solution treat at ~15 ˚C (60 ˚F) above Tβ, water quench and temper at 650 – 760 ˚C (1200 – 1400 ˚F) for 2 h	Tempered alpha'
Recrystallization anneal	925 ˚C (1700 ˚F) for 4 h, cool at 50 ˚C/h (120 ˚F/h) to 760 ˚C (1400 ˚F), air cool	Equiaxed alpha with beta at grain boundary triple points
Mill anneal	Alpha + beta hot work + anneal at 705 ˚C (1300 ˚F) for 30 min to several h and air cool	Incompletely recrystallized alpha with a small volume fraction of small beta particles

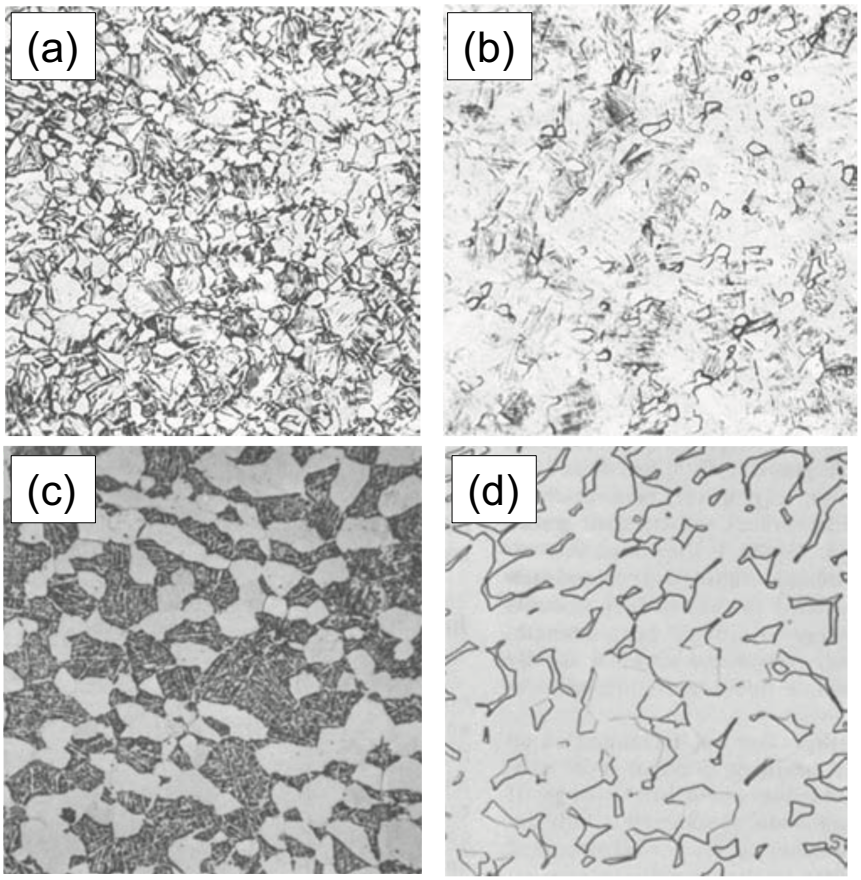

Fig. 1.7. Ti-6Al-4V microstructures, [4] (a) solution treated to 955 ˚C (1750 ˚F) and air cooled; primary α grain with a matrix of acicular α (transformed β), 250X (b) solution treated and water quenched; equiaxed primary α in martensite matrix, 250X[1] (c) solution treated 1 h at 955 ˚C (1750 ˚F), water quenched and annealed 2 h at 705 ˚C (1300 ˚F), equiaxed α grains (light) in matrix of acicular α (dark - transformed β), 500X (d) recrystallization anneal at 925 ˚C (1700 ˚F); equiaxed primary α with intergranular β.

[1] Magnifications throughout this document refer to the original magnification of the image.

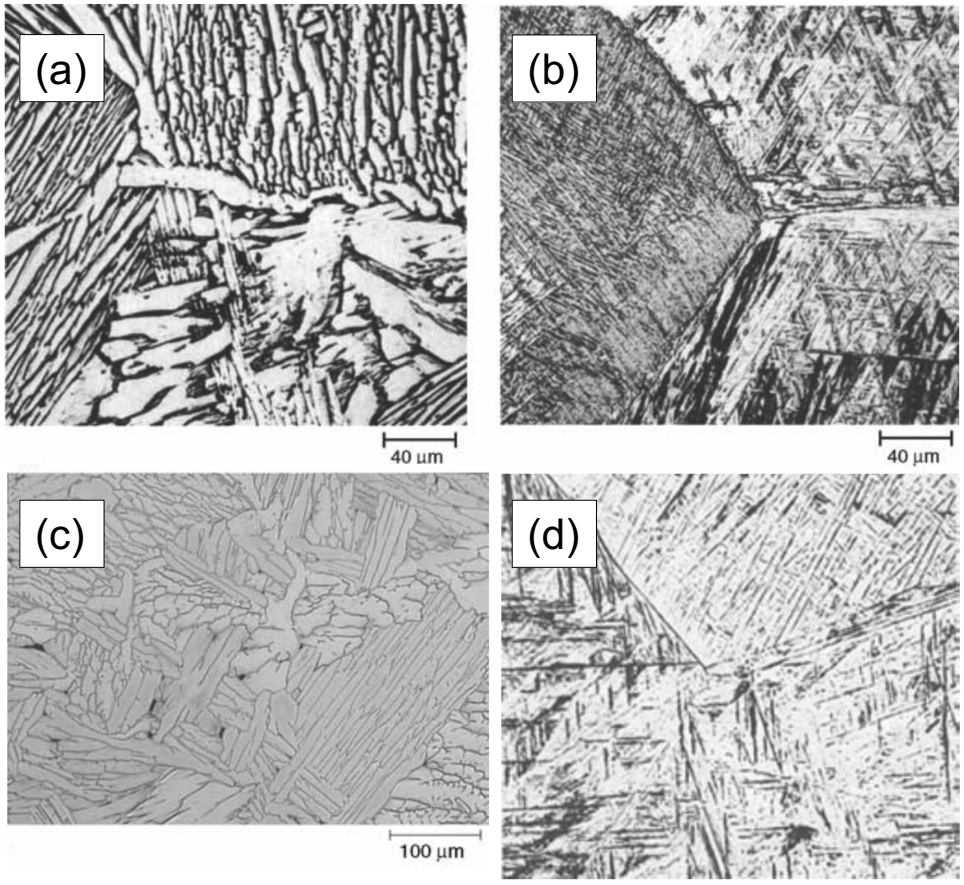

Fig. 1.8. Ti-6Al-4V microstructures, [6] (a) Held for 1 h at 1065 ˚C (1950 ˚F), above the β transus, and furnace cooled, plate-like α (light) with intergranular β (dark) [6] (b) Held for 1 h at 1065 ˚C (1950 ˚F) and air cooled, acicular α with prior β grain boundaries [6] (c) β anneal at 1040 ˚C (1900 ˚F); coarse lamellar α and intergranular β [6] (d) Held for 1 h at 1065 ˚C (1950 ˚F) and quenched, martensite (α'), 250X [4].

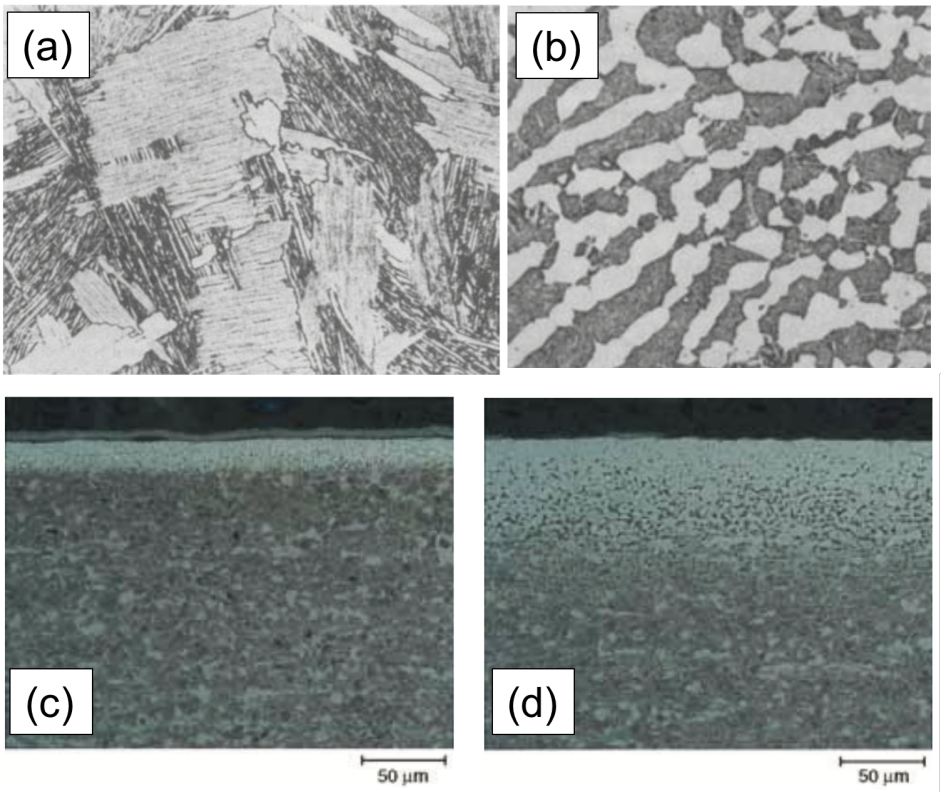

Fig. 1.9. Ti-6Al-4V microstructures (a) forging, beta annealed 2 h at 705 ˚C (1300 ˚F); basketweave structure, 500X (b) as-forged at 955 ˚C (1750 ˚F), below the β transus; elongated primary α within matrix of acicular α (transformed β), 250X (c) Alpha-case layer observed in Ti-6Al-4V after exposure to 760 ˚C (1400 ˚F) for 90 min (d) Alpha-case layer observed in Ti-6Al-4V after exposure 885 ˚C (1625 ˚F) for 90 min.

The precipitation of Ti_3Al (α_2) particles may form in Ti-6Al-4V as a result of the alloy element partitioning effect. As shown in Fig. 1.10, α_2 forms in titanium at aluminum concentrations of > 10%. Upon matrix separation into α phase and β phase, the α stabilizer (aluminum) and β stabilizer (vanadium) will diffuse to the two phases, respectively, leading to a localized increase in aluminum or

vanadium content. Oxygen promotes age hardening by the formation of α_2, as oxygen serves as a strong α stabilizer, thus yielding an increase of aluminum diffusion into the large volume fraction of the α phase.

Partitioning leads to α lamellae not responding to age hardening as well as globular primary α. For Ti-6Al-4V, the α_2 solvus is 550 ˚C (1020 ˚F), so aging at 500 ˚C (930 ˚F) will precipitate α_2 particle. Alloy partitioning increases with increase in globular α, leading to a lower strength within the lamellae of the bimodal structure compared to a full lamellar structure. The β phase contains lower amounts of oxygen, which promotes age hardening by formation of α_2. The existence of primary α suggests a difference in strength between the transformed β and the primary α due to the alloy partitioning effect.

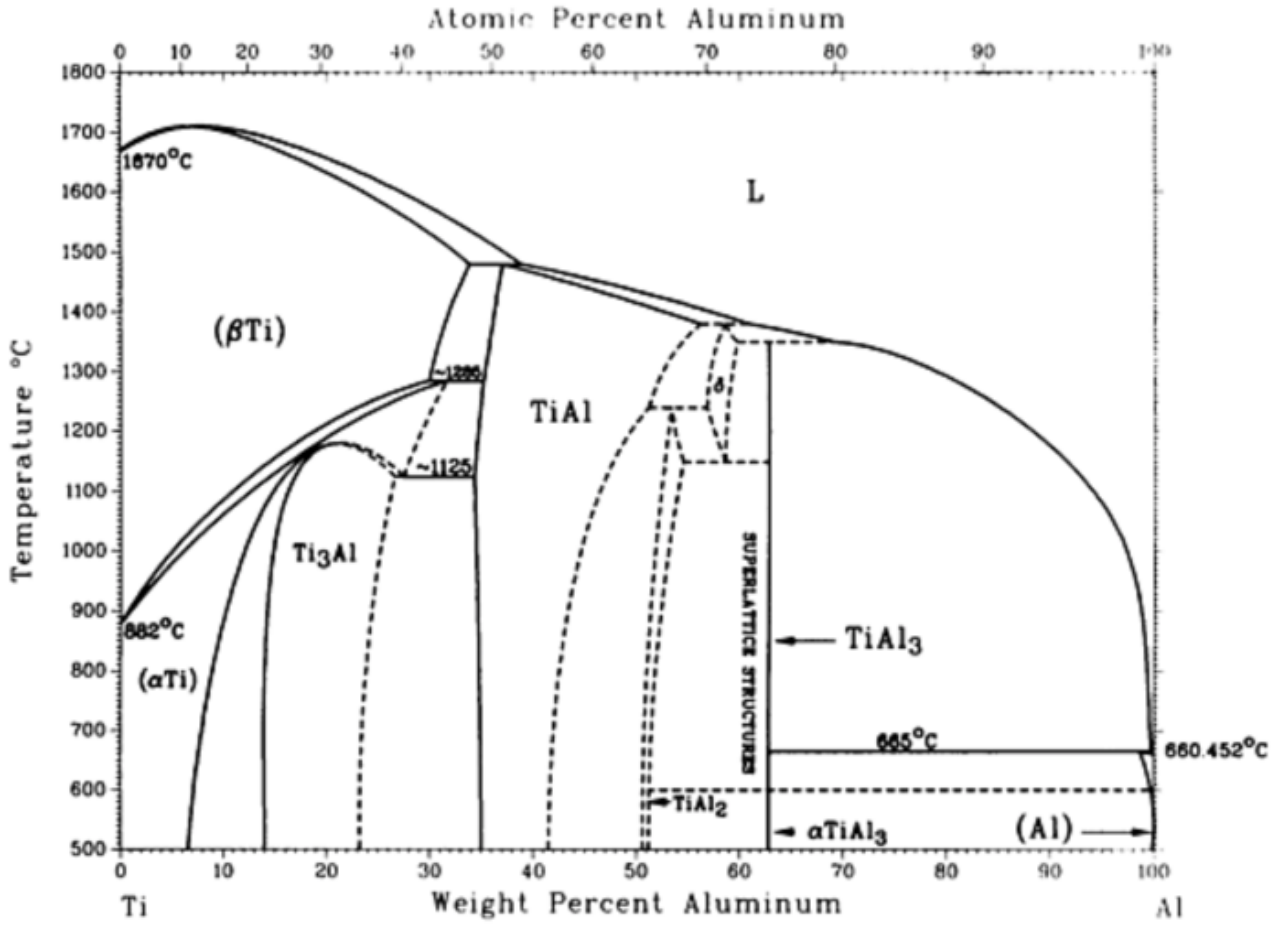

Fig. 1.10. Ti-Al phase diagram. [7]

1.4.2. Superalloy Metallurgy

Superalloys find applications at elevated temperatures and demonstrate a combination of strength and resistance to surface degradation. Superalloys are nickel-, iron-chromium-, and cobalt-based with properties that are manipulated by thermomechanical processing and heat treatment. All superalloys contain an

austenitic (γ) fcc matrix stable at room temperature. Superalloys are typically heavy with densities influenced by alloying additions.

The primary strengthening mechanism for the nickel- and iron-chromium-based superalloys is solid solution strengthening (SSS) and precipitation hardening. The γ matrix dissolves a large amount of solid solution hardeners, such as cobalt, iron, chromium, molybdenum and tungsten. Titanium and aluminum also participate in solid solution strengthening and serves as the primary elements in precipitation hardening. Grain boundary carbides provide high-temperature stability and molybdenum and tungsten minimize creep at elevated temperatures.

Gamma prime (γ'), the fcc intermetallic compound $Ni_3(Al,Ti)$, is the most important of the precipitates formed in nickel- and iron-nickel-based superalloys. Gamma prime has a 0.1% mismatch with the γ matrix, thus maintains high temperature stability as a result of low surface energy. Spherical γ' indicates a matrix mismatch of 0 to 0.2% while a cubical and plate-like morphologies indicate a mismatch of 0.5 to 1%, and >1.25%, respectively. Grain boundary γ' that develops during heat treatment improves stress rupture properties.

Secondary phases that influence properties include: MC-, $M_{23}C_6$-, M_6C- and M_7C_3-type carbides. Body-centered tetragonal (bct) ordered Ni_3Nb (γ''), hexagonal ordered Ni_3Ti (η) and orthorhombic Ni_3Nb (δ) are also other phases common to nickel-based and iron-based superalloys. Detrimental phases that form in superalloys

are topologically close-packed (tcp) phases, tetragonal σ, rhombohedral μ and hexagonal Laves.

1.4.2.1. Nickel-based Superalloy Inconel 718

Inconel 718, a nickel-based superalloy, is considered the single most important wrought superalloy. The alloy demonstrates a good combination of mechanical properties at temperatures up to 704 ˚C (1300 ˚F), is moderately priced and is easily processed. [8] When high amounts of γ' are present, the alloys can see increases in strength at elevated temperatures as the precipitates tend to coarsen slowly. Gamma double prime (γ'') is also involved with strengthening the alloy, but is unstable at temperatures above 650-815 ˚C (1200-1500 ˚F) due to a large mismatch (2.9%) with the matrix. Additional strengthening can be seen with the formation of carbides with the added carbide, which can contain chromium, molybdenum, or iron.

1.4.2.2. Iron-based Superalloy A-286

Alloy A-286 is an austenitic, precipitation-hardenable stainless steel designed for high temperature applications up to 704 ˚C (1300 ˚F). The alloy has high strength and good corrosion resistance. The strengthening precipitate for A-286, γ', is titanium-rich, thus care must be taken to avoid the formation

hexagonal ordered Ni_3Ti (η), the less effective strengthening precipitate that forms at high titanium/aluminum ratios. Austenite is able to be retained at low temperatures upon cooling, due to nickel reducing the temperature at which austenite transforms to martensite. Chromium provides excellent corrosion resistance and, along with molybdenum, participates in SSS. Boron serves to prevent formation of the deleterious η phase and also aids in enhancing stress-rupture resistance.

1.4.3. Aluminum and Aluminum Alloys

Advanced aluminum alloys are employed in aerospace applications due to their high strength to weight ratio and high fatigue resistance. Copper, manganese, magnesium, silicon, and zinc are the primary alloying elements. Aluminum alloys are divided into two classifications: non-heat-treatable alloys, 1XXX, 3XXX, 4XXX and 5XXX and precipitation-hardenable or heat treatable alloys, 2XXX, 6XXX and 7XXX. Table 1.5 lists the designations of all aluminum alloys and the corresponding alloying element. The non-heat-treatable alloys are those that are hardened by work hardening and SSS. The precipitation-hardenable alloys are hardened by the precipitation of fine, evenly distributed matrix and grain boundary particles and attain the highest strengths of the aluminum alloys.

Table 1.5. Designations for wrought aluminum alloys. [4]

Series	Aluminum Content or Main Alloying Element
1XXX	99% Aluminum
2XXX	Copper
3XXX	Manganese
4XXX	Silicon
5XXX	Magnesium
6XXX	Magnesium and Silicon
7XXX	Zinc
8XXX	Others
9XXX	Unused

Table 1.6. Temper designations for aluminum alloys. [4]

Suffix letter F, O, H, T, W indicates basic treatment condition	First suffix digit Indicates secondary treatment used to influence properties	Second digit for condition H only indicates residual hardening
F – As-fabricated O – Annealed-wrought products only H – Cold-worked, strain hardened		
	1 – Cold worked only 2 – Cold worked and partially stabilized 3 – Cold worked and stabilized	2 – ¼ hard 4 – ½ hard 6 – ¾ hard 8 – ¾ hard 9 – extra hard
W – Solution heat treated		
T – Heat treated, stable		
T1 – Cooled from an elevated temperature shaping operation + natural aged		
T2 – Cooled from an elevated temperature shaping operation + cold-worked + natural aged		
T3 – Solution treated + cold-worked + natural aged		
T4 – Solution treated + natural aged		
T5 – Cooled from an elevated temperature shaping operation + artificial aged		
T6 – Solution treated + artificial aged		
T7 – Solution treated + overaged		
T8 – Solution treated + cold-worked + artificial aged		
T9 – Solution treated + artificial aged + cold-worked		
T10 – Cooled from an elevated temperature shaping operation + cold-worked + artificial aged		

1.4.3.1. Aluminum Alloy 2024

Aluminum alloy (AA) 2024 is the most widely used of the precipitation-hardenable 2XXX-series. Alloying additions of copper and magnesium, possessing relatively high rates of diffusion in aluminum, allow for precipitate formation during aging heat treatment. Aging of AA 2024 produces the following precipitation structure sequence:

$$\text{Solid Solution} \rightarrow \text{GP} \rightarrow S' (Al_2CuMg) \rightarrow S (Al_2CuMg).$$

Enriched with solutes, the Guinier-Preston (GP) zones is the initial step involving the redistribution of solute atom within the solid solution matrix. Distortion of the lattice accompanies GP zones with the local segregation of solute atoms. Increased strength is associated with the production of a new solute-lattice interface and also due to the increased stress required for dislocation motion through region of high lattice distortion. The transition precipitate, *S'* is coherent with the matrix while formation of the equilibrium eutectic *S* phase results in loss of coherency.

AA 2024 is typically used in the -T3 temper (see

Table 1.6) which gives the alloy moderate strength and good fracture toughness. The -T8 temper, which reduces the number of and size of grain boundary precipitates, is also often used for when stress-corrosion cracking is a concern.

Titanium is added for grain refinement while manganese, chromium and zirconium additions to aluminum allow for dispersoids to form such as $Al_{20}Cu_2Mn_3$, $A_{18}Mg_3Cr_2$, and Al_3Zr. Iron and silicon are impurities that are avoided due to their formation of intermetallics, Al_7Cu_2Fe and Mg_2Si, respectively, that reduce fracture and fatigue toughness. [9]

Incipient melting is the onset on liquid phase formation. For AA 2024, incipient melting can occur at the grain boundaries where the eutectic *S* phase is likely to form. The *S* phase has a eutectic melting temperature of 500 ˚C (932 ˚F) and if AA 2024 is reheated rapidly to the eutectic temperature, *S* phase will melt instead of dissolving into solution. When the eutectic liquid solidifies, a rosette structure forms during cooling, after reheating. Other features, indicative of overheating, are excessive void formation, segregation, blistering, cracking and/or severe oxidation. [10]

Intergranular corrosion (IGC), the preferential attack of grain boundaries and/or regions adjacent to the boundaries, is due to the grain boundary area becoming anodic to the grain interior. All 2XXX series contain copper and precipitate $CuAl_2$, which increases the occurrence of precipitate-free zones (PFZs), making the 2XXX the most susceptible to IGC. Exfoliation corrosion is a type of IGC that contains delaminated features similar to broom-straw fracture. As corrosion progresses laterally (parallel to the surface) the corrosion products that form within the grain boundary have the effect of forcing the metal away, contributing to a layered appearance.

Chapter 2

Literature Review

2.1. Post-accident Investigations of Ti-6Al-4V Response to Atmospheric Re-entry

2.1.1. Discovered Char Layer Deposits on Overhead Windows

An investigation of charred deposits seen on fragments of overhead crew module Windows 7 and Window 8 were conducted by Olivas. [11] The overhead windows are comprised of a thermally tempered aluminosilicate pressure pane, a redundant fused silica pane, and a thermal fused silica pane. Samples of the window with charred deposition were prepared for evaluation using optical microscopy (OM) and transmission electron microscopy (TEM). The sample was categorized into four regions: the glass of the window, an inner layer, an outer layer, and a porous layer. With use of Selected Area Electron Diffraction (SAED) the inner layer was identified to be titanium dioxide, (TiO_2, rutile) with equiaxed grains near the glass substrate and irregular, elongated grains away from the

glass. The outer layer contained acicular TiO_2 grains and an aluminosilicate phase ($Al_{4+2x}Si_{2-2x}O_{10-x}$, mullite). Applying a ternary phase diagram for the Al_2O_3-SiO_2-TiO_2 system, its estimated that recrystallization occurred in the range of 1500-1700 ˚C (2730-3090 ˚F), and under the assumption that the inner and outer layers were molten at a certain point, it is estimated that they were above 1700 ˚C (3090 ˚F) before deposition to the window.

The composition of a 2XXX series aluminum alloy comprised of the porous layer. It was reasoned that this layer came from an aluminum alloy component as molten, or semi-molten, particles. The morphology of this layer was nondescript, and it is expected that the aluminum alloy deposited on the overhead windows from a source with a significant distance from the window or possibly from other debris in the travel path of the window. It is also reasoned that the source of the porous layer deposition may have been in aggressive motion with the window, but it could be concluded which, if not all, processes were involved in the porous layer deposition event. The charred deposits were only seen on the overhead windows of the orbiter, suggesting that the windows were intact during deposition process. The closest source of titanium to the overhead windows is the payload bay door latch rollers with is secured along the ring frame bulkhead made primarily of AA 2024. Due to the relative melting temperatures of aluminum and titanium, the sequence of titanium depositing before is unexpected. It suspected that the Ti-6Al-4V of the rollers experienced bulk metal combustion, characterized by the reaction surface boiling and ejecting

a spray of molten particles, which may continue to burn and become fully oxidized, converting metallic titanium to a titanium oxide. [11]

The melting temperatures of these two alloys, seen in in Table 1.2. are lower than Ti-6Al-4V therefore should exhibit the same, if not more, thermal damage than the titanium material of the roller. The thermal conductivity is lower than titanium, so the lack of damage to Inconel cannot be explained as heat shunting (withstanding higher heat rates because it created a heat sink).

2.1.2. Computational Fluid Dynamics Thermal Analysis of Payload Bay Door Rollers

Computational fluid dynamics (CFD) analysis of a PLBD was conducted by Johnson Space Center Applied Aerosciences and Computational fluid dynamics Branch. Testing was carried out at an orientation for which the face of the roller had an orthogonal geometry into the direction of heat flow. The heating rates and temperature distribution were calculated for Mach 10.52. The results of the CFD analysis showed that the melting temperature of titanium could be reached at Mach numbers above 10 and with pressure of flow, ablation is likely to occur (forcing away molten material). The Object Re-entry Survival Analysis Tool (ORSAT) was also used for analysis, and when compared to CFD analysis, the results were comparable. Heating rates were calculated traveling radially outward from the center of the roller face, and the results found that heating rates

increased and peaked as the heat flow reached the edge of the interior cylinder, then again when heat travelled to the outside edge of the outer sleeve. The amount of material loss due to heating rates alone in the short amount of time that the roller face was in oriented in the vector velocity direction seems improbable, so other heating events should be considered for cause of the significant thermal erosion experienced by the rollers.

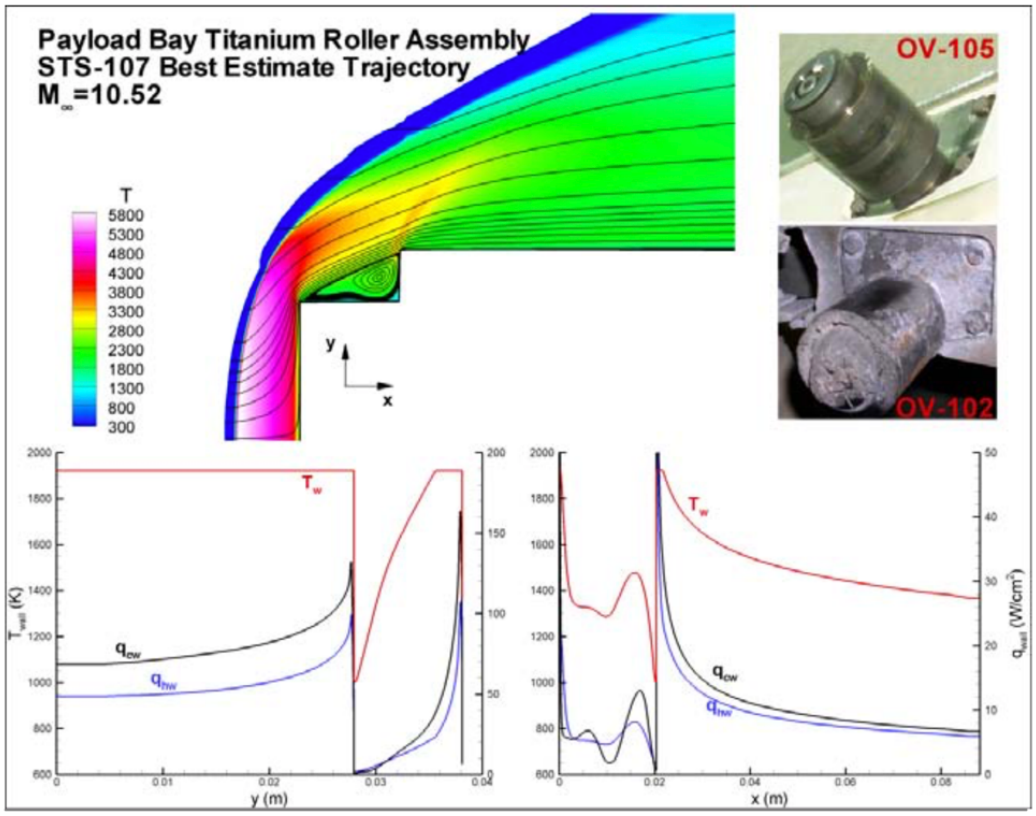

Fig. 2.1. CFD analysis at the tip of the payload pay door roller for orthogonal geometry into the direction of travel at M = 10.5.

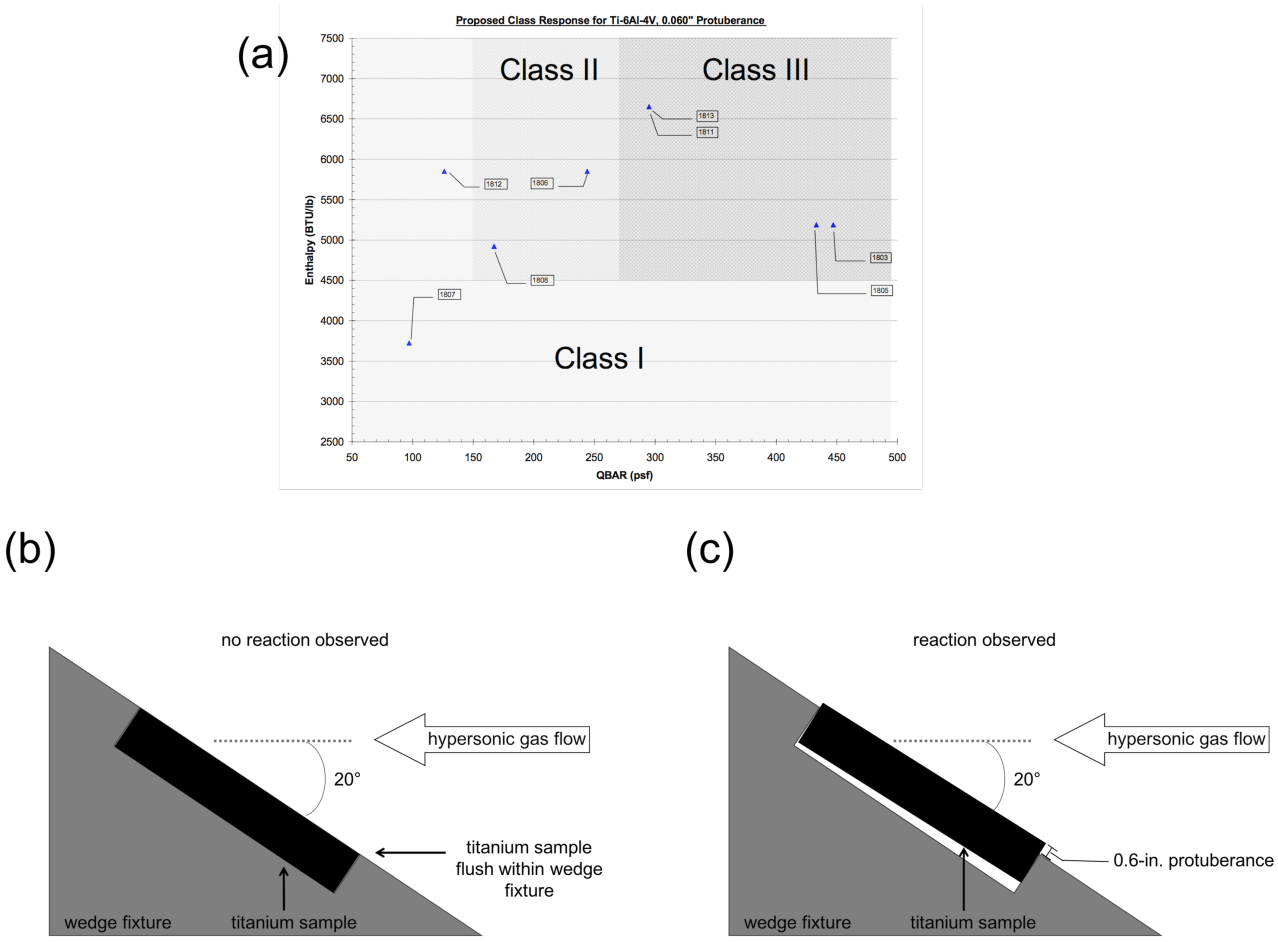

Fig. 2.2. (a) Results presented for Ti-6Al-4V samples (with 0.06-in protuberance) within representative boundary regions where passivation, ignition and combustion may result as theorized though testing. Adapted from [12] (b) Arc-jet sample schematic, titanium sample (black) with a flush configuration with wedge holder; (c) Arc-jet sample schematic, titanium sample with 0.06-in protuberance.

2.1.3. Study of Titanium Combustion in Simulated Entry Environments

Investigation of titanium response to simulated entry environments revealed that ignition and combustion is possible for certain orientations at

specific enthalpy and pressure conditions. Testing conducted by Olivas et. al. [12] was performed at the Boeing-St. Louis (Boeing-STL) Large Core Arc Tunnel (LCAT) plasma arc facility verified by NASA Atmospheric Re-entry Materials and Structures Evaluation Facility (ARMSEF) for accuracy.

The objective of the investigation was to evaluate the potential of Ti-6Al-4V to undergo ignition and/or combustion under conditions simulating re-entry of the *Columbia*. From the testing of samples in different configurations representative to that which *Columbia* experienced during re-entry, certain conditions were identified under which ignition/combustion responses were observed. Material response was classified under three types, Class I, Class II and Class III. Class I was characterized by relatively stable oxide layer formation that remained intact, re-forming even after spalling, during exposure to flow conditions. Class II behavior response showed a secondary increase in temperature occurring above the β transus temperature, 1065 ˚C (1950 ˚F). This secondary increase in temperature is followed by a slow increase in sample temperature until melting occurs. Class II behavior did exhibit oxide growth, but increased heating rates did not allow for a stable oxide layer to form. Instead, the oxidizing reaction at the surface appeared to initiate an exothermic response, increasing the local temperature at the surface to alloy melt temperature. Class III behavior was similar to Class II in that a secondary increase in temperature was also observed at or near the β transus temperature, the difference being that after this initiating event, an exponential temperature excursion resulted,

achieving temperatures significantly above melting. The samples classified by Class III behavior experienced temperatures above 3200 ˚C (5800 ˚F). The reaction was visually characterized by highly luminous spalled material, more intense than the spalled material seen from melting in Class II. Test samples from Class III never achieve steady state melting or oxide growth.

The test samples that were originally flush-mounted exhibited only Class I behavior. After observing the exacerbation of heat flux for a sample slightly raised in relation to mount, the subsequent samples were oriented similar to this, with a 1.5-mm (0.060-in) protuberance exposed to flow conditions. These test specimens, with 1.5-mm (0.060-in) protuberances, showed Class I, Class II and Class III responses and are the only samples included in the summary below. From this observation, it was implied that geometry along with enthalpy and pressure conditions, played a role in material behavior during the re-entry event. The results of this testing revealed the potential for titanium to undergo ignition and combustion with conditions simulated to a re-entry environment, and the temperatures observed during the arc-jet study, confirmed that Ti-6Al-4V components of the *Columbia* likely experienced Class I, Class II and Class III behavior during re-entry exposure.

2.2. Broom-straw Fracture & Aluminum Debris Analysis from *Columbia*

Evaluation of sub-structural aluminum debris collected from Space Shuttle *Columbia* indicated "broom-straw fracture" of AA 7075 seat legs. [13] Though the term, broom-straw is used in the CCSIR report, it is infrequently referenced in literature and the mechanism behind this fracture mode has not been fully described. The fragmented-type features are not discussed in literature, but in an aircraft fire investigation report [14], broom-straw fracture was described to occur for any near-molten aluminum subjected to high impact loading, causing a feather-like appearance to fracture surfaces. The 1985 report further concluded that broom-straw fracture was evidence of an in-flight fire preceding aircraft impact. When the aluminum endures high impact, the partially melted metal is strained and fractures in a delaminated manner.

A 1991 aircraft investigation report [15] characterized an aluminum fracture mode phenomenon as a result of short term creep, defined as extensive distortion over a short period of time at elevated temperatures and high stress. Identification of short term creep was described in the report as gross distortions and stretching, and fracture surfaces resembling "pulled taffy" or "bullet points". The theory for this type of fracture was suggested in the report to be due to in-flight fires causing the aluminum structures to partially melt, and when subjected to the shock of ground impact, the aluminum fractures in a broom-straw manner due to its partially-melted state.

The post-accident CAIB evaluation of shuttle debris attributed incipient melting as cause for broom-straw features. Microstructural analysis of aluminum debris items containing the “unique delamination features” was performed by NASA Langley Research Center [16] and it was reported that for debris samples, composed of 2XXX and 7XXX aluminum alloy, the delamination features were in result of crack propagation occurring along high angle grain boundaries (relative mis-orientation $\geq$ than 15˚), as observed with generated inverse pole figures. [16] Adjacent to areas of prevalent intergranular cracking, it was noted that the grain boundaries contained heavy precipitation, with certain alloys exhibiting significantly more precipitation. An association was made between the increase in second phase particles and exposure to higher temperatures or an increase in exposure duration.

Later investigations of debris recovered from *Columbia* provided general conclusions for failure observed in aluminum structures. Although no mention of delamination, or broom-straw fracture, was reported, it was clearly realized by the presented data that the aluminum debris contained broom-straw fracture features. The authors concluded that the failure of aluminum structures involved localized heating that caused grain boundary liquation of second-phase particles, resulting in void formation and intergranular rupture. [17, 18]

2.3. Titanium Oxidation

With the widespread use of metals and their alloys, oxidation behavior is an important field of study. The incorporation of oxygen at the titanium surface is a combination of forming an oxide layer and dissolution of oxygen into the metal. The mechanism at which the two events occurs depends upon temperature, pressure, duration of oxidation, metal condition, and alloying elements. Although, the proposed regimes for oxidation were developed from studies involving oxidation in pure oxygen or air, in a steady state environment, the information presented still serves useful in appreciating the effects of temperature on the rate of oxidation.

Oxygen solubility is high for titanium, and at room temperature forms rutile, TiO_2, a surface oxide layer. Rutile, the most common titanium oxide, is a thin passive layer that provides protection from further oxidation and corrosion. Fig. 2.4 displays the Ti-O phase diagram that shows several stable oxides in addition to the low temperature TiO_2, that can be formed such as Ti_2O, TiO, Ti_2O_3 and Ti_3O_5, and Ti_nO_{2n-1} ($4 < n < 38$) for oxidation occurring above 1000 ˚C (1832 ˚F).

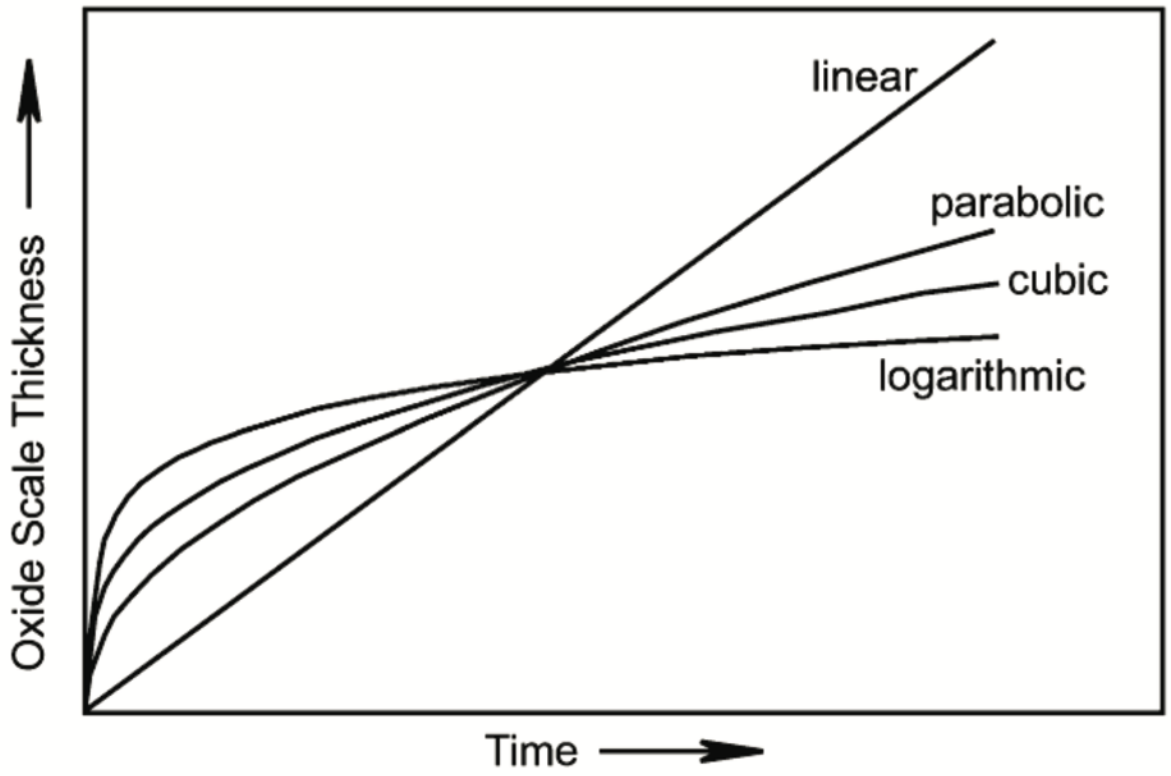

Fig. 2.3. Schematic representation of variation of oxide thickness with respect to oxidation duration for different oxidation rate laws. [19]

Studies conducted by Kofstad et al. [20, 21] have shown commercially pure (CP) titanium oxidation to follow a logarithmic rate law below 400 ˚C (750 ˚F) and within the oxidation temperature range of 400 to 600 ˚C (750-1110 ˚F) a cubic rate law is obeyed followed by parabolic behavior from 600-700 ˚C (1110-1290 ˚F). Fig. 2.3 displays a schematic representation of the oxidation rate laws and Fig. 2.4 displays the Ti-O phase diagram. When oxidation is prolonged within the parabolic rate law regime, oxidation is seen to shift to a pseudo-linear behavior.

At temperatures above 900 ˚C (1650 ˚F) the oxidation rate is linear and then progressed into a slower rate at a prolonged oxidation duration.

Logarithmic oxidation is described as the formation of the thin rutile formation while the cubic and parabolic oxidation rate is associated with the formation of a less protective rutile and simultaneous diffusion of oxygen through the oxide layer, into the metal where the brittle, oxygen enriched α-case layer is formed. The transition from cubic to parabolic is defined by temperature and oxygen content, as the cubic oxidation rate is decreased with an increase in temperature and oxygen. The parabolic oxidation is believed to be the simultaneous occurrence of oxide formation and oxygen dissolution. At increasingly elevated temperatures, the rutile becomes porous and develops cracking due to the stresses at the oxide/α-case interface, resulting in the transition into the linear rate of oxidation. [21] Oxidation within the linear rate law regime is associated with an increase in rate and oxidation proceeds by oxygen dissolution into the metal, resulting in $TiO_{0.35}$ at the surface and at this time, increased oxidation occurs. It has been proposed that at when the exterior composition reaches $TiO_{0.35}$, the oxide scale may develop cracking as the growth of stresses from expansion of the lattice occurs by oxygen dissolution. The newly formed detached surface will then undergo rapid oxidation due to the sudden availability of oxygen. [20, 21, 22, 23]

A preferred orientation of the oxide stunts the titanium diffusion into the inner surface of the oxide. Above 900 ˚C (1650 ˚F) the preferred orientation is less

apparent so an increase in oxidation occurs, switching from the parabolic to linear regime due to the cracking of the scale from increased growth. [24, 25] There is a formation of a porous inner layer and recrystallized outer layer and it opens up paths for increased oxygen diffusion. Kofstad showed that the occurs when the composition of the outer layer become $TiO_{0.35}$ and the layer starts to develop strains and stresses that lead to the cracking of the oxide scale if oxygen dissolution continues so the linear regime is governed by oxide nucleation and growth. [21]

Vaquila et. al. [26] and Biswas et. al. [27] studied the oxide behavior during oxidation. Vaquila stated that titanium oxidation at room temperature is characterized by one oxide phase, TiO_2. When oxygen exposure occurs at high temperatures, above 350 ˚C (660 ˚F), there is no saturation of oxygen at surface. Above 450 ˚C (840 ˚F), no oxygen is detected at the surface and Ti_2O_3 is the present oxide. [26]

Oxidation at 400-600 ˚C (750-1110 ˚F) for 25-60 h resulted in an adherent oxide surface, Ti_2O_3 and TiO_2. Oxidation at 600 ˚C (1110 ˚F) for 60 h resulted in microcracks and high hardness. [27] The oxidation of titanium alloys does not vary greatly from that of CP titanium. Studies featuring Ti-6Al-4V, conducted by Frangini, Guleryuz and Cimenoglu, and Sefer, observed temperature regimes that closely agreed with the above rate law behavior. [28, 19, 29] A multi-layered oxide scale composed of TiO_2 and Al_2O_3 was reported in the work of Du et. al.. [30] It was described that within the range of 650-850 ˚C (1200-1560 ˚F) the formation

of TiO_2 separates the bulk metal from the environment, providing a gradient in oxygen partial pressure that decreases moving away from the oxide scale into the bulk. The oxygen partial pressure at the gas/oxide interface is high, allowing the formation of Al_2O_3 on top of the TiO_2 scale. Pitt and Ramulu [31] observed the influence of microstructure on oxidation behavior. It was reported that the fine grained Ti-6Al-4V microstructure demonstrated faster oxidation kinetics compared to a coarse-grained Ti-6Al-4V microstructure.

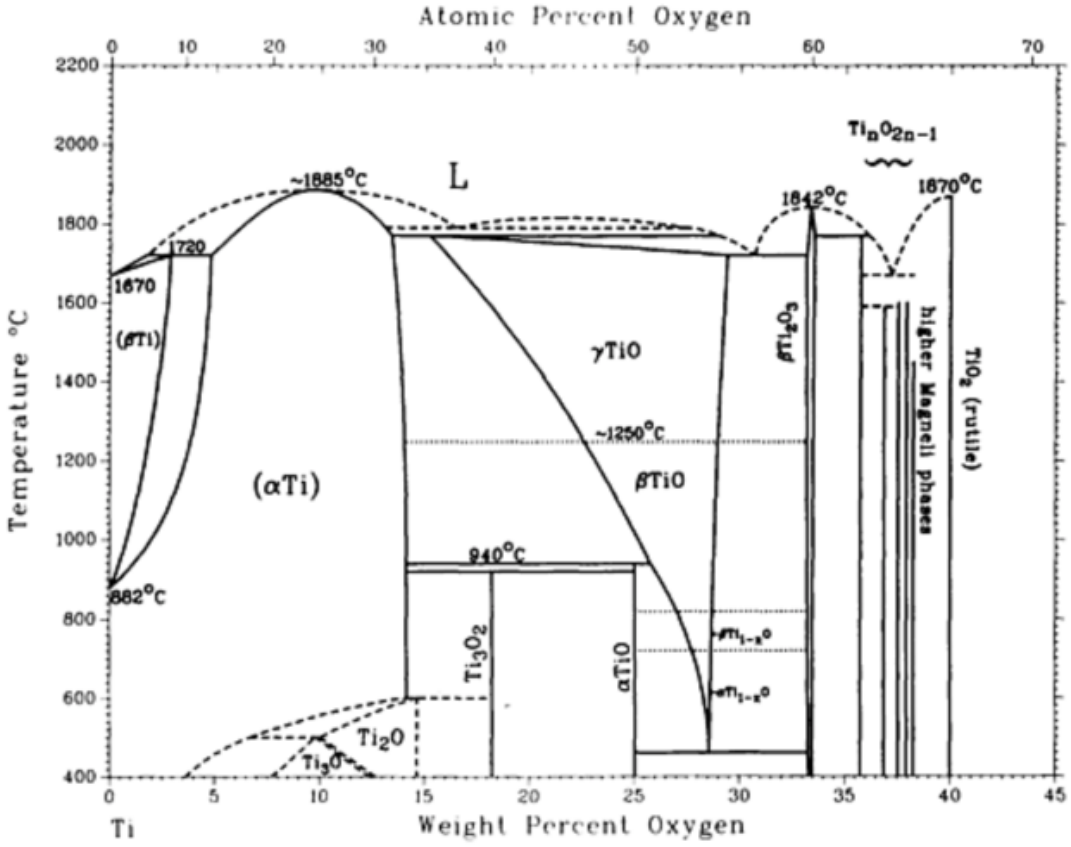

Fig. 2.4. Ti-O phase diagram. [7]

2.4. Titanium and Gaseous Nitrogen

Titanium has demonstrated a strong affinity for nitrogen and forms a nitride case of high hardness similar to the α-case formation in the presence of oxygen. Nitriding of titanium resulted in the formation a surface nitride layer consisting of Ti_2N and TiN. [32] [33] In addition to oxygen, nitrogen can also dissolve within burning molten metal particles and a ternary metal-gas solution can form for metals like titanium. [34] When the burning metals becomes saturated with oxygen or nitrogen, changes in the surface reaction rate and vapor phase reaction rate occurs. The rate at with oxygen or nitrogen dissolves into the surface decreases as the metal reaches saturation.

Deevi et. al. [35] reported that the reaction between titanium and gaseous nitrogen, before melting, produces a layer of TiN at the surface and a solid solution forms. At higher temperatures, the titanium of the TiN surface layer melts into which nitrogen dissolves. When the temperature is sufficiently high to melt titanium before the formation of TiN layer, the titanium is saturated with dissolved nitrogen.

Deevi proposed a model in which the surface layer dissolves to form a solid solution and then reappear when the solid solution becomes saturated. As the interaction between titanium and nitrogen progresses, a thick surface layer is formed and bulk contains a solid solution of nitrogen and titanium and the surface layer grows. Titanium powder, pressed into cylindrical specimens were ignited in 99.97% N at 0.101 MPa (14.7 psi). Titanium ignition was accomplished

by heating the titanium at one end by radiation. X-ray diffraction analysis showed the presence of minor amounts of TiN, the major phase being titanium.

Nitrogen, as well as oxygen occupies octahedral interstitial sites within hcp metals. Experiments performed by Montanari et. al. [36] demonstrated lattice expansion at high temperatures as a result of thermal effects and gas absorption. After cooling, residual expansion was observed, due to entrapped gas remaining within the lattice. Expansion due to gas absorption was greater for powder Ti-6Al-4V than for bulk Ti-6Al-4V samples.

2.5. Titanium Ignition and Combustion Behavior

Although bulk metal combustion dates back to 1782 when Ingenn-Hausz heated iron and steel in oxygen [37], the complex mechanism still remains poorly understood. Self-ignition of reactive metals is of great concern, especially when a reactive metal, such as titanium, is found in several applications in which ignition poses a safety risk.

Ignition of pure titanium occurs when heat generated by oxidation exceeds heat loss by way of conduction, convection and radiation. Beyond this, the metal is driven into thermal runaway due to the reaction rate's exponentially dependency upon temperature. Acceleration of the reaction reaches a

catastrophic oxidation level, exothermic self-propagating combustion occurs, increasing to the metals vaporization temperature. [38]

Extensive research has been dedicated to the combustion of metal particles due to its application is several industries, while bulk metal combustion has received far less focus. Fine metal particulates undergoing combustion are at a relatively uniform temperature while combustion of bulk metal involves a run-away exothermic reaction, just at the surface; the interior of the metal, away from the reaction, is at a significantly decreased temperature.

Markstein and Reihl [39, 40] described reactivity of metals susceptible to combustion. Ignition is the onset of reactivity and characterized by exothermic oxide formation. Combustion is associated with the rapid emission of heat and light, with transformation to a molten state.

Strobridge [41] stated 1600 ˚C (2900 ˚F) as the ignition temperature for titanium if air at 0.101 MPa (14.6 psi). He described that with the addition of energy and high pressure, the temperature decreases. Other factors influence the ignition reaction includes concentration of oxygen, and gas velocity but other factors are also involved: size, shape, thermomechanical processing etc.

2.5.1. Temperature Influence on Ignition

Tench, et. al. [42] studied the combustion behavior of 2.886-cm (1.125-in.) diameter rods heated by a radio frequency (RF) induction heater in 0.201 MPa (30

psig) of oxygen. A 25.4-mm (1-in.) length rod section did not burn, while a 12.7-mm (0.5-in.) length section of rod burned vigorously. Ignition was also observed for a 12.7-cm x 12.7-cm x 0.318-cm (5.0-in. x 5.0-in. x 0.125-in.) plate when fractured in 0.38 MPa (55 psig) of oxygen. [42] Tench analyzed the combustion products and discovered titanium oxides of varied stoichiometry. This was explained by the variable occupancy of oxygen at varied lattice sites resulting in changes in lattice parameters.

Branch tested titanium in 99.5% oxygen at a pressure of 0.04-0.40 MPa (5.9-58.7 psi) (heterogeneous oxidation versus homogenous). Ignition temperature below, or in range of, melting temperature, was expected for metals exhibiting heterogeneous oxidation with non-protective oxide layers.

Wolf proposed that rapid heating rates can reduce ignition temperature. Wolf proposed that low ignition temperatures imply ignition is precipitated by localized deposition of heat in small hot spots with a rapid local oxidation rate and thermal runaway. Under rapid heating, Wolf showed CP titanium and Ti-6Al-4V to have an ignition temperature of 750-800 ˚C (1380-1470 ˚F), from testing 99.8% CP titanium in a sealed chamber of oxygen at 0.027 MPa (3.9 psi). The specimens ignited when subjected to heating rates of 40 ˚C/s (100 ˚F/s) or greater in 0.0253 MPa (3.7 psi). [43, 44, 45, 46]

Hill [47] tested titanium wires with 1.588-mm (0.0625-in.) diameter and 50.8-mm (2.0-in.) length. The specimens were heated while immersed in a static air, oxygen or nitrogen. At 3.44 MPa (500 psia), titanium ignited and burned

vigorously 1150 ˚C (2100 ˚F) in oxygen, and the same reaction occurred in the air and in pure nitrogen atmospheres.

Rozenband [48] subjected porous titanium plates to an oxygen environment and observed ignition temperatures of 170 ˚C (335 ˚F), 165 ˚C (330 F) and 270 ˚C (520 ˚F). Andrzejak [49] tested spherical titanium particles, 3.0-mm (0.118-in.) in diameter, by heating samples with a laser to 850-950 ˚C (1560-1740 ˚F), TiO_2 formed with an increase in temperature, when the sample reached 1400 ˚C (2550 ˚F), a sharp temperature rise occurred, leading to the self-acceleration of reaction. This was not the case when tested in pure nitrogen or argon.

2.5.2. Added Energy (fracture) Influence on Ignition

Littman [50] tested titanium alloy rods and sheets, including Ti-6Al-4V, and observed ignition occurring at free surfaces, upon surface fracture, when exposed to a certain oxygen pressure and temperature. Littman observed that the alloys all combusted the same, and that as the temperature increased, ignition occurred for decreasing oxygen concentration. Dynamic flow, versus a static condition, allowed for ignition to occur more readily. He theorized that molten titanium serves as a precursor for ignition, postulating that the increased oxygen solubility into the melt prevents the formation of a protective oxide layer.

Borisova [51] observed that titanium ignition occurs for an unoxidized surface within an oxidizing environment contained at least 35% oxygen

concentration. It was determined that titanium ignition occurs when a fresh surface was exposed to oxygen, due to fracture, as an oxide layer forms with a large heat release. Ignition was stated to be dependent upon the rate of oxidation, with the observation that ignition did not occur at atmospheric pressure but did occur in pressurized environments (associated with a high oxidation rate). Different concentrations of oxygen and nitrogen, determined that the critical oxygen pressure at which ignition occurs increases sharply with decreasing concentrations of oxygen, the critical oxygen pressure varying for each alloy. Increase in temperature decreases the critical pressure of oxygen required for ignition and a decrease in oxygen concentration increases critical temperature. [51] The critical oxygen pressure for CP titanium, ruptured at 20 ˚C (70 ˚F), was 0.20-0.25 MPa (29-36 psi) and for Ti-6Al-4V, the critical oxygen pressure was 0.8 MPa (116 psi). [51]

2.5.3. Gravity Effects

Abbud-Madrid et. al. [52, 53] conducted studies aimed to understand the effect of elevated (20-g's) and normal (1-g) on titanium ignition in pure (99.5%) oxygen at an absolute pressure of 0.101 MPa (14.6 psi). [53, 52] The increased buoyancy-induction convection rate resulting from elevated gravity was shown to increase the loss of heat away from the titanium rod, measuring 4-mm (0.16-in.) in diameter and 4-mm (0.16-in.) in length. The decrease in heating led to a

delay in ignition time at 3- to 5-g's. Faster ignition times were observed above 5-g's where increased convection promotes faster oxidation rate, i.e. increased heat generation that is likely to overcome the rate of heat loss away from the sample. Burning rates after ignition is also increased due to increased gravitation load pulling the molten products away from the surface, exposing fresh metal available for ignition.

2.5.4. Gas Velocity Influence on Ignition

Strobridge performed static tests in 0.101 MPa (14.6 psi), using a laser source for ignition. He observed melting and ignition with intense luminosity. A decrease in intensity was reported along with steady burning, followed by a violent ejection of particles, until quench. Dynamic tests in 1.01 MPa (146 psi) at a flow speed of 300 m/s (984 ft/s) revealed that pressure played more of a role than velocity. Ignition was possible at temperatures as low as 250 ˚C (480 ˚F). [41]

Bolobov [54] described that when a metal surface, free of an oxidation layer, is exposed to a critical oxygen pressure, ignition occurs. Bolobov later described that for bulk metal, ignition is hypothesized to occur when metal surfaces, free of an oxide film, are exposed to gas flow of a critical pressure. [55]

Bolobov stated that ignition occurs when clean surface is raised to critical temperature and exposed to oxygen. The pressure at which ignition occurs depends on temperature. As temperature is increased, the oxygen pressure

required for combustion is decreased. Stronger titanium alloys require increased stress for fracture, which increases the temperature of sample at fracture, allowing for a lower critical oxygen pressure. No ignition occurred with slow forming fracture. Bolobov observed a critical pressure of 7.7 MPa (1116 psi) and 3.1 MPa (450 psi) for CP titanium and Ti-6Al-4V, respectively, for testing at 27 ˚C (80 ˚F) and a gas flow of 340 m/s (1115 ft/s).

Bolobov performed ignitions studies of CP titanium and titanium alloy 13-mm x 30-mm x 2-mm (0.512-in. x 1.18-in. x 0.787-in.) plates, oxidized to form a titanium oxide coating. Other samples were coated with both nickel and copper, synthesized enamels or a fluoroplastic. The titanium plates were subjected to an oxygen and nitrogen flow at approximately 340 m/s (1115 ft/s) through a nozzle of 40 MPa (5801 psi) initial pressure and 26 ˚C (80 ˚F). Titanium ignited at various angles of attack and it was postulated that the mechanism of ignition was due to flow-assisted mechanical fracture of the surface oxide or substrate. The enamel and fluoroplastic coatings demonstrated a hindrance to ignition in an oxygen flow. Bolobov observed surface features at the incident of flow to vary with the angle of attack. At 90˚, microcraters were apparent, while at angles between 0˚ and 5˚, grooves were observed. The nature of the surface fracture upon attack was the same in nitrogen as in oxygen. [55]

Results of the study conducted by Harrison [56] showed combustion of bulk 1- and 0.5-mm (0.03- and 0.02-in.) diameter titanium wire occurred on the surface of molten metal with no substantial vaporization pointing to

temperatures remaining below boiling point 3200 ˚C (5800 ˚F) during combustion. Factors of combustion were observed to be oxide characteristics as well as the balance of heat produced and lost during oxidation. Harrison also stated a relationship between temperature gradients at the flame point with the velocity of combustion propagation, observing the frozen conditions of the wire post combustion. As the combustion process was extinguished, a solidified globule remained attached to the unburnt wire with an oxide layer of decreasing thickness observed along the length of the wire adjacent to the globule. The extent and thickness of the oxide layer provided an indication of temperature gradient present at the termination of the combustion reaction. The oxide layer measured thicker at lower oxygen concentrations and thinner at higher oxygen concentrations, which corresponds to lower and higher propagation velocities, respectively. At 85% oxygen, corresponding to the highest recorded velocities, the globule fell from the wire resulting in a steep thermal gradient that extinguished the combustion reaction, when the portion of the wire was small enough. [56]

Tanguay et. al. [57] tested titanium metal rods in shock-accelerated oxygen with shock waves ranging from Mach 4 to Mach 9. Titanium ignited at Mach 4 and the combustion region and material loss increased, with an increase in Mach. Combustion temperature was determined to be 2240 ˚C (4060 ˚F), below the melt temperature of titanium. A control experiment was conducted in which titanium was tested in at a Mach 9 shock wave in pure nitrogen. The luminosity and mass

loss observed for titanium ignition in the oxygen flow did not occur in nitrogen, proving that the ignition was primarily the result of the exothermic reaction of combustion and material ablation, resulting from the high enthalpy of flow was not a dominant factor. The same was determined by aeroballistics experiments performed by Higgins. [58] Higgins tested metal spheres of aluminum, zirconium and magnesium, measuring 1.27-cm (0.47-in.) in diameter, by launching the samples to velocities of 1.2-2 km/s (Mach 3.6-6.0) at a pressure of 0.101-1.01 MPa (14.6-146 psi). He reported that ignition required temperature of flow to exceed melting temperatures or boiling temperature, but not to exceed the adiabatic flame temperature. Combustion can only occur during a small range of Mach numbers. Aluminum and magnesium did not ignite in 0.101 MPa (14.6 psi) air for 12.2 km/s (40,026 ft/s), but the specimens did ignite in oxygen, at pressures of 0.101 and 0.507 MPa (14.6 and 73.5 psi), for a certain velocity of 1.8 km/s (5906 ft/s) and 1.3 km/s (4265 ft/s) respectively. It was established that luminosity observed was the result of ignition and not material ablation with a separate reaction occurring separate from the sample.

2.5.5. Particles in Air Flow

Gordon [59] studied the ignition and combustion characteristics of several metals, including titanium. Tests were performed by injecting metallic particles into a gas stream of oxygen. Gordon classified titanium as a nonvolatile

substance with a soluble oxide, characterized by easy ignitability and slow burning rates, with long burning times and sharp streaks that suggests ignition and combustion initiating at the surface.

Molodetsky et. al. [60] measured and analyzed the temperature and composition of titanium droplets formed by a micro-arc generator and ignited immediately upon its formation in air. The titanium particles were quenched at varied times during combustion and the internal structure was revealed to be mixtures of titanium, oxygen and nitrogen. The Ti-N and Ti-O phase diagrams are well established while less reliable data exists for the Ti-O-N phase diagram. The observed nitrogen-rich Ti-O-N phase was seen to form after ignition and disappear after prolonged combustion duration. Oxygen concentration increased with increased combustion times, while nitrogen concentrations increased and then slightly decreased. It was stated that during combustion, two radiation jumps occurred. The first jump was due to the release of nitrogen gas around 2300 ˚C (4170 ˚F) as opposed to the formation of Ti-N, as shown on the Ti-N phase diagram. The second radiation jump was the result of titanium oxide Ti_2O_3 formation and nitrogen gas release. This release of nitrogen was proposed to be responsible for the voids within the Ar-quenched particles. [60] Dreizin further described the mechanism of titanium combustion by characterizing the work of Molodetsky and other researchers studying aluminum, magnesium and zirconium and iron, summarizing two stages of metal combustion. Stage I of metal combustion involves vapor phase combustion and oxygen (and/or nitrogen

for titanium and zirconium) dissolution into the burning metal. For the small sized particles, the gas dissolution is uniform throughout the volume at high temperatures. Gas dissolution decreases as the metal-gas solution reaches saturation and the boiling point of the pure metal shifts with the change in metal-gas solution composition. These phase changes signify the onset of Stage II in which oxygen dissolution progresses until oxygen concentration is that of the stoichiometric oxide. Oxygen dissolution decreases with decreasing temperature thus when equilibrium concentration is achieved, gas dissolution is decreased to zero and the droplet temperature decreases rapidly resulting in a supersaturated solution. Due to the formation of the complex metal-gas solution during the first part of combustion, several sequential non-variant phase transitions occur, causing luminosity and temperature changes during combustion. [34]

Devito [61] tested titanium spheres, of smooth and rough surface texture, in pure oxygen at 27 ˚C (80 ˚F). The spheres with smooth texture consistently produced intense luminosity when tested at a velocity of 1400 m/s (4593 ft/s) and pressure of 0.525 MPa (76.1 psi). Testing at 1150 m/s (3773 ft/s) reaction and pressure of 0.5 MPa (72.5 psi) produced a reaction while no reaction was observed at the same pressure, but at a velocity of 1440 m/s (4724 ft/s) and 1400 m/s (4593 ft/s). Reaction occurred at the decreased velocity of 1400 m/s (4593 ft/s) when pressure was also decreased to 0.4 MPa (58 psi). No reaction occurred below 1100 m/s (3608 ft/s) and 300 kPa (44 psi). Devito observed that lowering

pressure to 125 MPa (18130 psi) required increased velocities for reaction to occur.

Anderson [62] studied titanium alloys combustion by subjecting airfoil specimens, 2.5-cm x 0.15-cm x 7.4-cm (1.0-in. x 0.06-in. x 2.9-in.), to a laser ignition source at 427 ˚C (800 ˚F), air pressure of 0.48 MPa (70 psia) and an air velocity of 213 m/sec (700 ft/sec). and 240 ˚C (400 ˚F), 0.62 MPa (90 psia), 122 m/sec (400 ft/sec) airstream. Titanium ignited in both test conditions. Ignition was higher for higher temperature condition.

Chapter 3

PLBD Roller Examination

3.1. Experimental Methods

3.1.1. PLBD Roller Surface Characterization

Bolts securing the port PLBD roller onto the X_o 582 bulkhead were mechanically detached from the base plate. An attempt was made to detach the roller from the base plate, revealing that the roller was attached to the base plate by a firm press fit. Using a wooden block to protect the surfaces of the roller, the PLBD roller was hammered out of the bulkhead.

Sample A was obtained by a transverse section made approximately 3.8-mm (1.5-in.) from the thermally degraded base of the cylindrically-shaped roller, referred to as the reaction front, outlined in Fig. 3.1a. An abrasive cut-off saw was utilized to carefully section the PLBD roller. This method of sectioning was chosen to avoid altering or destroying the microstructure of the materials. The cut, positioned between two bearings, was selected by measuring the telescoped

displacement of the sleeves, identifying a region to minimize damage to the internal structure. Upon sectioning, a metal spring was released from inside the roller and due to the removal of the molten metal section, the outer sleeves of the roller regained the ability to slide and rotate radially and axially. Sample A was lightly cleaned in an ultrasonic bath of ethanol for four 30-s intervals. In between each interval, the surface was inspected for signs of alteration or material loss.

For surface characterization of the isolated reaction front of Sample A, light optical microscopy (LOM) with a Keyence stereo microscope and scanning electron microscopy (SEM) with a Hitachi S-4800 microscope was employed. Chemical analysis of external surfaces was obtained by X-ray fluorescence (XRF) with an Olympus DELTA handheld analyzer, and X-ray micro-analysis with the EDAX TEAM energy dispersive spectroscopy (EDS) capability of the Hitachi S-4800 microscope. X-ray diffraction (XRD) was also employed by use of a Bruker Discover 8 X-ray diffractometer, utilizing CuK_{α} radiation, an angle range of 20° to 120°, a step increment of 0.05 and a count time of five degrees per minute.

Fig. 3.1b provides a forward-facing view of the reaction front with a clock face designation included for circumferential reference and quadrant delineation to identify reaction front surface regions: Quadrant 1 (Q1), Quadrant 2 (Q1), Quadrant 3 (Q1), and Quadrant 4 (Q1).

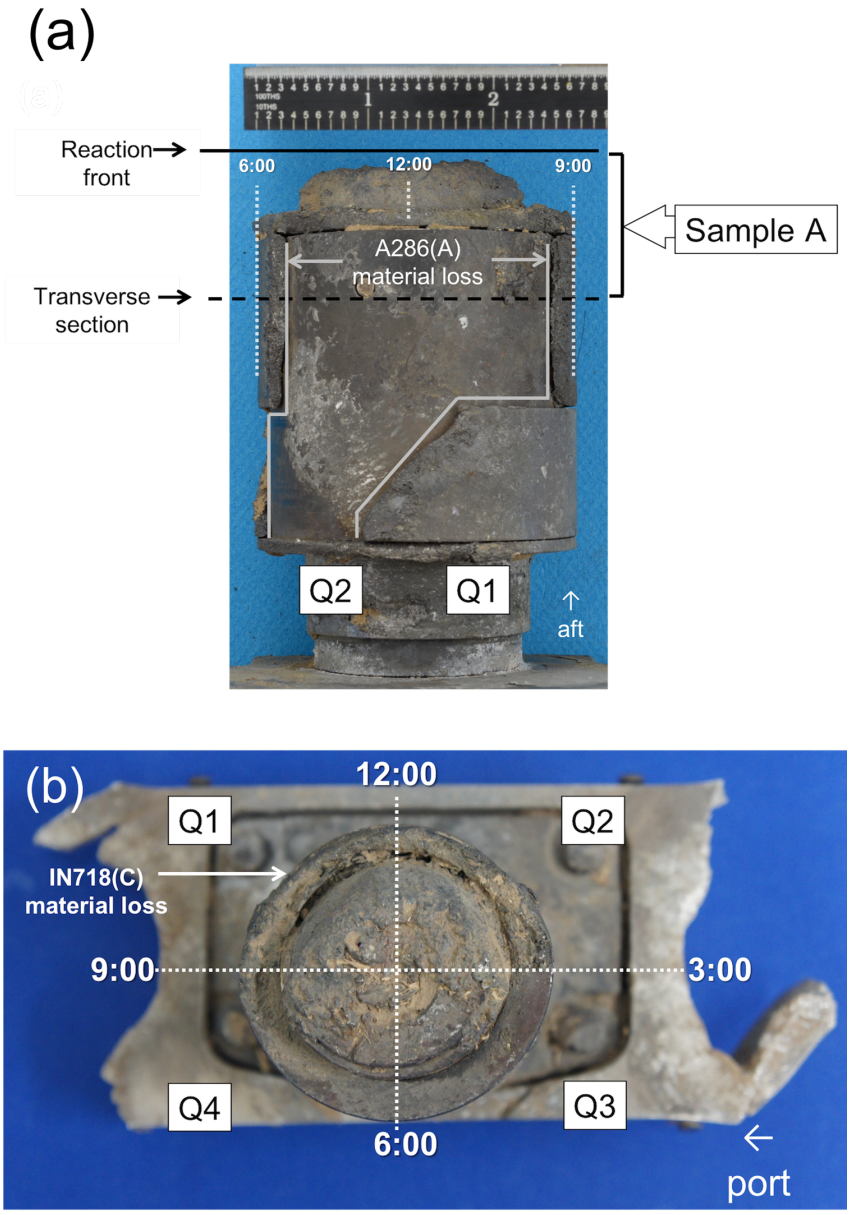

Fig. 3.1. As-received port roller recovered from Space Shuttle *Columbia*; (a) Sample A outlined in black (deck-facing) - note material loss of outermost A286 sleeve (b) Reaction front (forward-facing) with clock face configuration and quadrants (dashed white line) labeled: quadrant 1 (Q1), quadrant 2 (Q2), quadrant 3 (Q3), and quadrant 4 (Q4) – note material loss of IN718 sleeve shown.

3.1.2. PLBD Roller Microstructural Analysis

Fig. 3.2 contains sub-sections of Sample A1 which is the isolation of Q1 and Q4 by an axial section of Sample A from 12:00 to 6:00 using an abrasive cut-off saw at slow speeds. The sleeve contained in each sub-sample is indicated in Fig. 3.2. The alloy name is followed by a letter in parenthesis which refers to the sequential concentric position of the sleeve in accordance with the original roller construction, moving inward radially from (A) to (H), i.e. (A) refers to the outermost sleeve and (H) refers to the innermost sleeve component.

Upon sectioning, the three outermost sleeves A286(A), IN718(B), IN718(C) separated from the roller, the latter two remaining adhered together. The five innermost sleeves - CrIN718(D), Ti6Al4V(E), Ti6Al4V(F), IN718(G), and A286(H) – also remained adhered together by the re-solidified material (RSMM) deposition on the reaction front.

Standard metallographic techniques were used for preparation of samples. The Ti-6Al-4V sleeves were selectively etched with Kroll's reagent (46-mL H_2O, 3-mL HNO_3, 1-mL HF) and Kalling's No. 2 (5-g $CuCl_2$, 100-mL HCl, 100-mL C_2H_6O) was used for the spot etching of both IN718 and A-286 sleeves. Microstructural analysis was performed, using LOM with an Olympus PME 3 inverted light optical microscope, on the axial cross-sections of each sleeve in the more thermally affected region, Q1 and in the less thermally affected region, Q4, i.e. Ti6Al4V(E)-Q1 to be compared to Ti6Al4V(E)-Q4. The quadrant division is shown in a dashed white line. Due to the material loss observed for the A286(A) sleeve, the

microstructure will be evaluated on the transverse cross-section, (normal to the fracture surface plane). Features will be examined at the site of material loss in Q1 at approximately 10:00 and away from the damage at approximately 6:00 in Q4, as outlined in Fig. 3.3. The IN718(G) sleeve is an interior sleeve, located 2.54-cm (1.0-in.) away from the reaction front; the configuration of the roller is such that the G sleeve is inset, with no exposed surface area at the reaction front. Analysis of the sleeve was performed to appreciate any indication of heating in the region for a comprehensive understanding of thermal heating throughout the PLBD roller.

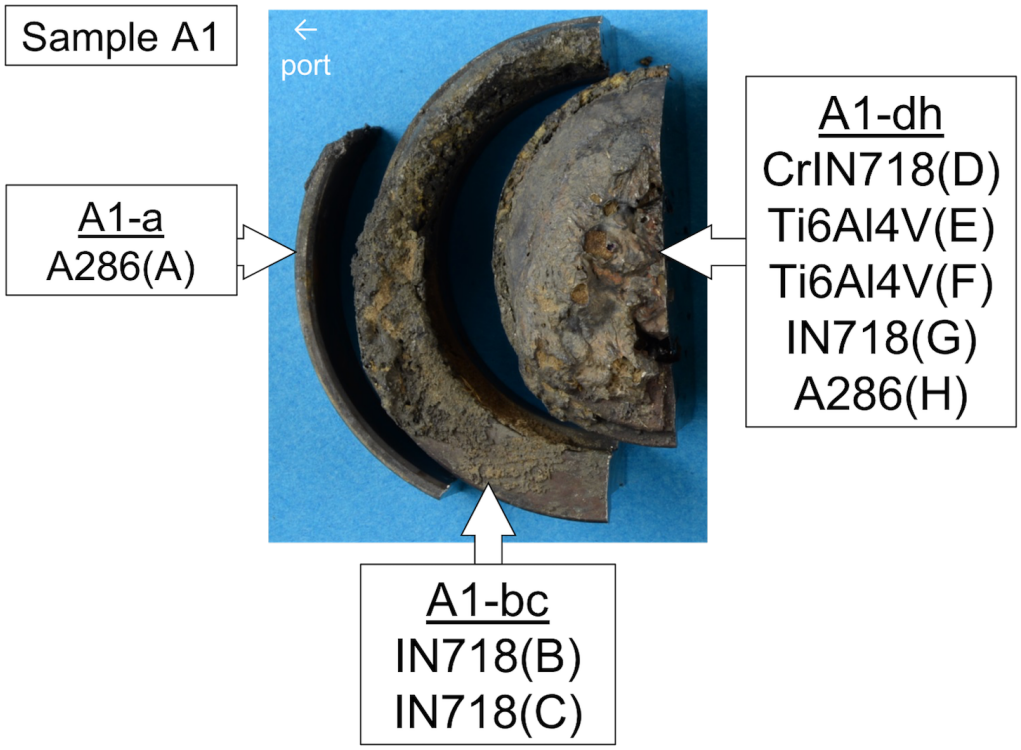

Fig. 3.2. Axial bi-sectioning of Sample A yielded Sample A1 to include sub-samples: A1-a, A1-bc, A1-dh; Sleeves contained within each sample identified by alloy type and sequential configuration in parenthesis, (A) to (H), outermost sleeve to innermost sleeve, respectively.

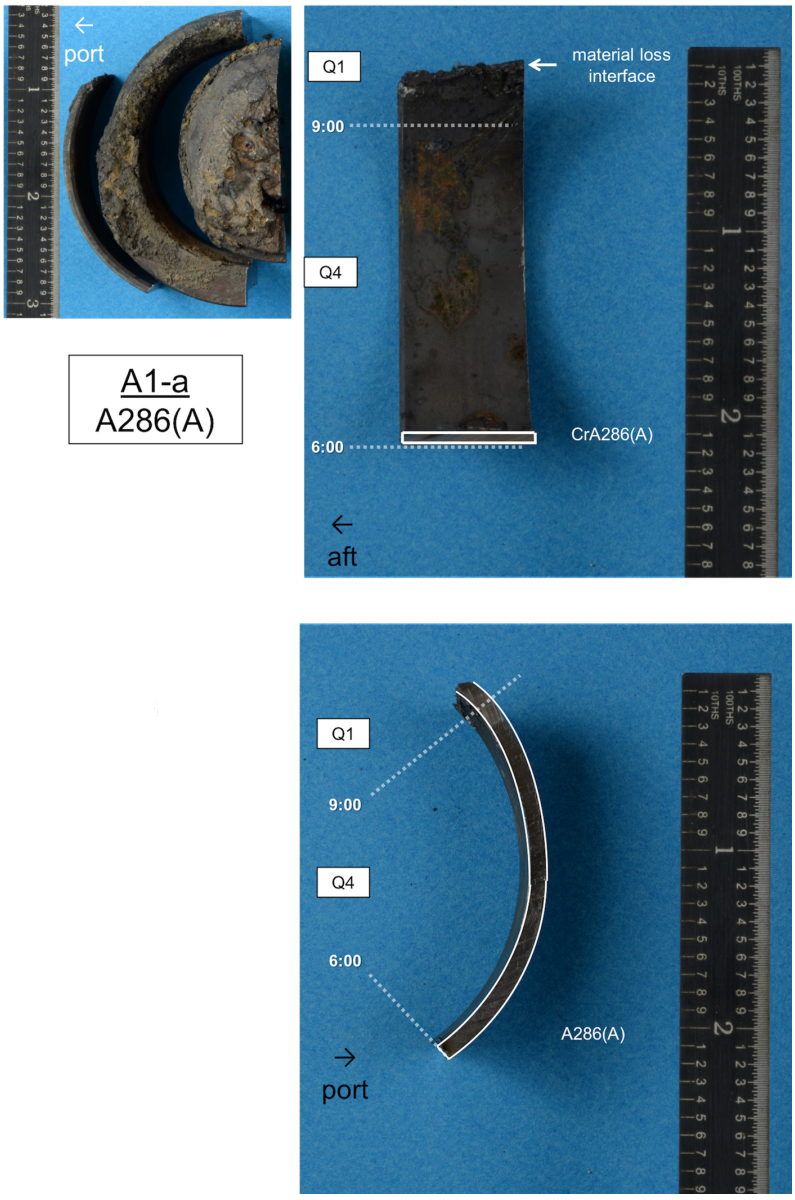

Fig. 3.3. Images of Sample A1-a containing A286(A) (a) forward-facing view (top left), ID wall and axial cross-sectional cut surface outlined in white (top right), (b) transverse cross-sectional cut surface from which microstructural evaluation was performed. Alloy type is indicated and labeled quadrant regions are divided by a dashed white line that also delineates the clock face configuration.

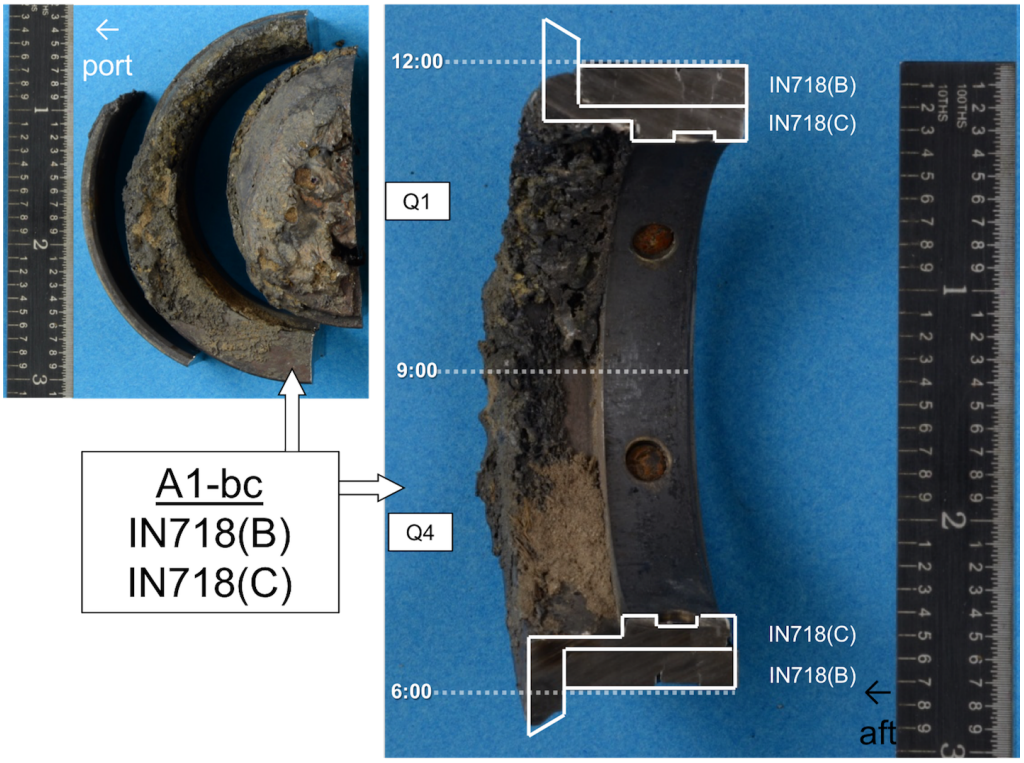

Fig. 3.4. Images of Sample A1-bc containing IN718(B) and IN718(C): forward facing view of reaction front (left), ID wall and axial cross-sectional cut surfaces outlined in white (right). Alloy type of each sleeve is indicated and labeled quadrant regions are divided by a dashed white line that also delineates the clock face configuration.

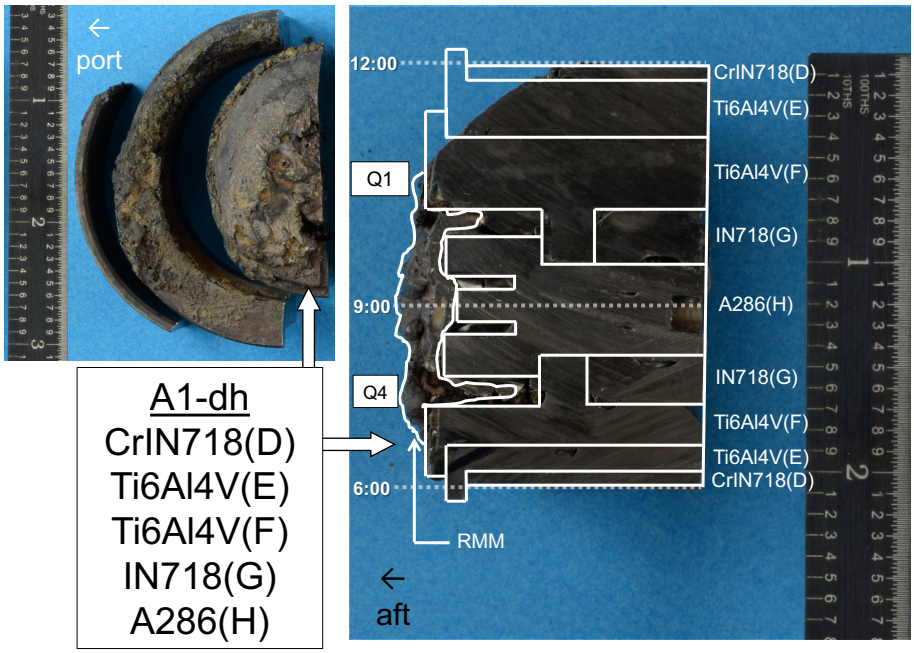

Fig. 3.5. Images of Sample A1-dh contained CrIN718(D), Ti6Al4V(E), Ti6Al4V(F), IN718(G), and A286(H): reaction front view (left image), ID wall and axial cross-sectional cut surfaces outlined in white (right image). Note variable wall thickness of the Ti-6Al-4V sleeves. Alloy type of each sleeve is indicated and labeled quadrant regions are divided by a dashed white line that also delineates the clock face configuration.

The sketches provided in this report were developed based on the cross-sectional measurements of the sample and aided by a design drawing provided by NASA. The overlays are not drawn to exact scale and should be used as a mapping reference only. The sleeve outlines were simplified to basic shapes that closely represent actual geometry and dimension, with disregard to the complexities of construction that include beveled edges, minor grooves, and internal fasteners.

Additional analysis includes SEM and backscatter scanning electron microscopy (BSE) using Hitachi S-4800 as well as an FEI XL30 scanning electron microscope. Chemical analysis involved use of EDS capability of both SEM microscopes and the use of XRD was carried out by the instrument and methods described previously.

Microhardness testing, performed axially along the Ti6Al4V(E) and Ti6Al4V(F) sleeves in mounted sample A1-dh, was carried out with a Vickers pyramid indenter using a Buehler MicroMet 3 Micro Hardness Tester. Measurements were obtained under indentation loads of 500-g with a 15-s dwell time.

3.1.3. Arc-jet Test Specimen Microstructural Analysis

Arc-jet test specimens, one from Class I, Class II, and Class III, and an untested control specimen were sectioned as shown in Fig. 3.6, for microstructural examination of the cross-section. Samples were vacuum-impregnation mounted in an epoxy resin, prepared using standard metallographic techniques and etched with Kroll's reagent.

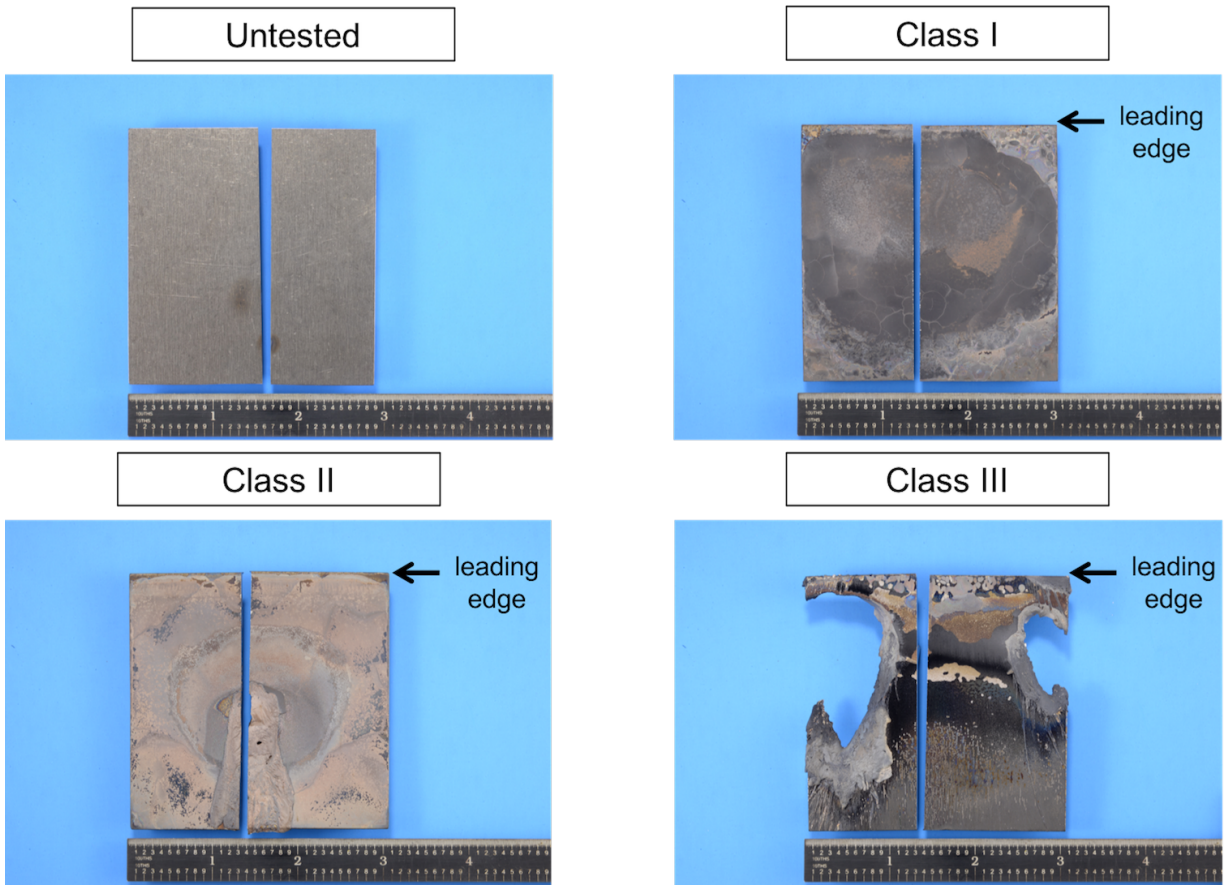

Fig. 3.6. Images of sectioned arc-jet samples: untested, Class I, Class I, and Class III, thickness.

3.2. Results

3.2.1. PLBD Roller Surface Analysis

The external surfaces of the port roller had a charred, dull appearance, with areas of discoloration and contamination. Severe material loss was

observed, with portions of its outermost A-286 sleeve absent, exposing the adjacent IN718(B) sleeve. The material loss of the outermost A286(A) sleeve was localized to the 10:00 to 2:00 regions, corresponding to regions of the roller that were oriented nearest to the overhead crew module windows during normal flight conditions, Fig. 3.7a. The material loss of IN718(C) sleeve is also apparent in the same region, with thickness measuring thinnest along 10:30 to 1:00 at 2.0-mm (0.08-in), and thickest, 3.6-mm (0.14-in.), in the opposite region, where minimal damage was observed.

Visible in Fig. 3.7b, the RSMM exhibited a slanting nature downward with its steepest region in Q1 and Q2 which also coincides with the area that A286(A) experienced significant material loss. In contrast, little to no material loss was seen in Q3 (Fig. 3.7e); the area contained no evidence of significant melting and little deposition of RSMM. With higher magnification, several cavities (Fig. 3.7d) were resolved on the reaction front, one of which, contained a purple patina interior wall coating, shown in Fig. 3.7f.

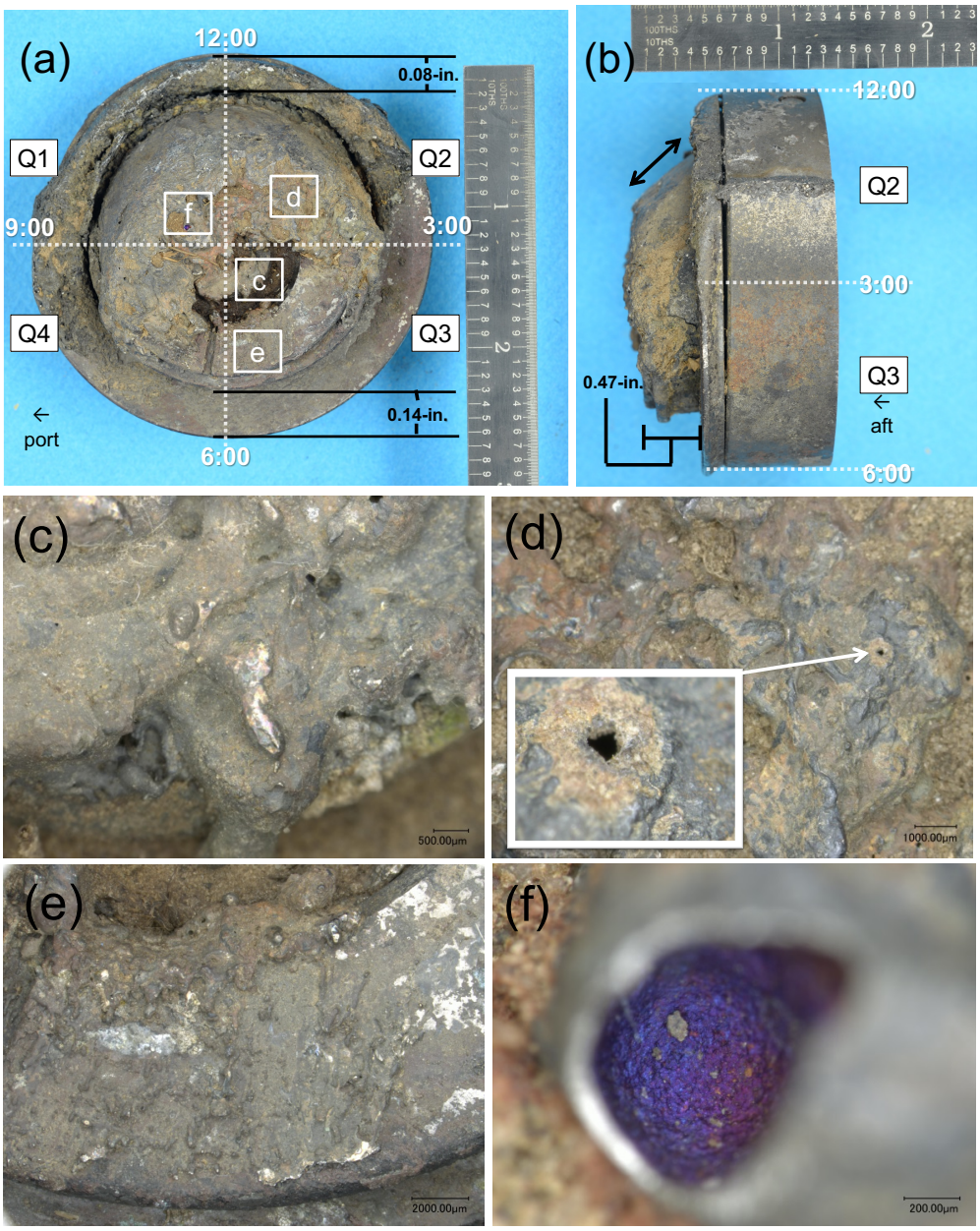

Fig. 3.7. Images of Sample A, thermal damage of reaction front (a) Thermal damage in Q1, Q2, and the inside perimeter of Q4; minimal damage observed in Q3 and outside perimeter of Q4 (b) RSMM of reaction front showing slanting characteristic (c)-(f) magnified images of reaction front corresponding to white boxed regions outlined in (a).

Averaged XRF results of the RSMM deposition on the reaction front can be seen in Table 3.1. The detection of titanium, aluminum, and vanadium are consistent with the Ti-6Al-4V composition, though a significantly high amount of aluminum was detected. While the presence of iron, chromium, and nickel are expected for superalloys IN718 and A-286, they were detected at decreased amounts. Copper and silicon, elements not native to Ti-6Al-4V, IN718 or A-286, were observed, with copper at a notably high concentration.

Table 3.1. Average Chemical Composition of Reaction Front - XRF

Ti	Al	V	Fe	Cr	Ni	Cu	Si
68.4	16.3	2.6	2.2	1.6	1.6	1.4	10.3

Analysis of the reaction front using SEM revealed varied surface features and texture. In the RSMM region of the reaction front, as well as in the degraded area of the outer sleeve, the surface contained a dimpled, porous texture, Fig. 3.8a-b. Throughout the entire sample, a globular morphology (Fig. 3.8c-d) was observed, ranging in size. Also observed in the thermally degraded area, was a ridged pattern, shown in Fig. 3.10a-b. On areas that exhibited little degradation, the surface exhibited mud-cracking, shown in Fig. 3.10c-d. Multilayered scales were also seen in several areas throughout the surface.

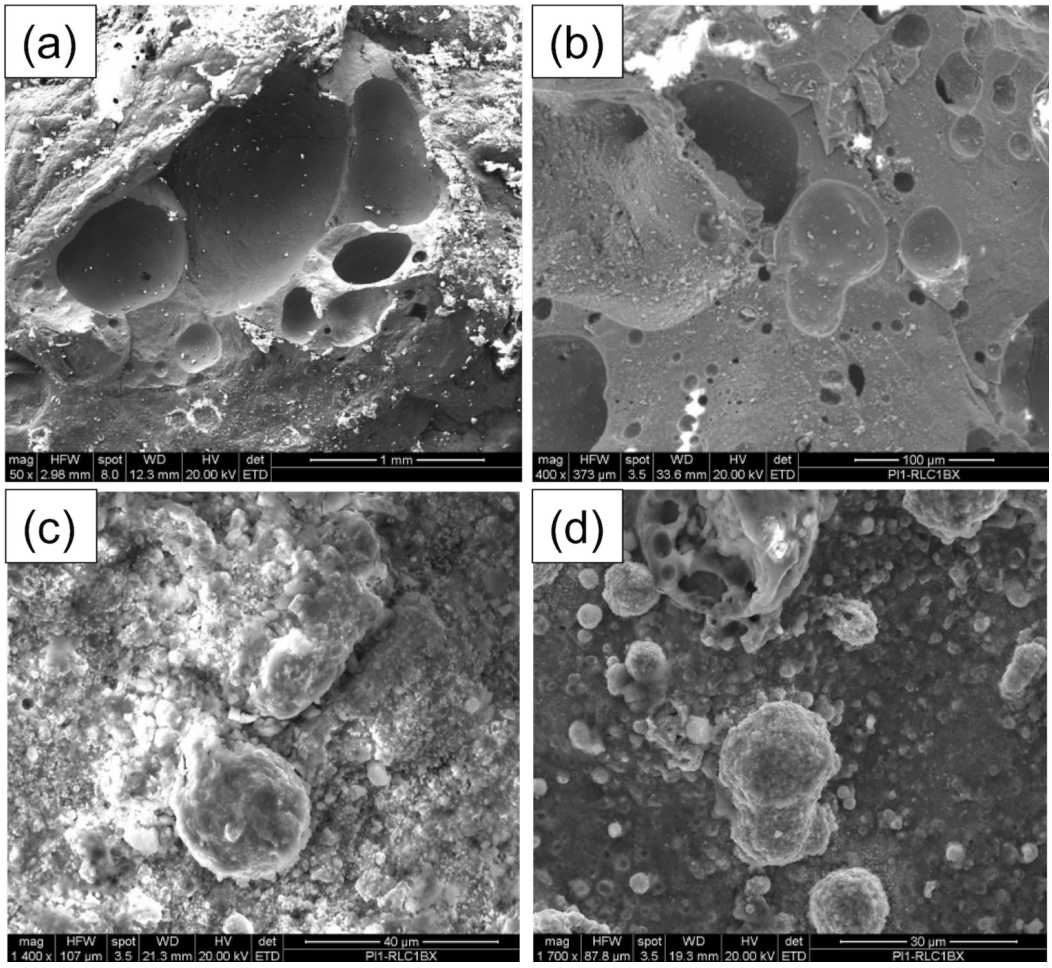

Fig. 3.8. SEM image of reaction front (a)-(b) spherical (c)-(d) globular oxide morphology.

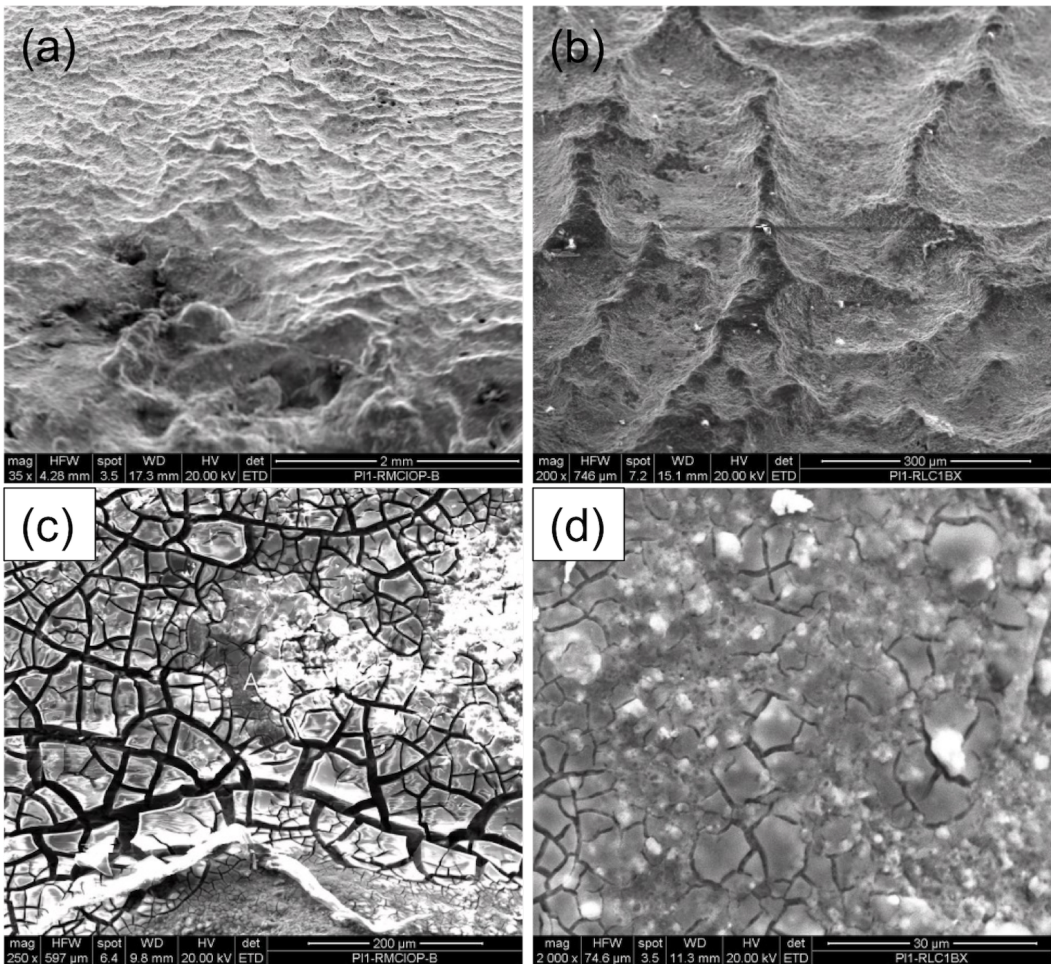

Fig. 3.9. SEM image of reaction front exhibiting varied surface texture: (a)-(b) Surface ridges (c)-(d) mud-cracked texture.

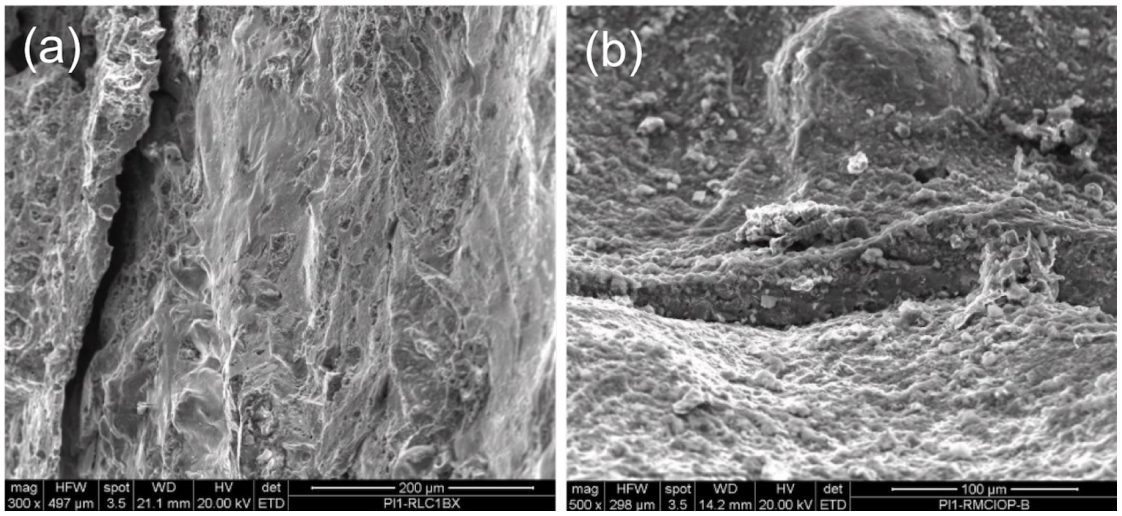

Fig. 3.10. SEM image of reaction front containing (a)-(b) multi-layered scale formation.

Fig. 3.11 contains EDS analysis results corresponding to regions in Q4 and Q3. The results from the heavily degraded Q4 region revealed the presence of elements native to alloys Ti-6Al-4V, IN718, and A-286, but aluminum was detected in high amounts along with a markedly higher amount of oxygen compared to Q3. Other elements not native to the original alloy construction of the roller, (not previously seen in XRF chemical analysis) include sodium, potassium, and chlorine.

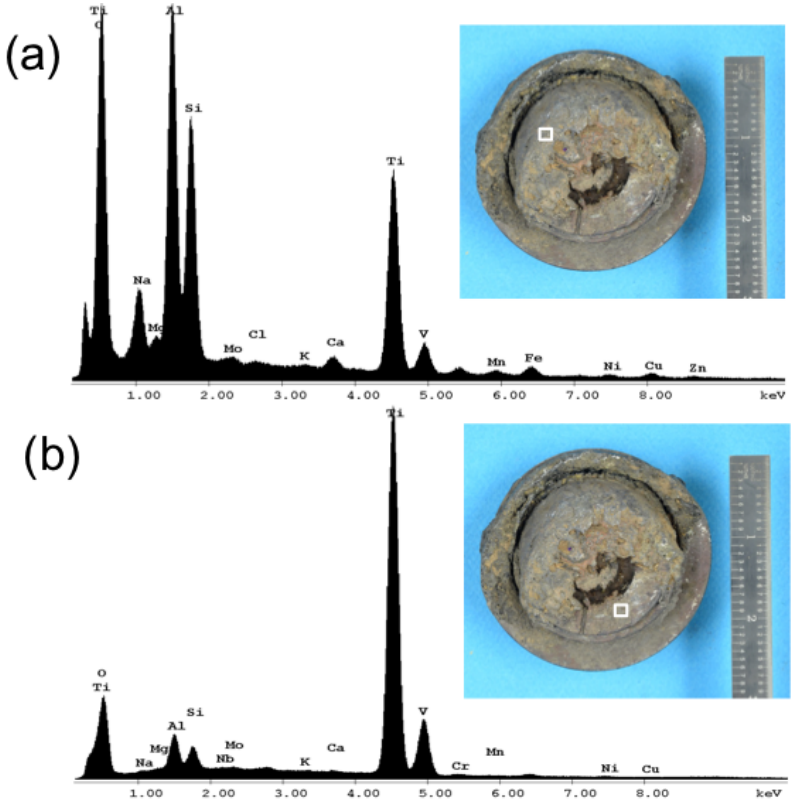

Fig. 3.11. EDS results of the reaction front corresponding to the outlined region in (a) Q1 and (b) Q3.

3.2.2. PLBD Roller Construction

Examination of the cross-section revealed sloped material loss of CrIN718(D), Ti6Al4V(E), and Ti6Al4V(F) that coincided with the observed slope of the reaction front outlined in Fig. 3.7b. It was also observed that by design, the bulk wall thickness of Ti6Al4V(E) and Ti6Al4V(F) varied circumferentially, the greater wall thickness extending along the Q1/Q2 and lesser wall thickness along Q3/Q4, (this feature was also confirmed by the design drawing).

Important design features to note are the surface geometries of the sleeves, as outlined in Fig. 3.12. Ti6Al4V(E) and Ti6Al4V(F) contain an external, circumferential rim that extends outward normal to the outer diameter wall thickness. The rim of Ti6Al4V(F) overlaps a portion of the Ti6Al4V(E) rim, which overlaps the entirety of the reaction plane surface area of CrIN718(D). A similar geometry exists for IN718(C), the rim of which overlaps the reaction plane surface of IN718(B).

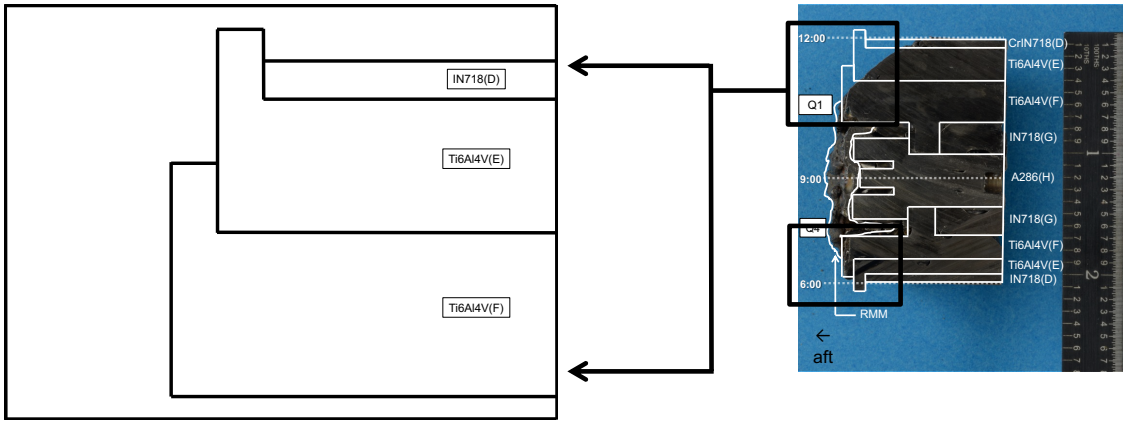

Fig. 3.12. Schematic of external circumferential rim of Ti6Al4V(E) and Ti6Al4V(F). Note overlap of CrIN718(D) by the Ti6Al4V(E) rim.

3.2.3. Re-solidified Molten Material (RSMM)

The RSMM of the reaction front was observed as surface deposition and as part of the bulk sleeve in some regions. Fig. 3.13 provides regions from which micrographs in Fig. 3.14-Fig. 3.19 were obtained. As seen in Fig. 3.14a, the RSMM

deposited onto the outer diameter (OD) of Ti6Al4V(E)-Q1, between CrIN718(D)-Q1 and Ti6Al4V(E)-Q1, contained a dendritic grain structure. The RSMM on Ti6Al4V(E) near Ti6Al4V(F)-Q1 is shown as an extension of the bulk and contained equiaxed grains and voids measuring over 0.1-mm (0.004-in.) in diameter, Fig. 3.14b.

RSMM was predominately observed as surface deposition onto Ti6Al4V(F) and A286(H) in Q1 and Q4. Shrinkage porosity can be seen in Fig. 3.14c and a mixed morphology of globular α with various regions of lamellar α in a β-phase matrix are illustrated in Fig. 3.14b, Fig. 3.15a and Fig. 3.15b. The RSMM of the Q4 region contained spherical voids measuring up to 0.25-mm (0.01-in.) in diameter, Fig. 3.15c, and also exhibited a mixed morphology with lamellar α arranged in irregular-shaped islands, Fig. 3.15c-d. EDS revealed the RSMM to contain titanium, aluminum, vanadium, with iron, molybdenum, chromium, and nickel, as outlined in Fig. 3.16.

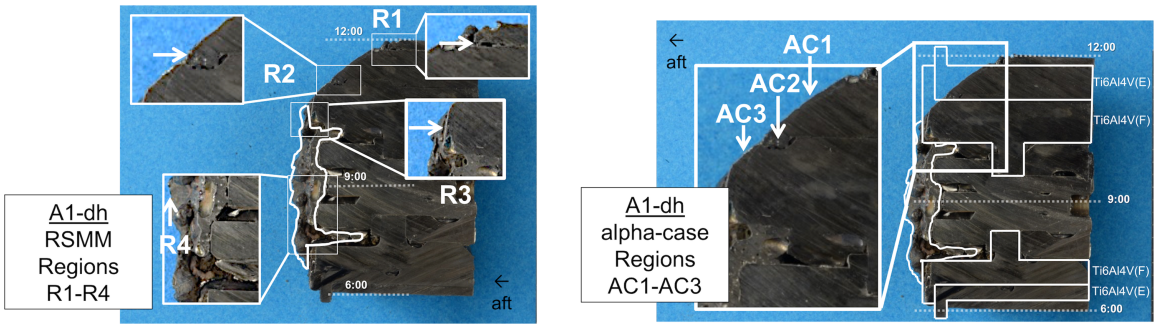

Fig. 3.13. Image of Sample A1-dh with Regions R1-R4 of RSMM and α-case layer Regions AC1-AC3 labeled and outlined in white at the bulk edge surfaces.

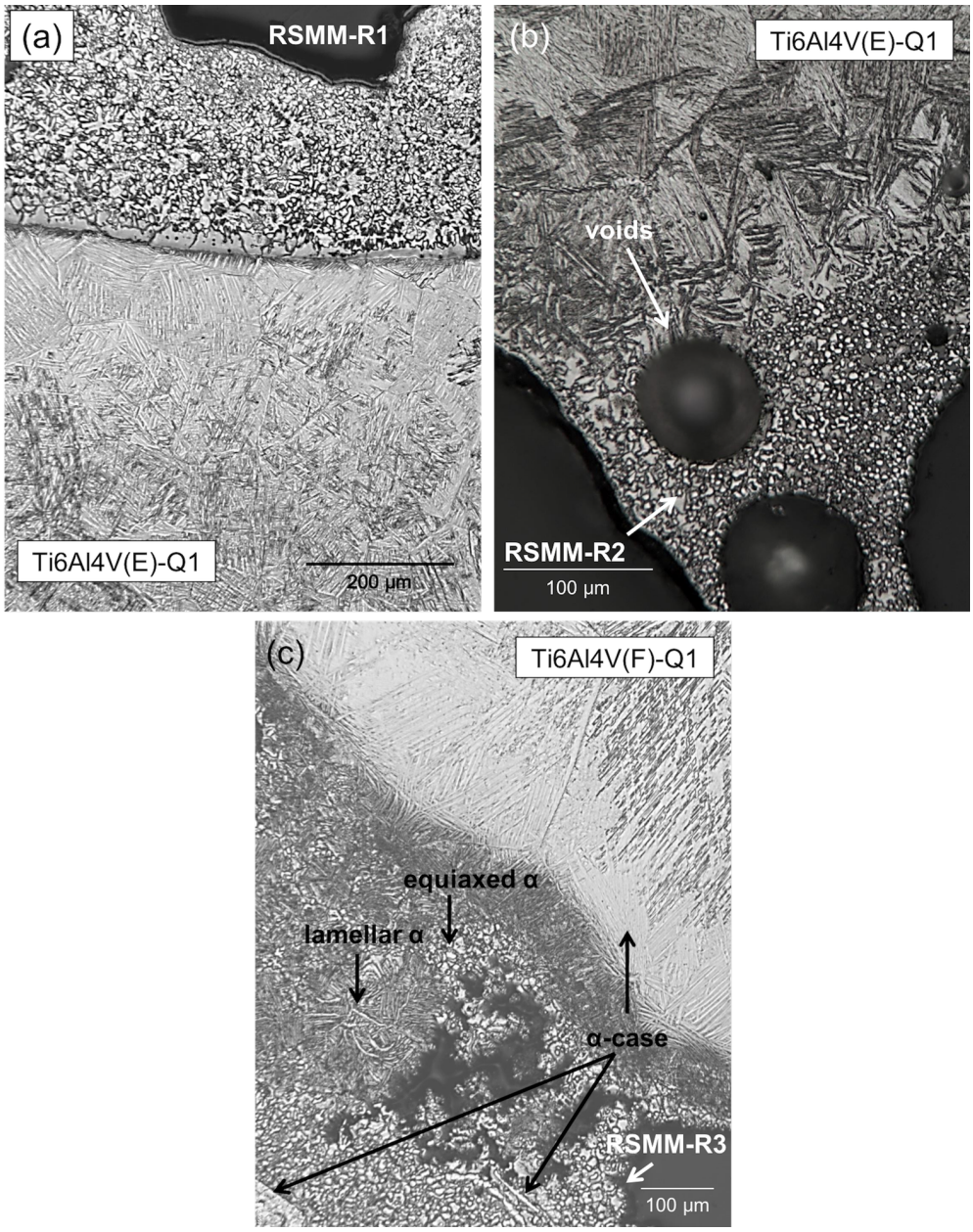

Fig. 3.14. (a) RSMM deposition onto OD of Ti6Al4V(E)-Q1 at CrIN718(D)/Ti6Al4V(E) inner sleeve-spacing, 100X, (b) RSMM of Ti6Al4V(E) at Ti6Al4V(E)/Ti6Al4V(F) inner sleeve-spacing, 200X (c) RSMM deposition/Ti6Al4V(F) interface, 100X; Kroll's.

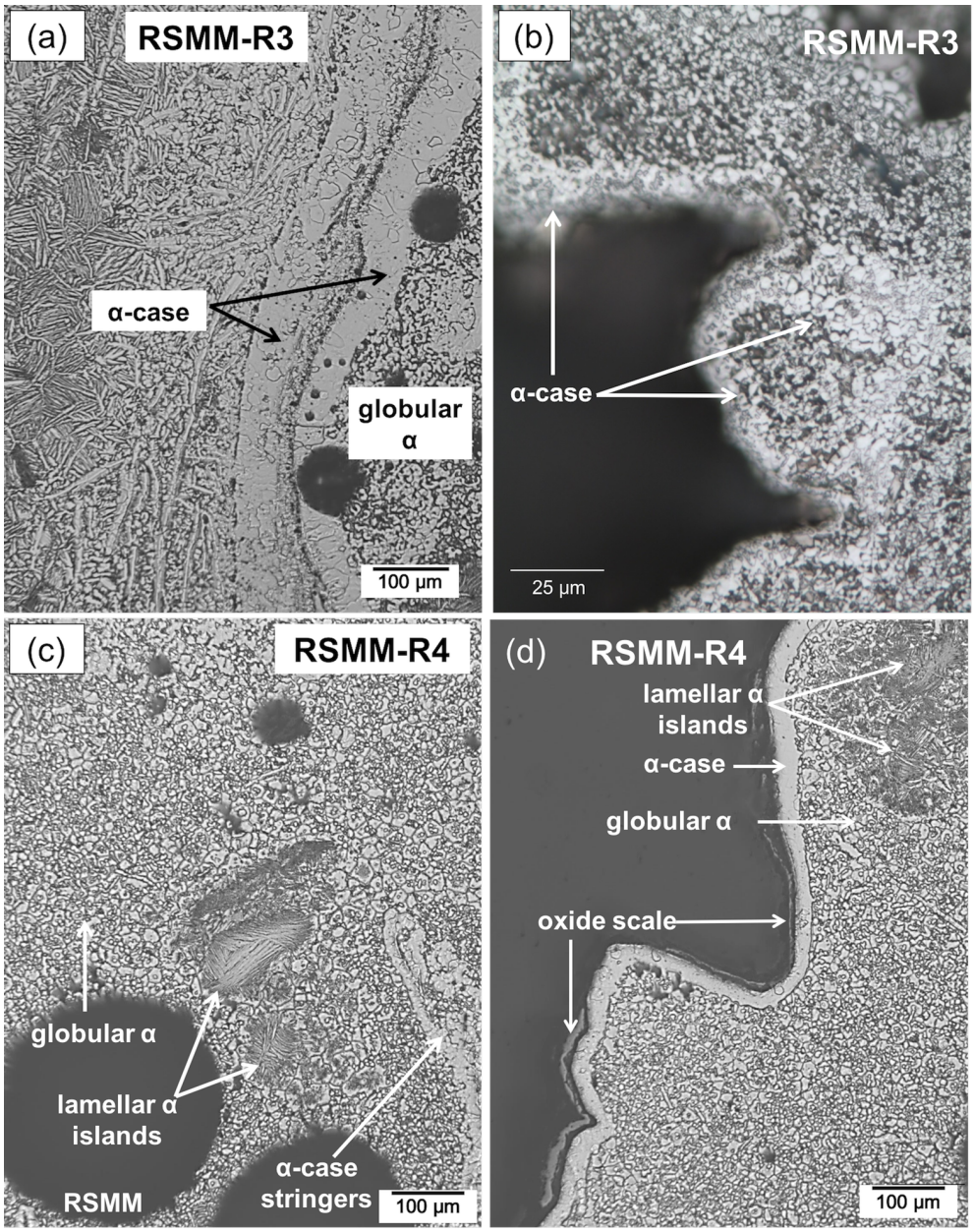

Fig. 3.15. RSMM deposition in Q1 (a) distinct multi-layered α-case, 100X (b) α-case region with variable width and dark regions and RSMM deposition in Q4 with islands of lath α regions containing, 500X (c) α-case stringers, 100X (d) distinct, uniform α-case layer, 100X; Kroll's

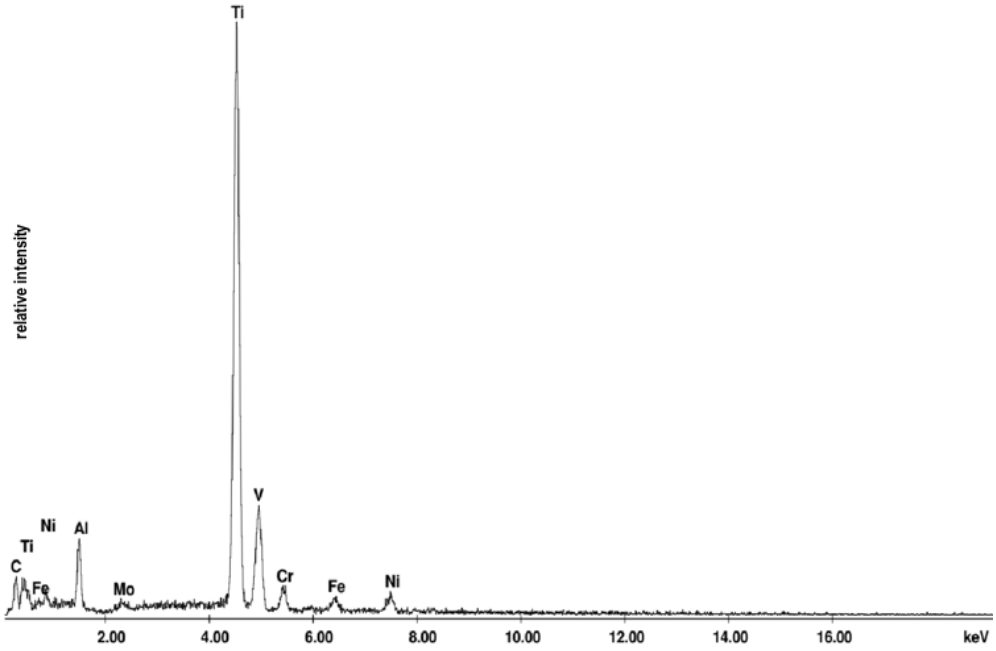

Fig. 3.16. EDS results of RSMM deposition.

3.2.4. Ti-6Al-4V Oxides and α-case Microstructural Analysis

The oxygen-enriched α-case layer was observed throughout the reaction front region within the microstructure of the RSMM and along the bulk surface edges of Ti6Al4V(E) and Ti6Al4V(F). The morphology of α-case was varied throughout and measured from 15- to 25-μm (0.0006- to 0.001-in.) in width. The presence of α-case is understood to form within the bulk of titanium alloys along with and adjacent to the formation of a surface oxide layer. Although the α-case observed in this investigation was not always present with a surface oxide scale

and often exhibited diverse features, it was clearly identified in micrographs as a distinct, light-colored region, which serves as an indication of increased α stabilization.

The bulk surfaces upon which RSMM deposition is present, a light region of coarsened lamellar α is present, visible in Fig. 3.14b and Fig. 3.15a with a multi-layered arrangement of α-case also shown in Fig. 3.15a, the layers measuring approximately 75-μm (0.003-in.) in thickness. Fig. 3.15b illustrates an α-case region of varied thickness, 15- to 25-μm (0.0006- 0.001-in.) in width, containing dark regions of β within the coarsened globular α-case. Small stringers of α-stabilized regions were present within RSMM deposition, presented in Fig. 3.14c, Fig. 3.15a and Fig. 3.15c as irregular-shaped, approximately 10- to 50-μm (0.0004- to 0.002-in.) in width. Fig. 3.15d displays α-case formation with an oxide scale present at the surface of RSMM in Q4. The oxide was discontinuous and measured approximately 15-μm (0.0006-in.) in width. The α-case layer beyond the oxide scale was uniform, 20-μm (0.0008-in.) with a smooth texture and non-descript grains, representing a full stabilization of α-phase.

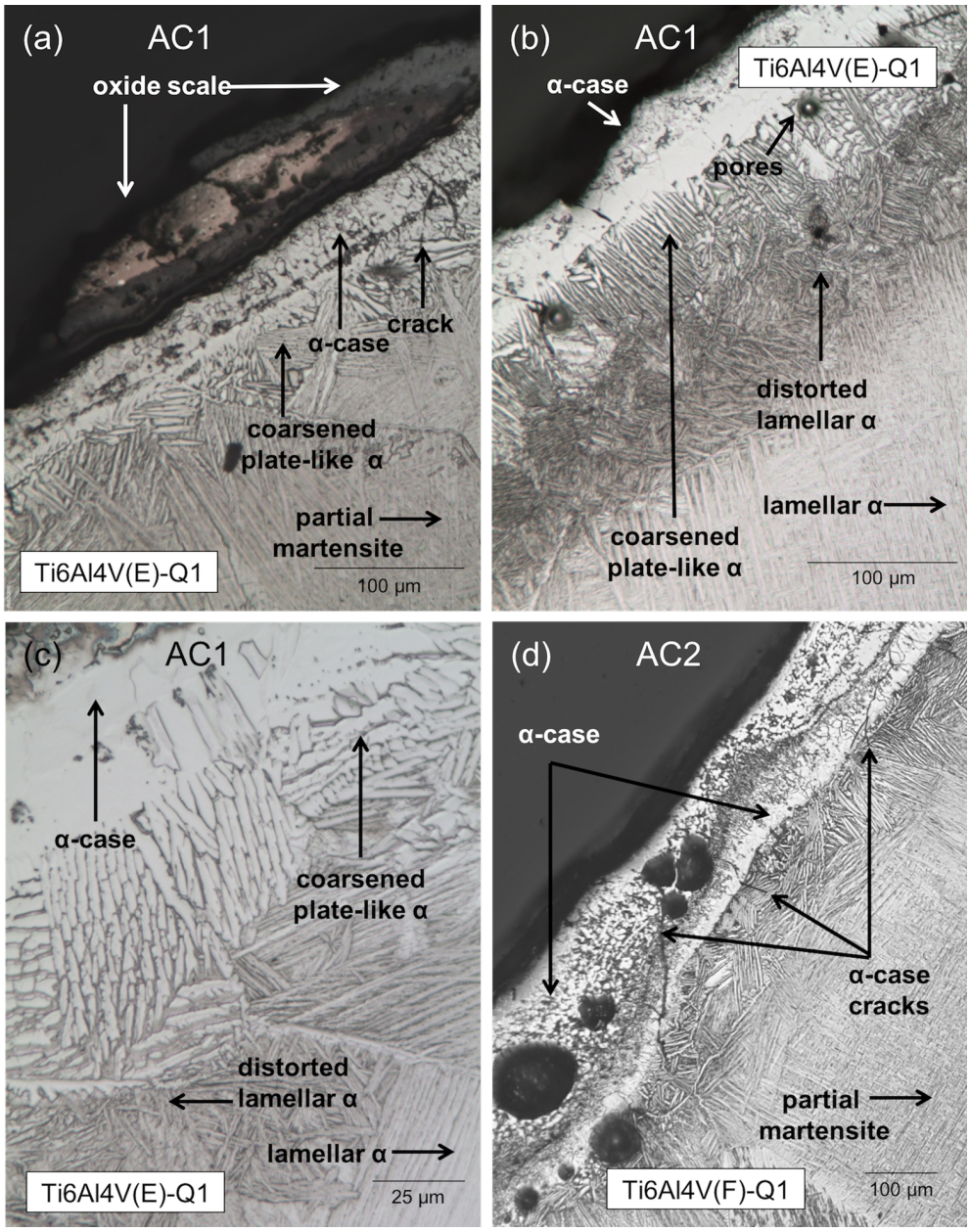

Fig. 3.17. Micrograph of α-case layers observed at the bulk edge surface of Ti6Al4V(E)-Q1 in (a)-(b) AC1, 200X, (c) 500X and (d) Region AC2, 100X; Kroll's.

Fig. 3.17a provides a region of Ti6Al4V(E)-Q1 containing a porous, mound-shaped oxide surface deposit, approximately 1-mm (0.04-in.) in length, 75- and

10-μm (0.003- and 0.0004-in.) in maximum and minimum thickness, respectively. This dark-colored oxide with a light pink center, contained cracking and appeared to be weakly adherent to the surface. The corresponding α-case layer seen adjacent to the oxide deposit appeared as a thin ~1-μm (0.00004-in.) linear region that was well-defined and etched dark, indicating the β phase. This linear feature served to delineate two morphologies of the α-case layer: adjacent to the oxide, the α-case was of a globular morphology, measuring approximately 40-μm (0.002-in.) in uniform thickness, and a morphology defined as featureless, containing solid α phase, extended 15-μm (0.0006-in.) into the bulk. A sharp transition was observed beyond the α-case layer where coarse, plate-like α phase, coherent with the innermost α-case layer, extended into the bulk approximately 75-μm (0.003-in.), at which point a partial martensitic structure was apparent, defined by both fine acicular α' and retained prior α lamellae, in prior β grains.

In a region where no surface oxide was resolved on Ti6Al4V(E)-Q1, globular α with grain boundary β characterized the α-case, measuring 15- to 30-μm (0.0006- to 0.001-in.) in depth, adjacent to the jagged, rough surface. The α-case then transitioned into a uniform, featureless layer of solid white α, measuring 30-μm (0.001-in.) depth, in result of having a full-α structure, Fig. 3.17b-c. A distinct transitional region beyond the α-case consisted of coarse, unidirectional finger-like protrusions of α phase that extended away from the α-case layer and measured approximately 50-μm (0.002-in.) in depth. Voids appeared localized to this region of transition. Moving into the bulk, a second transition was observed,

where less coarse, plate-like α was present in a dark-colored woven arrangement of measuring 50- to 60-μm (0.002- to 0.002-in.) in depth beyond which the plate-like α was present.

Ti6Al4V(F)-Q1 contained regions of multi-layered α-case formation, Fig. 3.17d, separated by a dark layer of fine, globular grains. With no adjacent surface oxide present, the outermost α-case was characterized by globular α (light) and β phase (dark) apparent at the grain boundaries. The inner α-case layer was more homogenous, containing less β phase. Pores and cracks were prevalent throughout both α-case layers and the transitional region of coarse plate-like α. Extending away from the α-case layer into the bulk approximately 150-μm (0.006-in.) in depth a transition into a partial martensitic structure was observed.

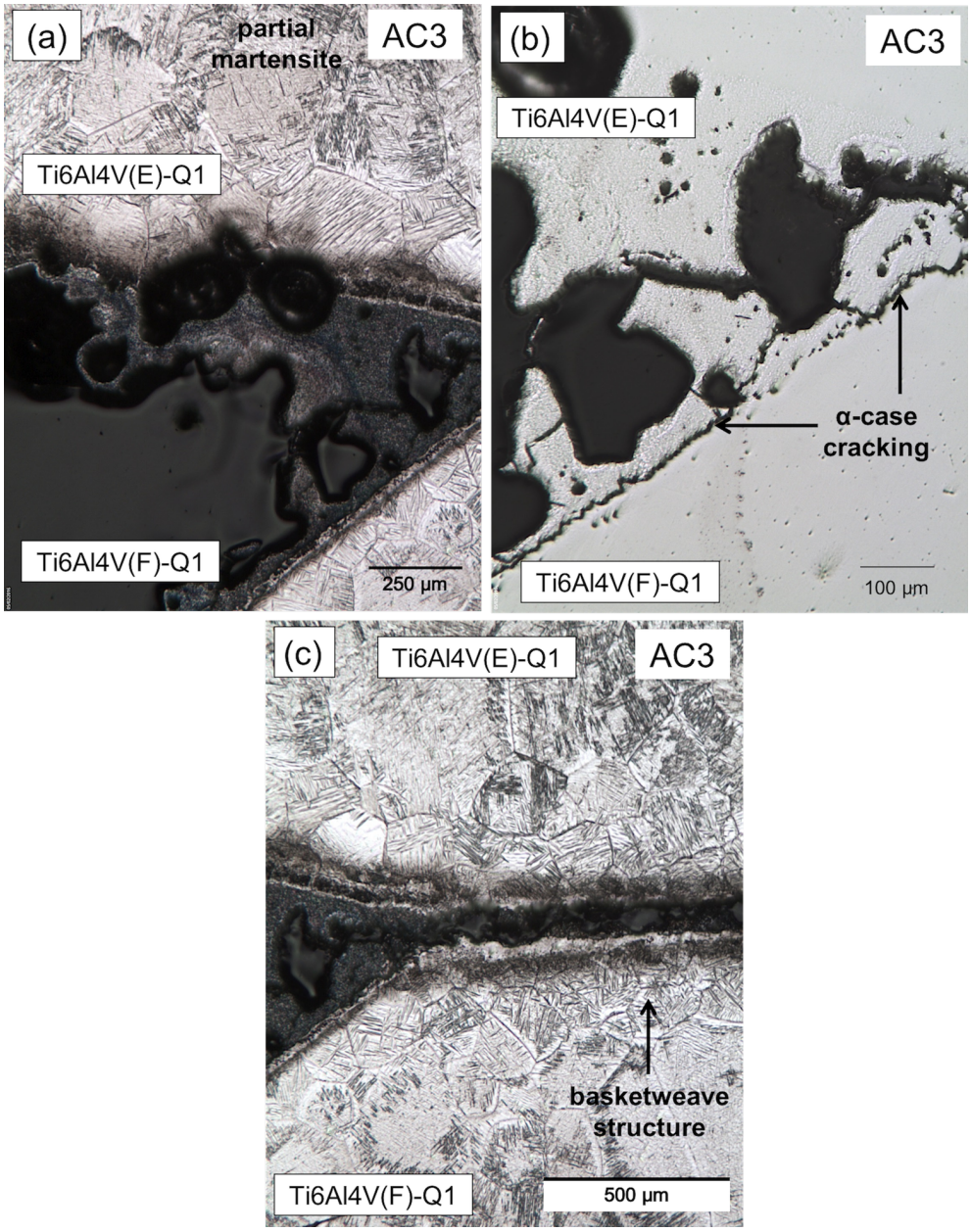

Fig. 3.18. Micrograph of porous, deposition (dark) on inner sleeve OD surfaces of Ti6Al4V(E)-Q1 and Ti6Al4V(F)-Q1 in (a) notch region, 150X (b) As-polished micrograph of (a), 150X; (c) inner-sleeve spacing approximately 1-mm (0.04-in.) beyond notch region, 100X; Kroll's.

On OD surfaces at the reaction front (normal to the reaction plane) of Ti6Al4V(E) and Ti6Al4V(F) in Q1, where inner-sleeve spacing is increased due to a machined notch of the Ti6Al4V(F) sleeve, deposition that appeared sintered and oxidized, was observed, Fig. 3.18b. As seen in the as-polished micrograph in Fig. 3.18b, the oxide exhibited a shiny, rough texture. The micrograph of Fig. 3.18c shows deposition on OD surfaces, approximately 1.0-mm (0.04-in.) beyond notch region. The pores within the deposition on Ti6Al4V(E)-Q1 measured 5- to 250-μm (0.0002- to 0.01-in.) in diameter, with coalesced voids seen partially within the bulk. The pores on Ti6Al4V(F)-Q1 were seen only within the deposition and measured smaller at 5- to 25-μm (0.002- to 0.001-in.) in diameter.

The α-case on the inner-sleeve OD surfaces of Ti6Al4V(E)-Q1 and Ti6Al4V(F)-Q1 measured approximately 30-μm and 60-μm (0.001 and 0.002 in.) in depth, respectively. In areas where voids were present within the bulk, a distinct α-case layer was not observed. A linear region of dark discoloration, approximately 15-μm (0.0006-in.) in thickness, was observed within the α-case layers in the notch region which, as seen in the as-polished micrograph of Fig. 3.18b, contained coalesced voids that compromised adherence of the deposition to the Ti6Al4V(F) surface. In contrast, no voids or crack-like features were evident corresponding to the dark delineated region in the α-case layer of the Ti6Al4V(E)-Q1 OD surface.

Moving into the bulk of Ti6Al4V(E)-Q1, away from the deposition as shown in Fig. 3.18c, a transitional region, also of dark discoloration, was observed, with

variable thickness measuring approximately 50- to 100-μm (0.002- to 0.004-in.) in depth. A gradient in discoloration existed at the transition region, as the extent of the dark shade decreased moving into the bulk, where the microstructure consisted of a basketweave structure then further into the bulk, partial martensite was present. The same gradient was observed for the inner-sleeve OD surface of Ti6Al4V(F)-Q1 as the region of discoloration, with a more distinct uniformity, extended approximately 50-μm (0.002-in.) into the bulk of Ti6Al4V(F)-Q1, after which, small grains of basketweave structure also transitioned into coarse-grained partial martensite.

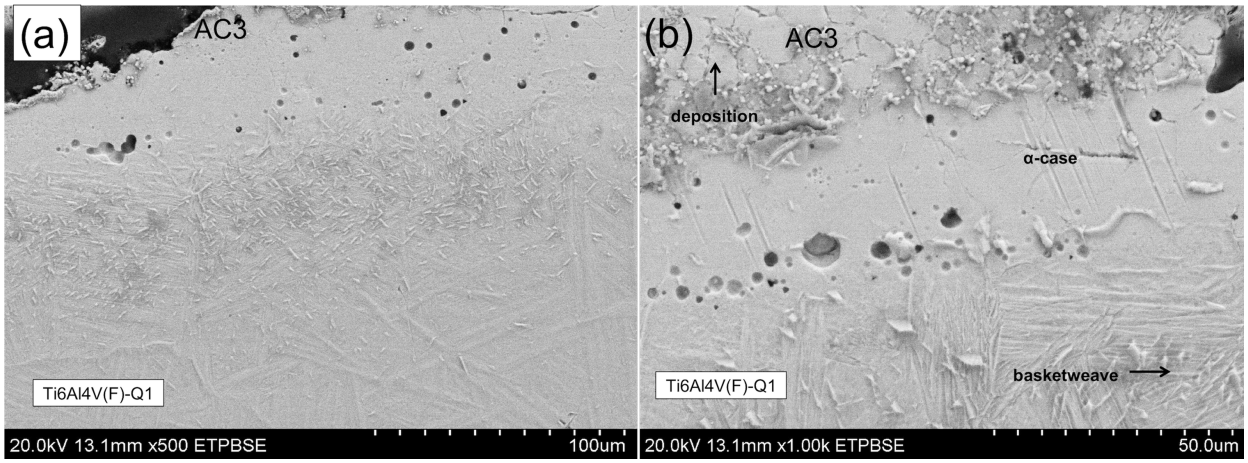

Fig. 3.19. (a)-(b) BSE micrograph of inner-sleeve OD edge surface of Ti6Al4V(F)-Q1 at (a) inner-sleeve spacing approximately 1-mm (0.04-in.) beyond notch region.

Fig. 3.19a-b displays BSE images that clearly illustrate the morphological distinction of the deposition, α-case layer, and microstructural transition into the

bulk. The equiaxed grains contained small, globular deposits arranged along grain boundaries. The α-case region contrasted greatly with the other areas in the image, exhibiting a smooth and porous texture. The pores of the α-case layer, measuring 1.0- to 8.0-μm (0.00004- to 0.0003-in.) in diameter, appeared to have a preferential arrangement near the interface between the α-case layer and transitional bulk region where the lamellar features of the Widmanstätten structure are present with a layer of short flecks of flake-like α that measured approximately 75-μm (0.003-in) in thickness.

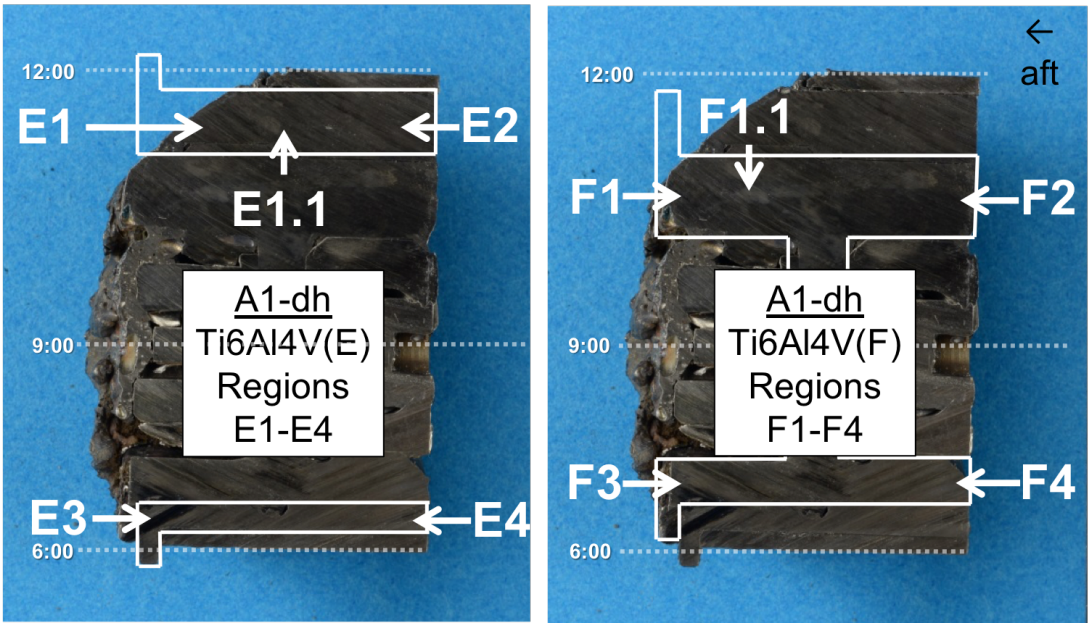

Fig. 3.20. Image of Sample A1-dh with Regions E1-E4 of Ti6Al4V(E) and F1-F4 of Ti6Al4V(F) labeled and outlined in white.

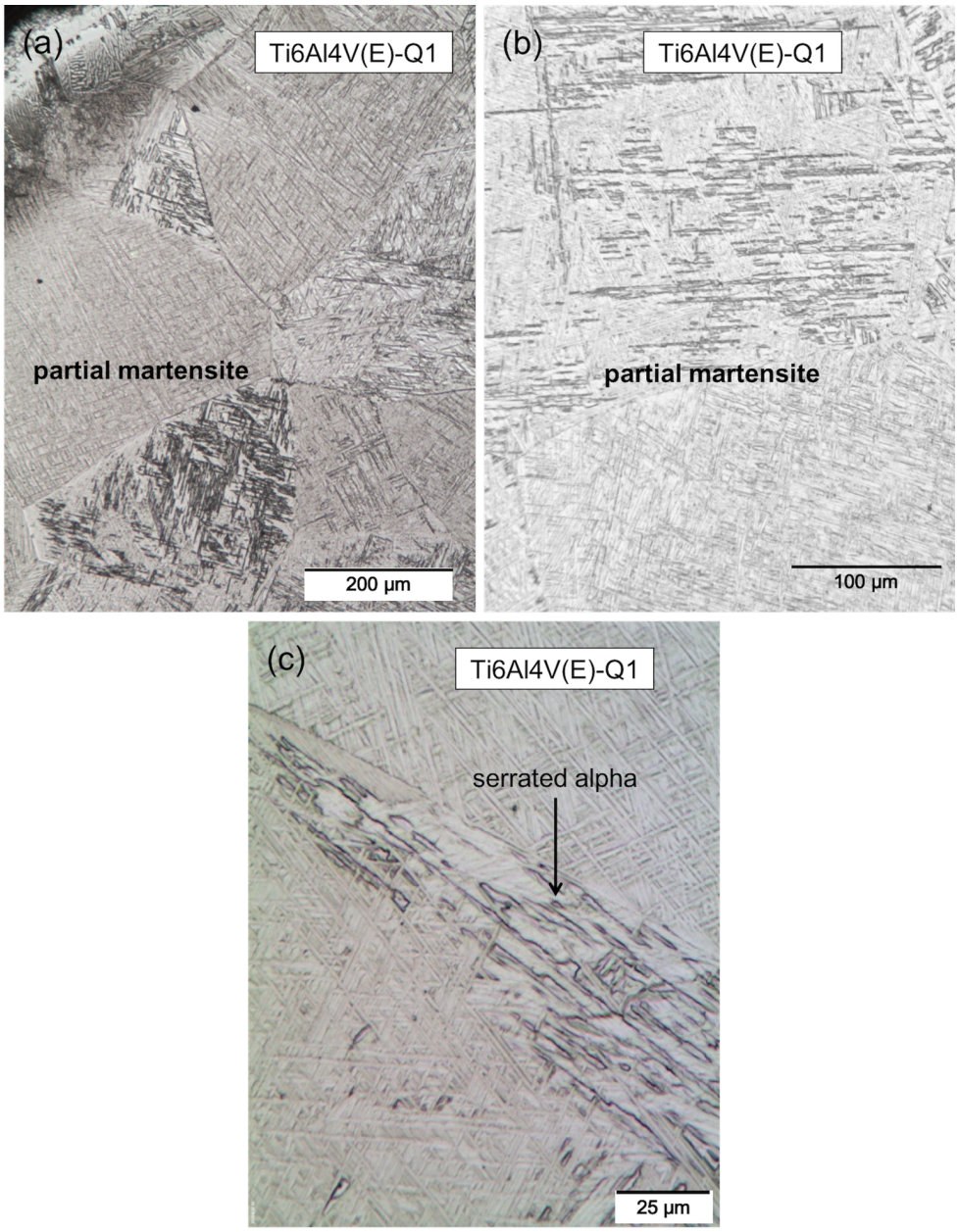

Fig. 3.21. Micrograph of Ti6Al4V(E)-Q1 in E1 region of bulk; (a) 100X, (b) 200X, (c) 500X; Kroll's.

3.2.5. Ti-6Al-4V Sleeves Bulk Microstructural Analysis

Fig. 3.20 provides regions from which micrographs in Fig. 3.21-

Fig. 3.25 were obtained. The partial martensitic bulk microstructure observed beyond α-case layers for Ti6Al4V(E)-Q1 and Ti6Al4V(F)-Q1, Fig. 3.21a-b, contained serrated α, resolved at higher magnification (Fig. 3.21c). The martensitic structure gradually transitioned into a structure of acicular α in an aged transformed β matrix and at approximately 7.6-cm (0.3-in.) away from the reaction interface, Ti6Al4V(E) transformed into (Fig. 3.22a), and remained as, a bimodal structure of elongated primary α grains in a transformed β matrix consisting of coarse, plate-like α and β, Fig. 3.22b-c. A bimodal microstructure is typically yielded from solution heat treating to 845-930 ˚C (1550-1700 ˚F) and subsequent aging below the β transus.

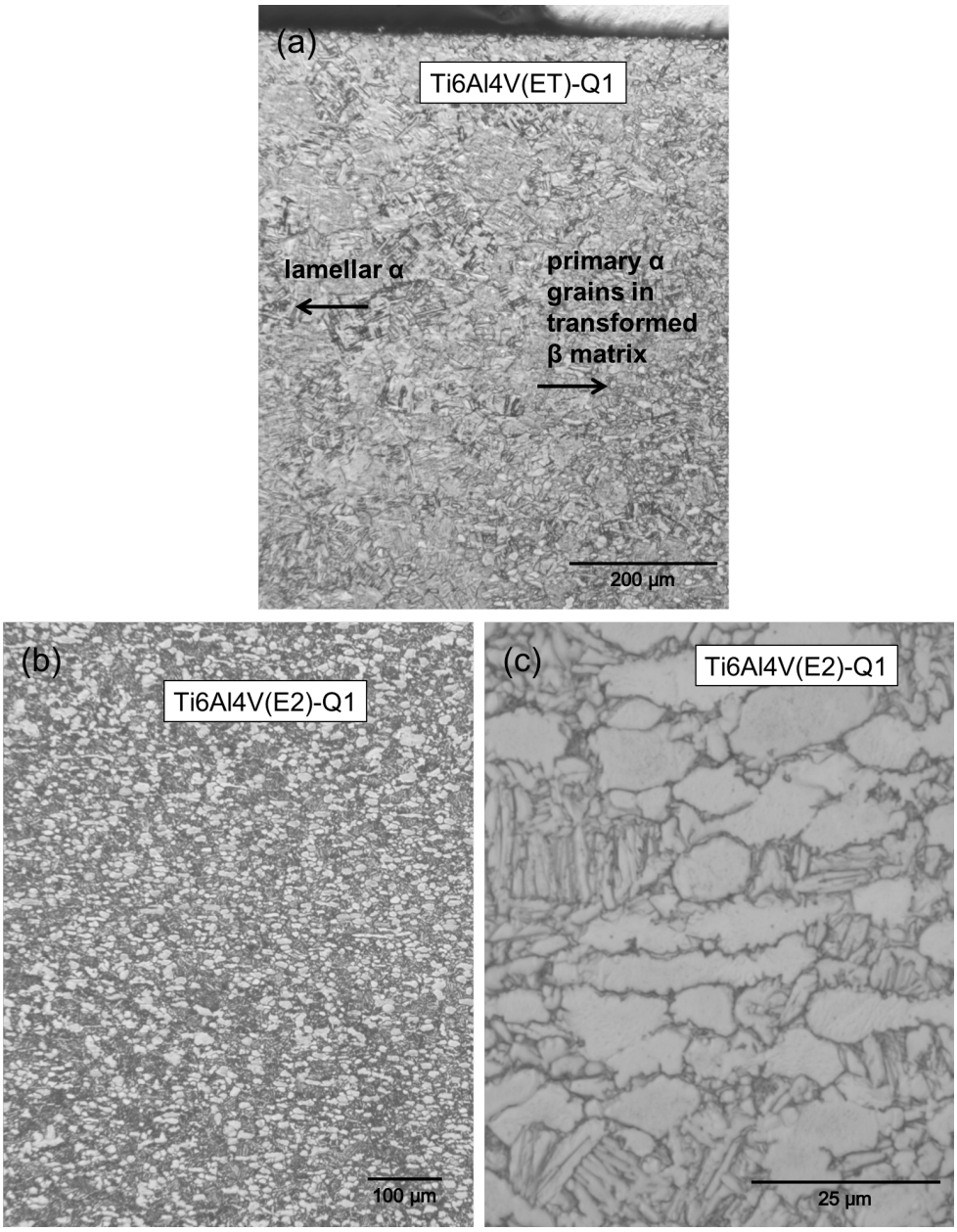

Fig. 3.22. Micrograph of Ti6Al4V(F)-Q1 in (a) F1.1 region of bulk where microstructural gradient is apparent (approximately 1.5-cm (0.6-in.) from the reaction front edge, 100X; (b) E2 region of bulk approximately 3.3 (1.3-in.) away from reaction front, 100X, and (c) 100X (measurements obtained from the edge surface of Ti6Al4V(F)-Q1); Kroll's.

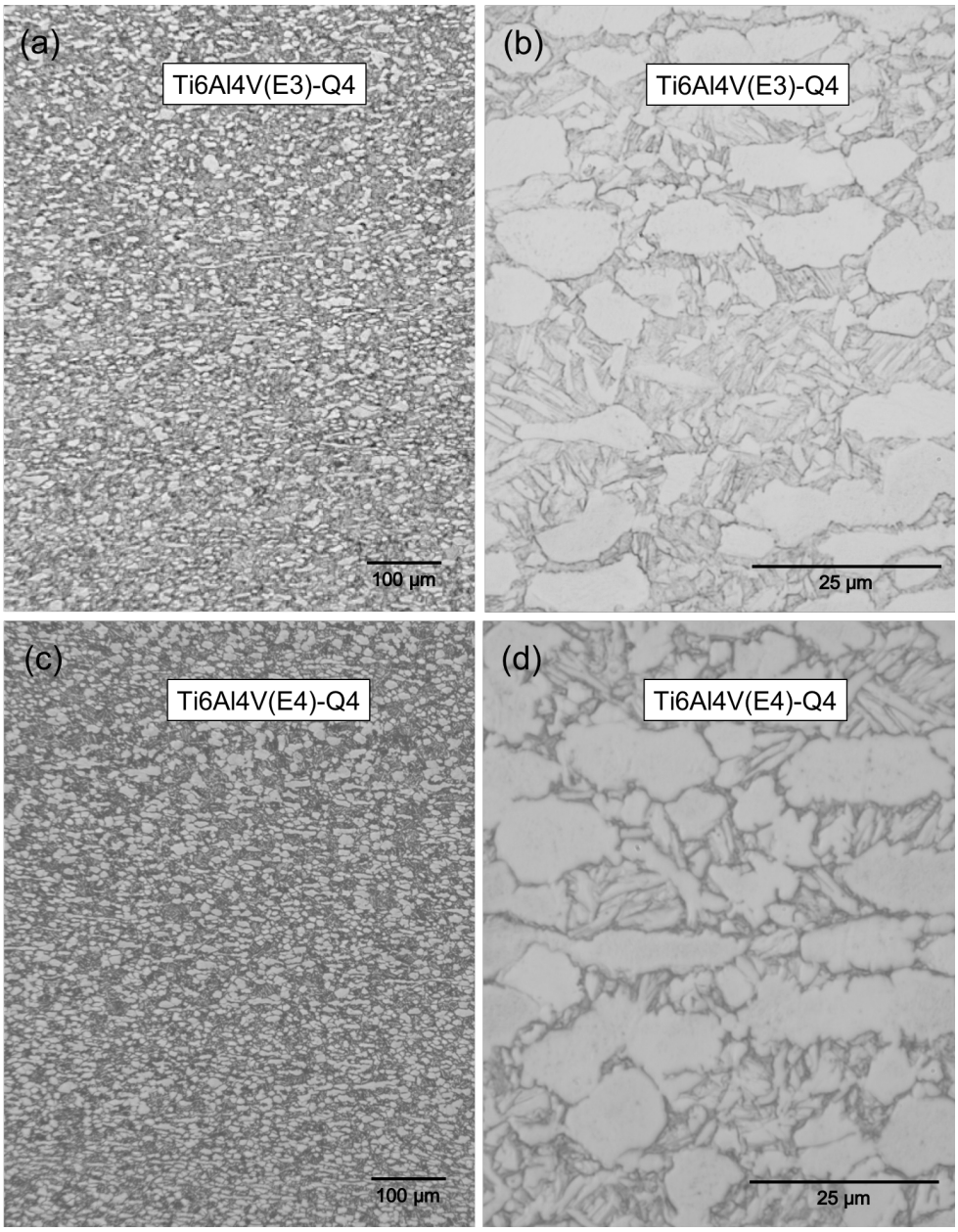

Fig. 3.23. Micrograph of Ti6Al4V(E)-Q4 in (a) E3 region of bulk at the reaction front edge, 100X and (b) 1000X; (c) E4 region of bulk approximately 3.3 cm (1.3-in.) away from reaction front, 100X and (d) 1000X; Kroll's.

As seen in Fig. 3.23, Ti6Al4V(E)-Q4 contained a bimodal microstructure comparable to that of Ti6Al4V(E)-Q1. The volume fraction of primary α is higher for Ti6Al4V(E)-Q4 than for Ti6Al4V(e)-Q1 and the volume fraction of primary α decreases slightly in Ti6Al4V(E)-Q4 moving away from the surface of the roller which is typically attributed to decreased aging temperature or aging time.

Presented in Fig. 3.24, the acicular α structure of Ti6Al4V(F) transitioned into, and remained as, a structure containing basket-weave acicular α (Widmanstätten) with prior β grain boundaries, the dark basketweave typical of an overaged β annealed 980 ˚C (1800 ˚F) structure. [63]

Similar to Q1, Fig. 3.25a-b shows the microstructure of Ti6Al4V(F)-Q4 to be partially martensitic near the surface and a gradient was also present in Ti6Al4V(F)-Q4 as the transition to large colonies of Widmanstätten α was observed and maintained for the remaining bulk moving away from the reaction front, Fig. 3.25c-d. Ti6Al4V(F) was absent of the bimodal structure observed within Ti6Al4V(E). Microhardness testing performed on Ti6Al4V(E) and Ti6Al4V(F) are summarized in Fig. 3.28. Elevated hardness values were observed nearest to the reaction front for both Ti6Al4V(E) and Ti6Al4V(F) the remainder of the bulk, moving away from the reaction front measured consistently around 300-350 HV.

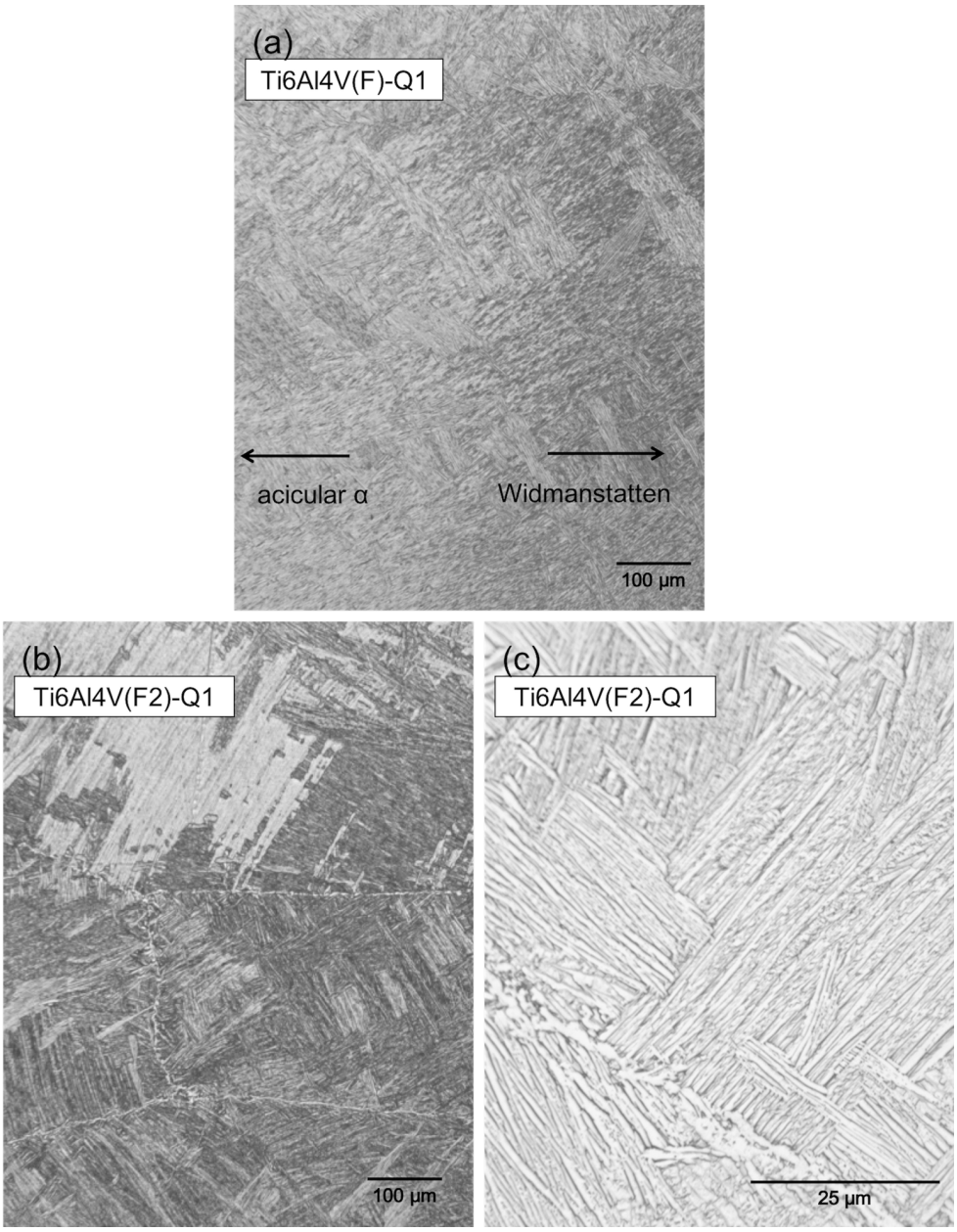

Fig. 3.24. Micrograph of Ti6Al4V(F)-Q1 in (a) F1.1 region of bulk where microstructural gradient is apparent (approximately 0.76-cm (0.3-in). from the reaction front) 100X and in (b) F2 region of bulk approximately 3.3-cm (1.3-in.) away from reaction front, 100X and (c) 1000X; Kroll's.

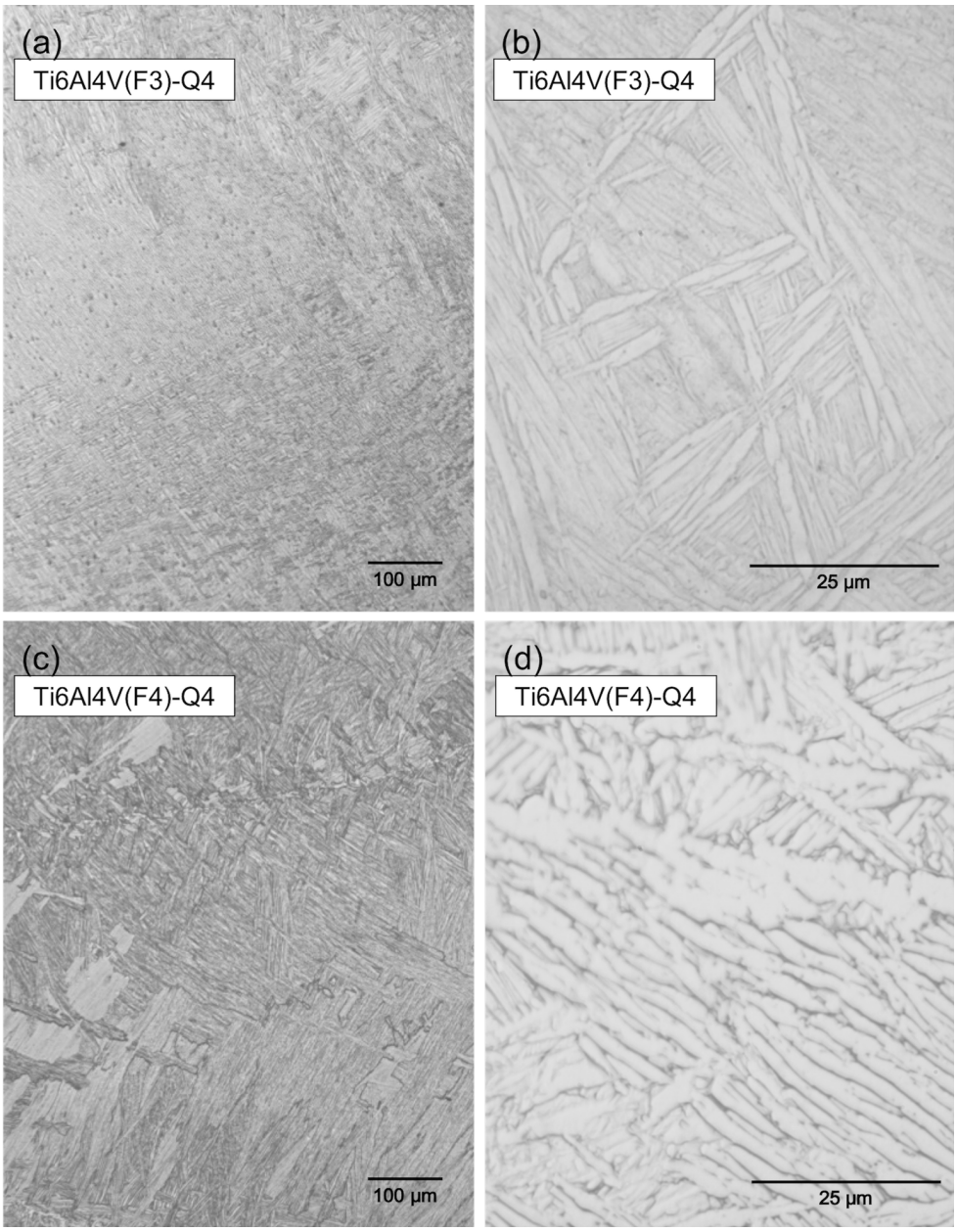

Fig. 3.25. Micrograph of Ti6Al4V(F)-Q4 in (a) F3 region of bulk at the reaction front edge surface, 100X and (b) 1000X; (c) F4 region of bulk approximately 3.3-cm (1.3-in.) away from reaction front, 100X and (d) 1000X; Kroll's.

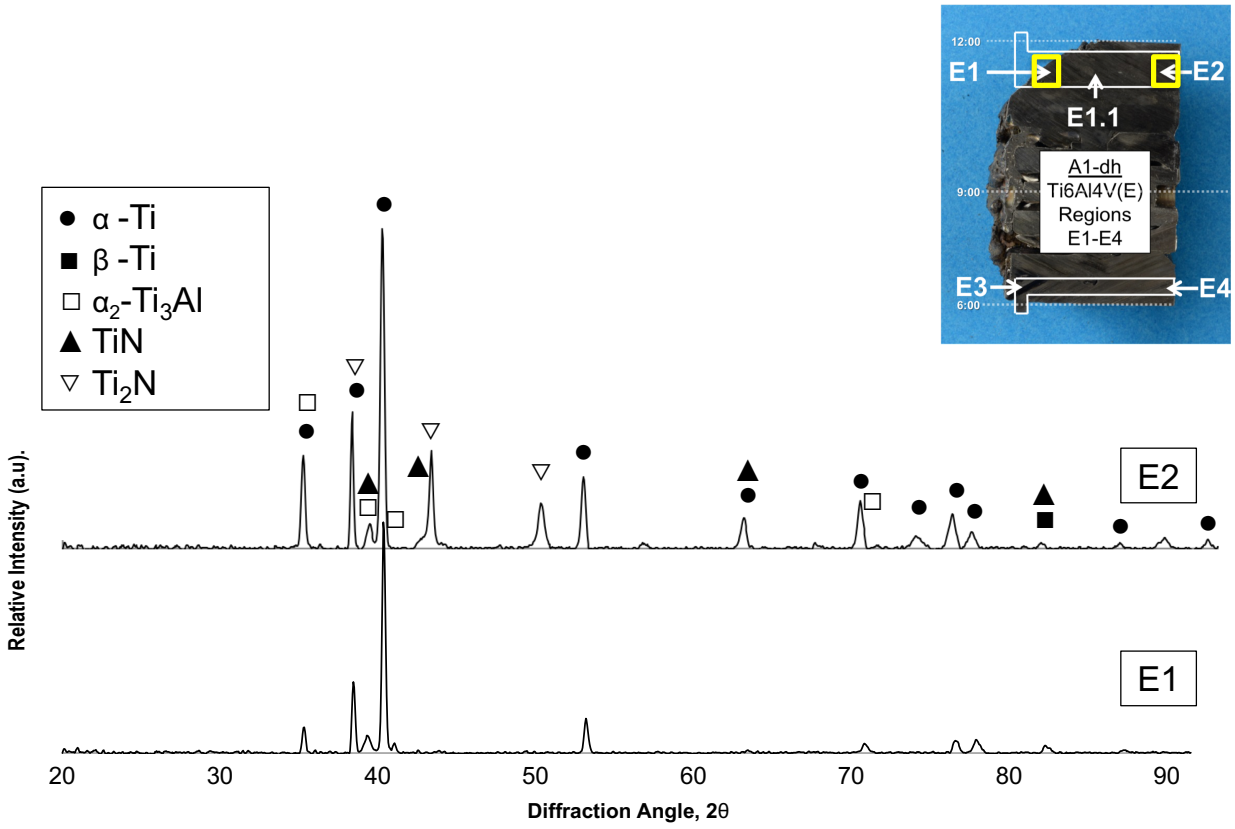

Fig. 3.26. Diffraction patterns of Ti6Al4V(E) in Q1 region at Regions E1 and E2 as outlined in the provided schematic.

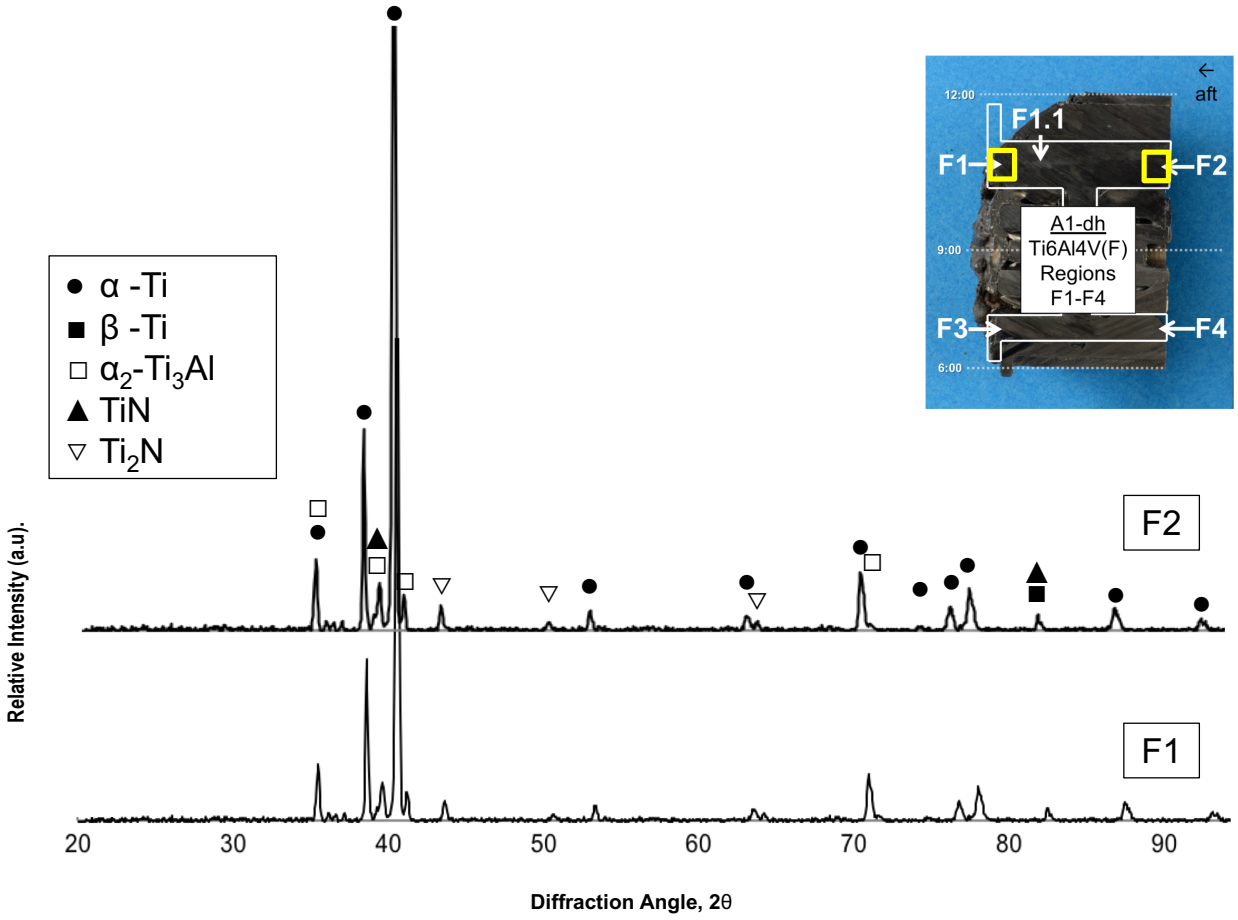

Fig. 3.27. Diffraction patterns of Ti6Al4V(F) in Q1 at Regions F1 and F2 as outlined in the provided schematic.

The results, shown in Fig. 3.26-Fig. 3.27, reveal peaks corresponding to α-Ti and β-Ti, along with peaks that correspond to α_2 and TiN. For the Ti6Al4V(E) sleeve, the α_2 peak decreased moving away from the reaction front while the TiN phase increased. For Ti6Al4V(F) the intensities of the α_2 and TiN showed little

variation throughout the bulk, both remaining at similar relative intensities at throughout the bulk.

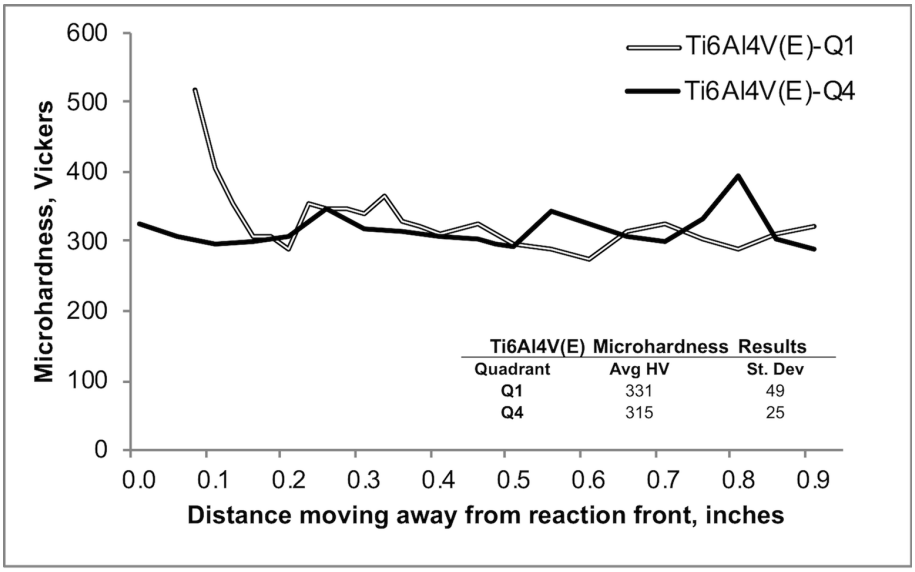

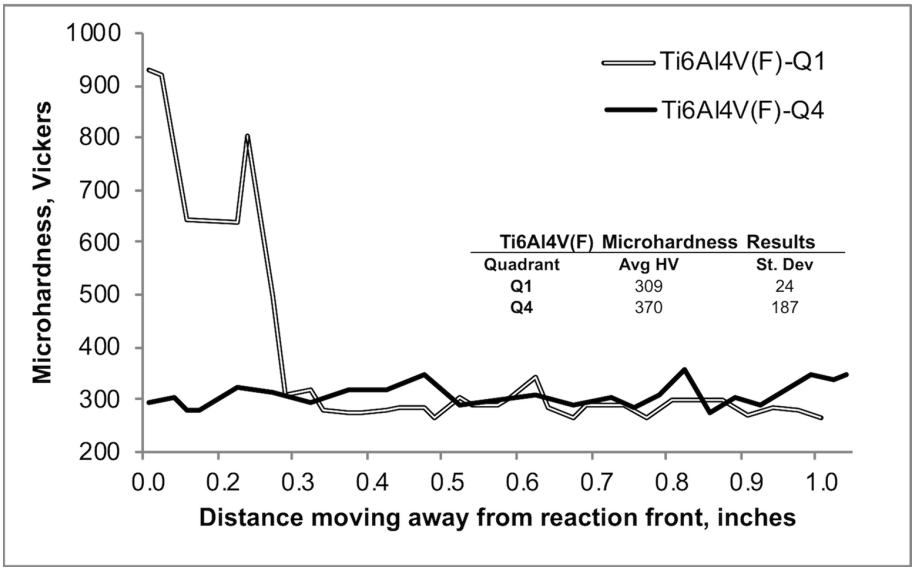

Fig. 3.28. Microhardness results for Ti6Al4V(E) and Ti6Al4V(F) in both Q1 and Q4. Measurements taken along axial length moving away from the reaction front edge.

3.2.6. A286 Microstructural Analysis

Fig. 3.29 provides regions from which micrographs in Fig. 3.30-Fig. 3.31 were obtained.

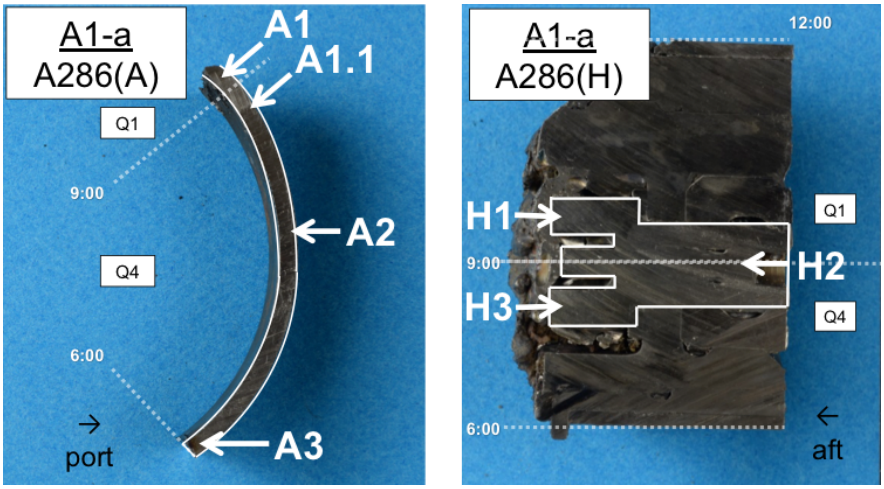

Fig. 3.29. Image of Sample A1-dh with Regions A1-A3 of A286(A) and H1-H3 of A286(H) labeled and outlined in white.

3.2.6.1. A286(A)

The microstructure of A286(A), provided in Fig. 3.30a-e, contained a solid solution austenite matrix with fine γ' precipitation at the interface of material loss, as shown by the darkened regions in the micrographs. At the edge surface, a dendritic microstructure was observed and transitioned into equiaxed, partially dendritic grains. Segregation at the grain boundaries was also present, as Fig. 3.30b-e displays heavy intergranular precipitation and precipitate free zones

(PFZ) were prevalent, surrounding needle-like particles likely to be the δ phase Fig. 3.30b. The region at material loss is typical of partially melted and overaged A286. Moving away from the fracture surface, the microstructure was characterized by a decrease in matrix precipitation and an increased in coarsened particles, likely MC-type carbides. Decreased grain boundary precipitation exhibited even distribution and needle-like particles were absent, representing a structure produced by furnace cooling from a solution 980-1230 ˚C (1800-2250 ˚F).

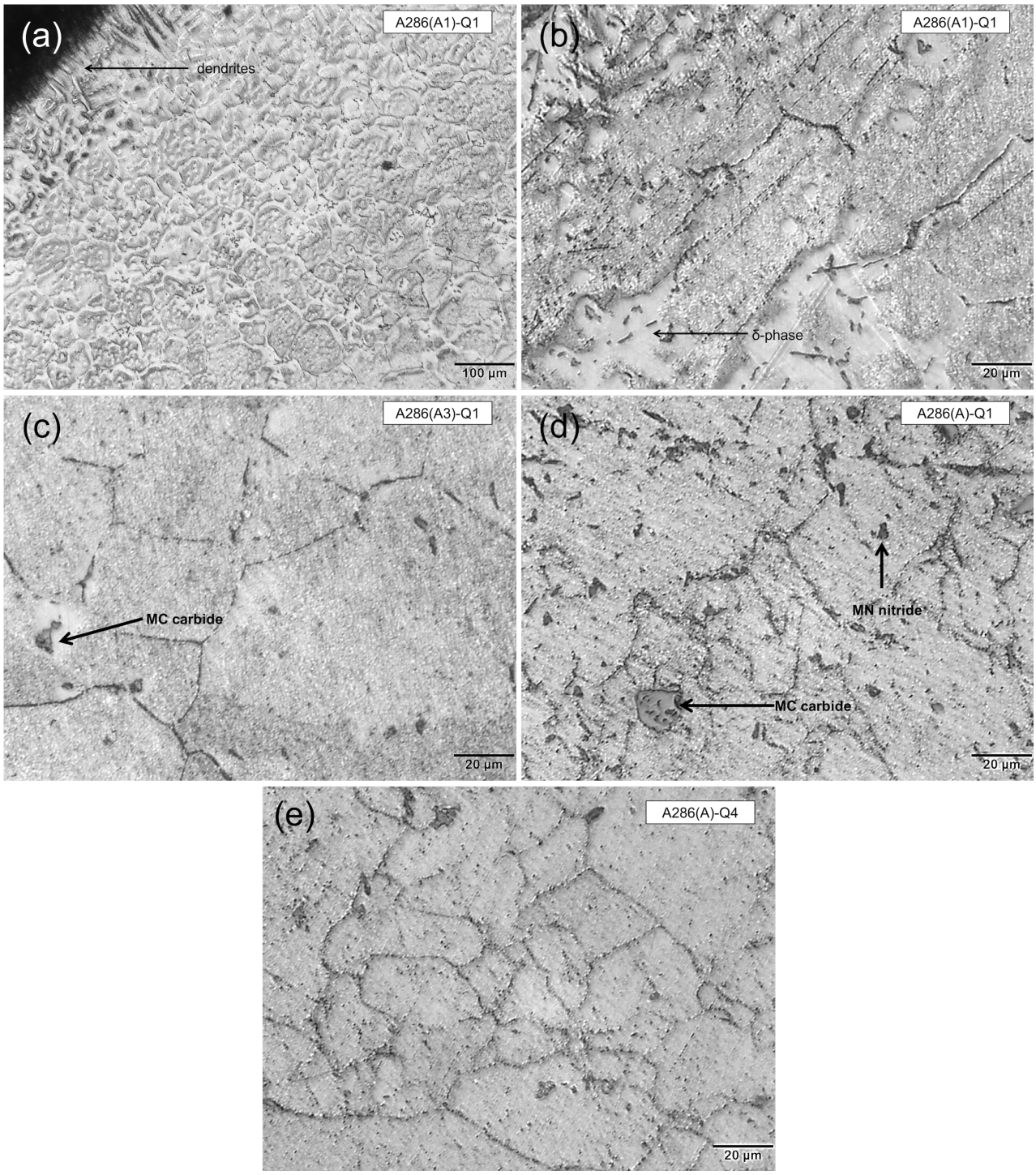

Fig. 3.30. Micrograph of A286(A)-Q1 in the (a)-(b) A1 region of bulk at the reaction front edge surface and in the (c) A2 region and A3 region of Q4.

3.2.6.2. A286(H)

At the reaction front, the microstructure of A286(H)-Q1 and A286(H)-Q4 displayed in Fig. 3.31 contained a solid solution of austenite grains, approximately 5- to 30-μm (0.0002- to 0.001-in.) with finely dispersed globular carbides, typical of M6C-type carbides, throughout the matrix and fine, coalesced carbides (typical of $M_{23}C_6$-type) along the grain boundaries. Both structures are typical of overaging, with the A286(H)-Q1 region contrasting with Q4, as this region experienced markedly increased matrix and grain boundary precipitation, shown in, Fig. 3.31b. Away from the reaction front, approx., 3.3-cm (1.3-in.) into the bulk, annealing twins were observed, as well as darkened regions due to the presence of unresolved γ' precipitates. Fig. 3.31c also shows smaller grains as well as decreased carbide precipitation within the grains and at grain boundaries. The Laves phase was present within the matrix along with coarse, irregular carbides.

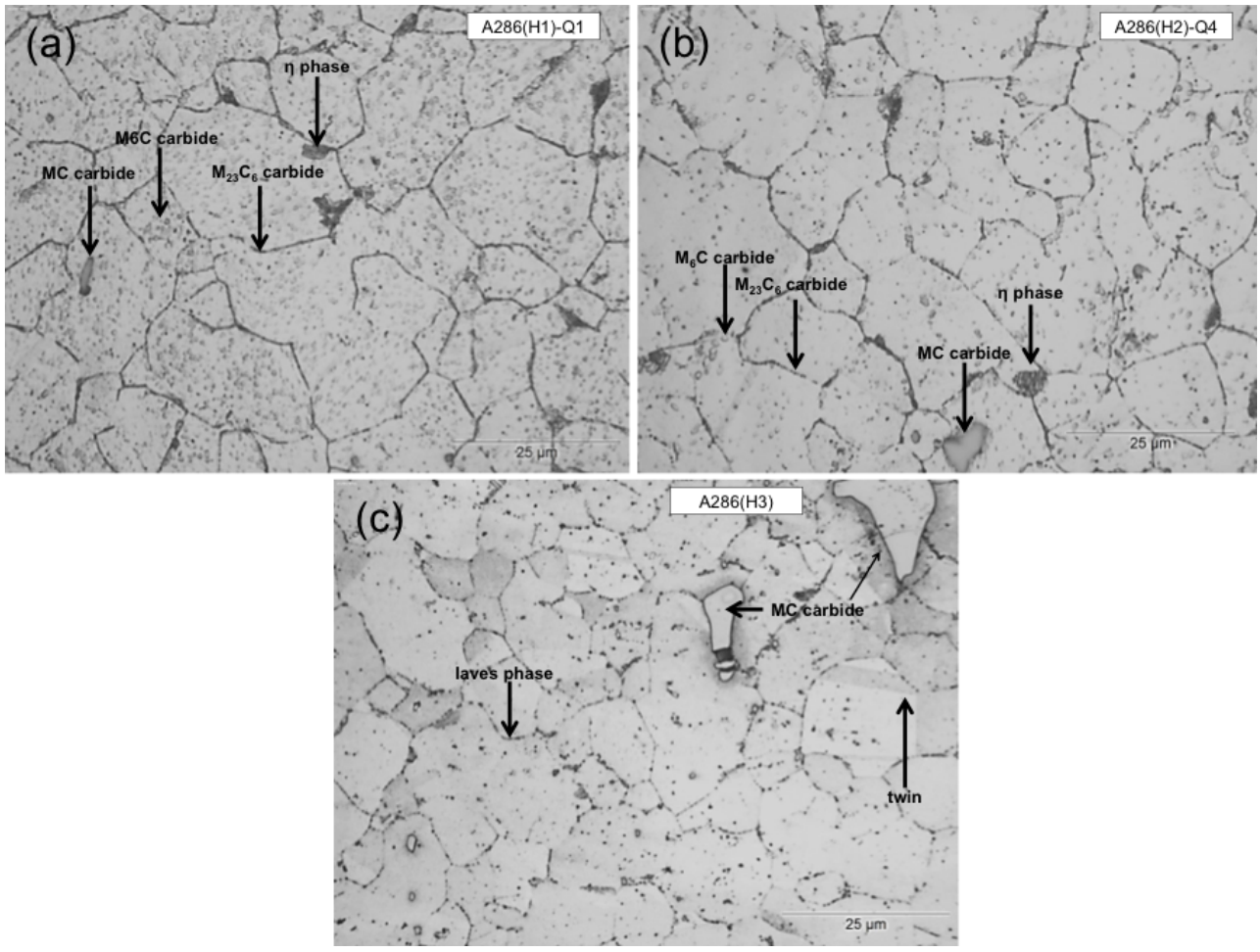

Fig. 3.31. Micrograph of A286(H)-Q1 in (a) H1 region of bulk at the reaction front edge surface and (b) A286(H)-Q4 in H2 region of bulk at the reaction front edge surface and (c) H3 region of bulk away from reaction front; 1000X, Kalling's No. 2

3.2.7. IN718 Microstructural Analysis

Fig. 3.32 provides regions from which micrographs in Fig. 3.34-Fig. 3.37 were obtained and Fig. 3.33 provides regions from which micrographs in Fig. 3.38- Fig. 3.41 were obtained.

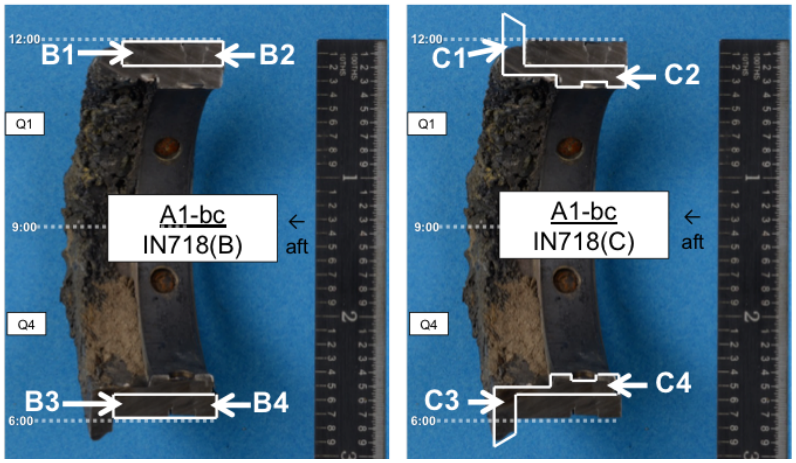

Fig. 3.32. Image of Sample A1-bc with Regions B1-B4 of IN718(B) and Regions C1-C4 of IN718(C) labeled and outlined in white.

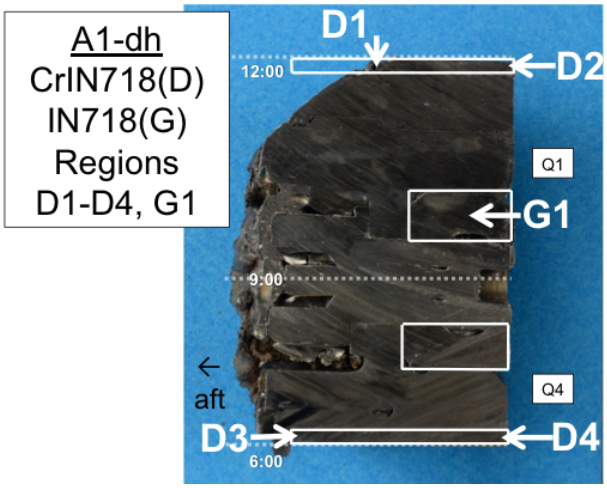

Fig. 3.33. Image of Sample A1-bc with Regions D1-D4 of CrIN718(D) and Region G1 of IN718(G) labeled and outlined in white.

3.2.7.1. IN718(B) and IN718(C)

The microstructure at the reaction front of IN718(B) provided in Fig. 3.34a-d contained extensive precipitation with less precipitation prevalent moving away from the reaction front in Q1. The opposite was seen in Q4, with IN718(B) containing more precipitation away from the reaction front than near the reaction front as shown in Fig. 3.35a-d.

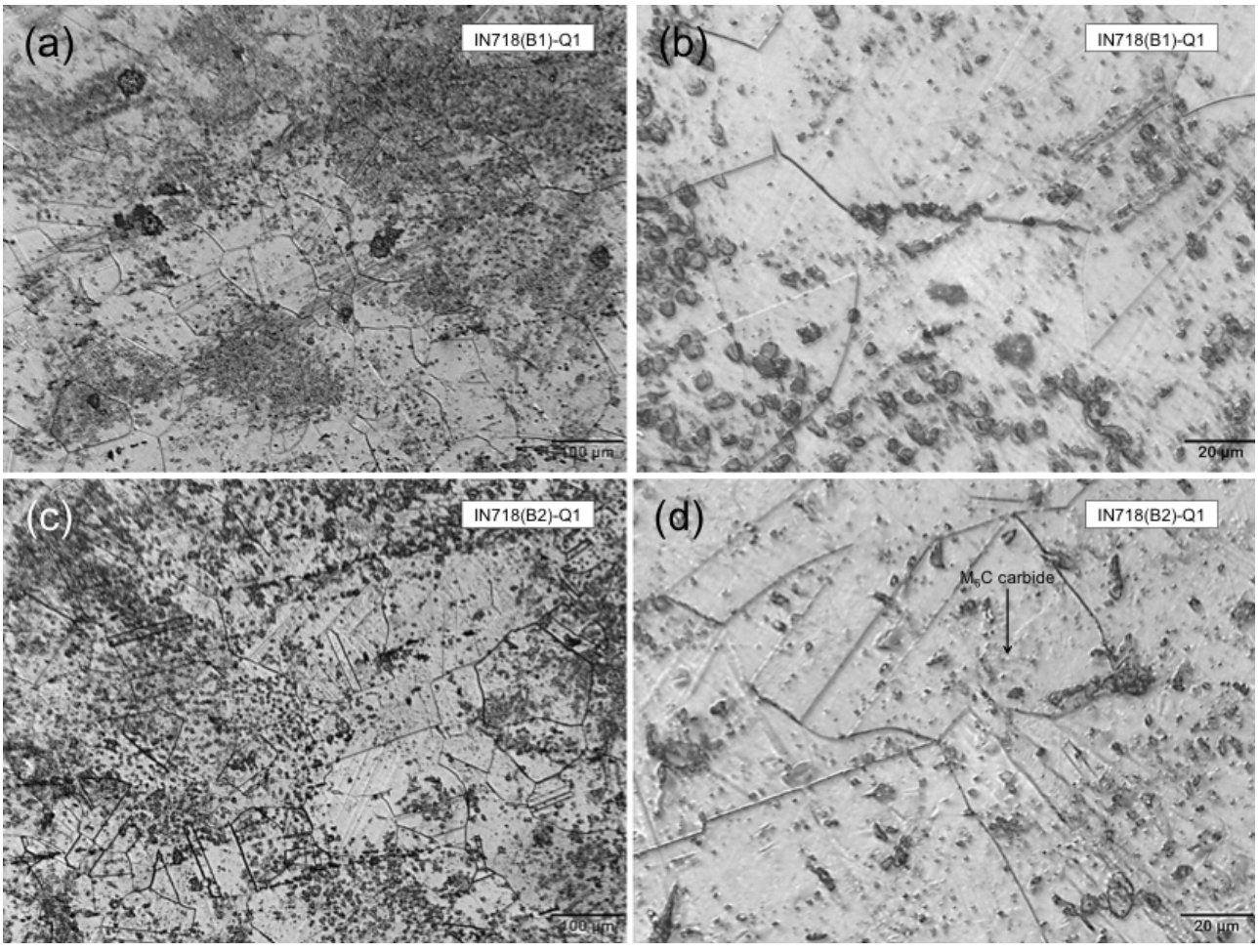

Fig. 3.34. Micrograph of IN718(B)-Q1 in (a) B1 region of bulk reaction at the front edge surface, 100X, (b) 500X (c) B2 region of bulk away from reaction front, 100X, (b) 500X; Kalling's No. 2.

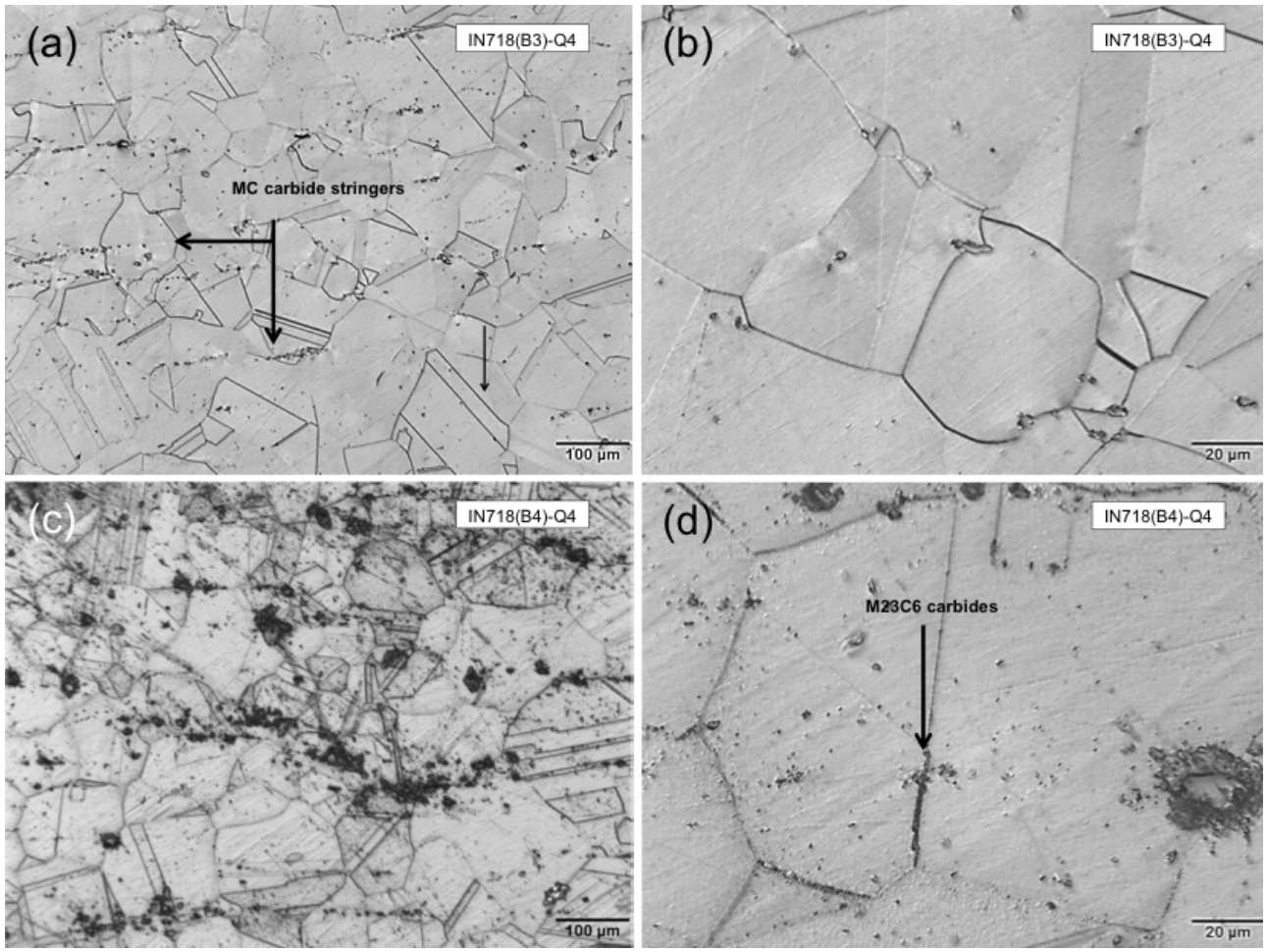

Fig. 3.35. Micrograph of IN718(B)-Q4 in (a) B3 region of bulk reaction at the front edge surface, 100X, (b) 500X (c) B4 region of bulk away from reaction front, 100X, (b) 500X; Kalling's No. 2.

The microstructure of IN718(C)-Q1 at the reaction front (Fig. 3.36a) exhibited material loss and consisted of a solid solution of γ matrix with a high

prevalence of liquated second phase particles, an indication of overheating. Indication of overheating lessened moving away from the reaction front (Fig. 3.36b-d) In Q4, liquation was not present within IN718(C) and carbide precipitation was less prevalent throughout the Q4 sleeve as seen in Fig. 3.37a-d.

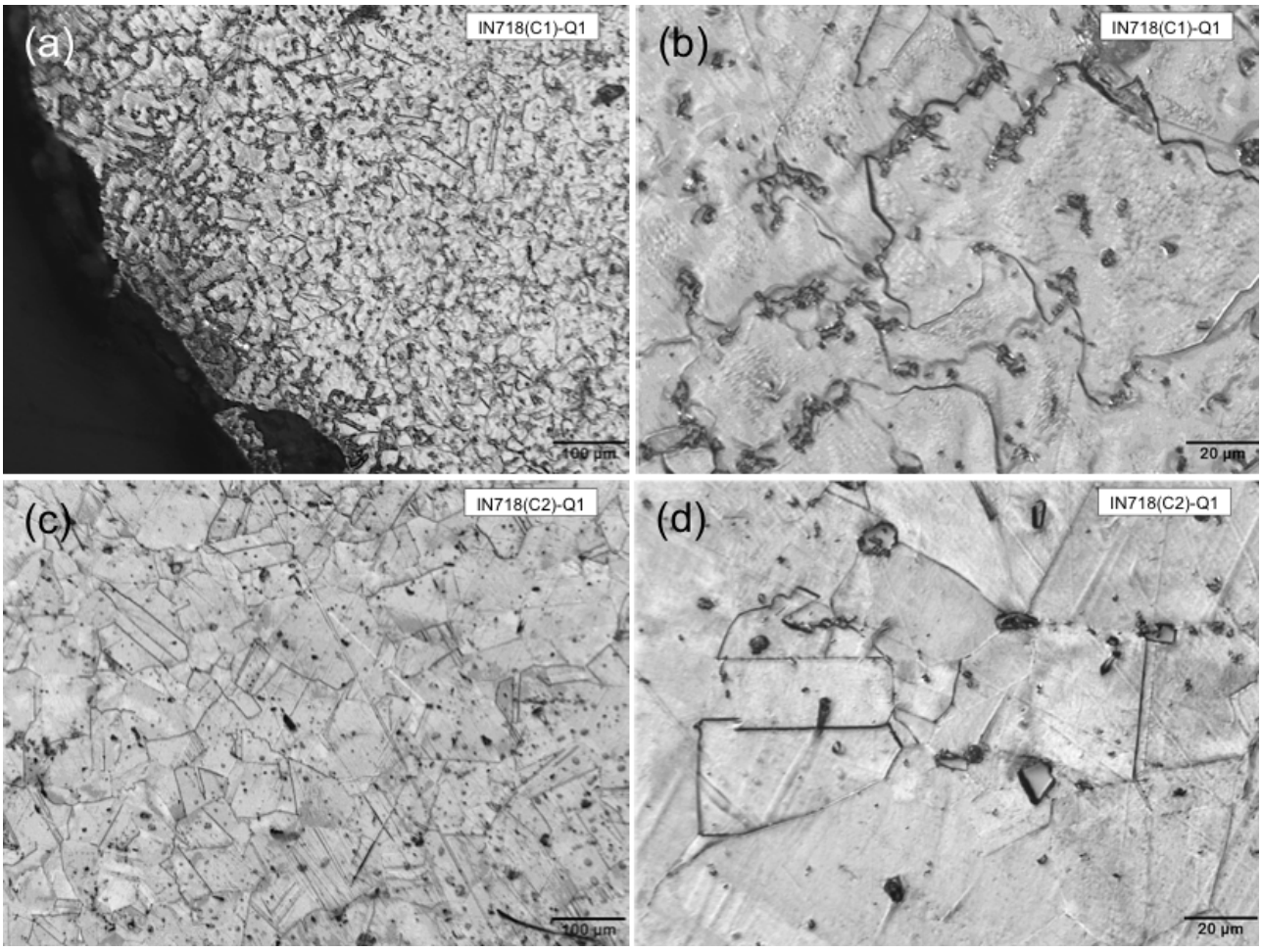

Fig. 3.36. Micrograph of IN718(C)-Q1 in (a) C1 region of bulk reaction at the front edge surface, 100X, (b) 500X (c) C2 region of bulk away from reaction front, 100X, (b) 500X; Kalling's No. 2.

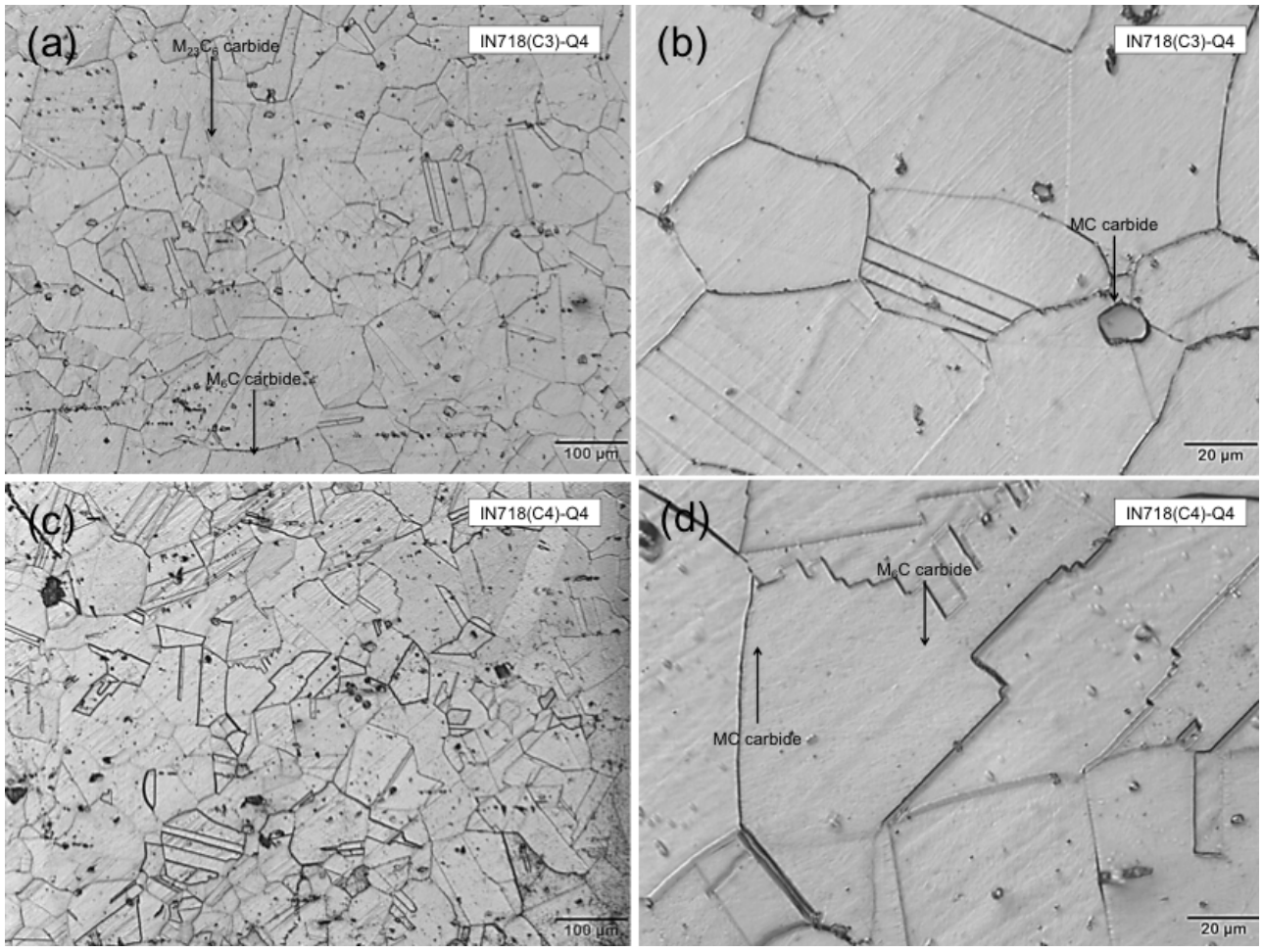

Fig. 3.37. Micrograph of IN718(C)-Q4 in (a) C3 region of bulk reaction at the front edge surface, 100X, (b) 500X (c) C4 region of bulk away from reaction front, 100X, (b) 500X; Kalling's No. 2.

Also observed moving away from the reaction front, the microstructure of both IN718(B) and IN718(C) in Q1 and Q4, contained stringers of MC-carbides and minimal grain boundary precipitation. Annealing temperatures, 980-1230 ˚C (1800-2250 ˚F), allow for the solutionizing of second phase particles, as seen in the regions away from the reaction front and evidenced by the presence of annealing twins.

3.2.7.2. CrIN718(D) and IN718(G)

At the reaction front, the microstructure of the CrIN718(D)-Q1 sleeve was typical of an overheated structure containing an equiaxed γ matrix with extensive, coarse γ' precipitates dispersed in a non-uniform manner, shown in Fig. 3.38a-b. The heavy precipitation in the BSE micrograph of Fig. 3.38b is shown in relief. The BSE micrograph in Fig. 3.39 shows the chrome plating of the of CrIN718(D)-Q1 sleeve near the reaction front where damage and weakening adherence was apparent in a region adjacent to RSMM. Also illustrated in the BSE micrograph are the coarsened γ precipitates in relief of the image. Away from the reaction front the chromium plating exhibits minimal damage, containing minor, transverse crack-like features. Blocky MC-type carbides and nitrides were also observed within the bulk CrIN718(D) microstructure with clean grain boundaries. Away from the reaction front, Fig. 3.38c-d, MC-type carbide precipitation was observed, but was less prevalent in this region and γ‘ precipitates are not resolved. This microstructure is typical of that seen along the length of CrIN718(D)-Q4.

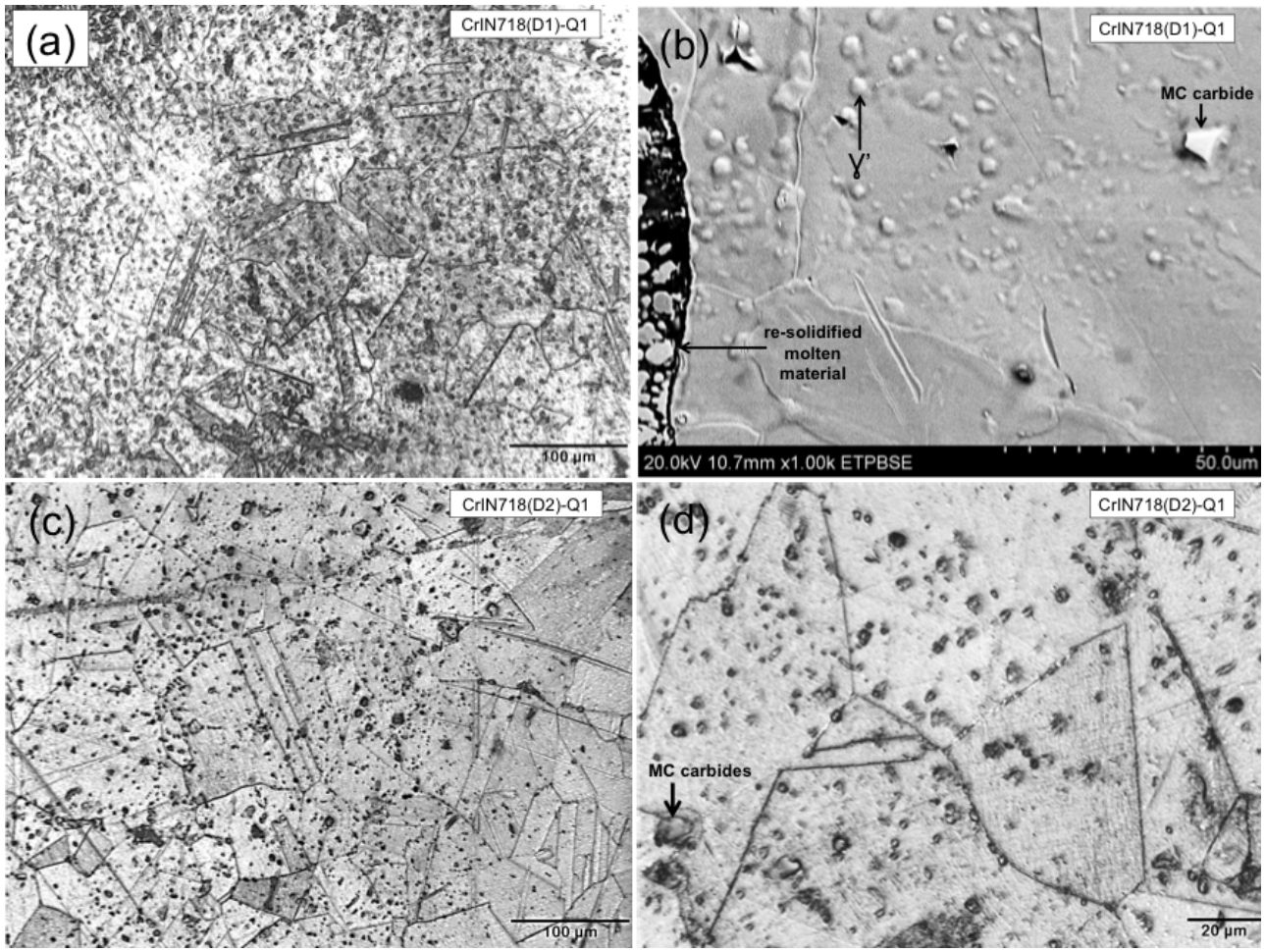

Fig. 3.38. Micrograph of CrIN718(D)-Q1 in (a) D1 region of bulk at the reaction front edge surface, 150X and (b) BSE micrograph in D1 region; micrograph of D2 region of bulk away from reaction front, (c) 150X, (d) 500X; Kalling's No. 2.

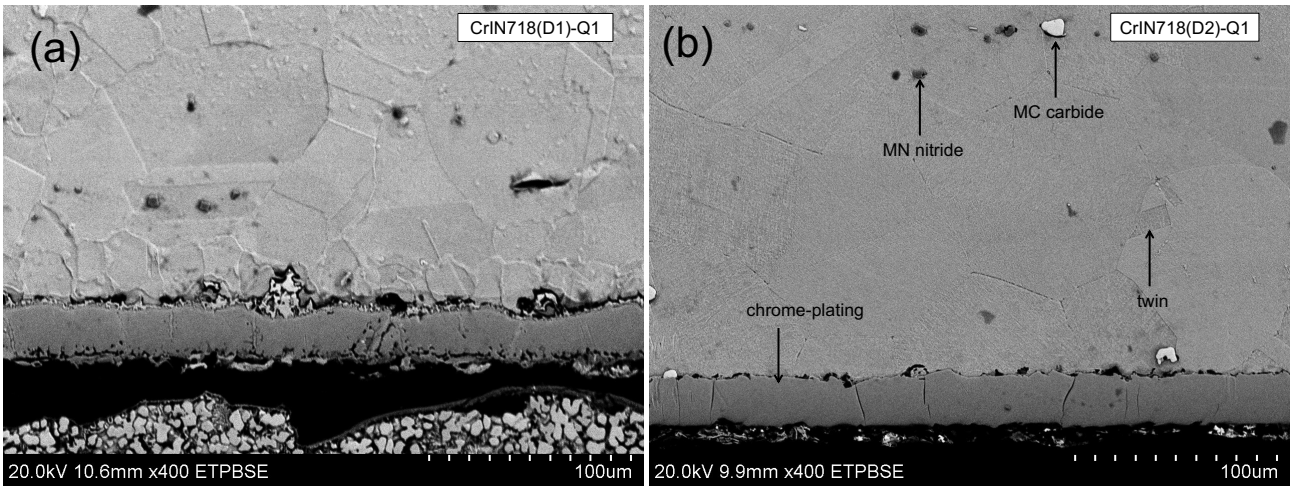

Fig. 3.39. BSE micrograph of CrIN718(D)-Q1 in (a)-(b) D1 region of bulk at the reaction front edge surface and in (c)-(d) D2 region of bulk away from reaction front.

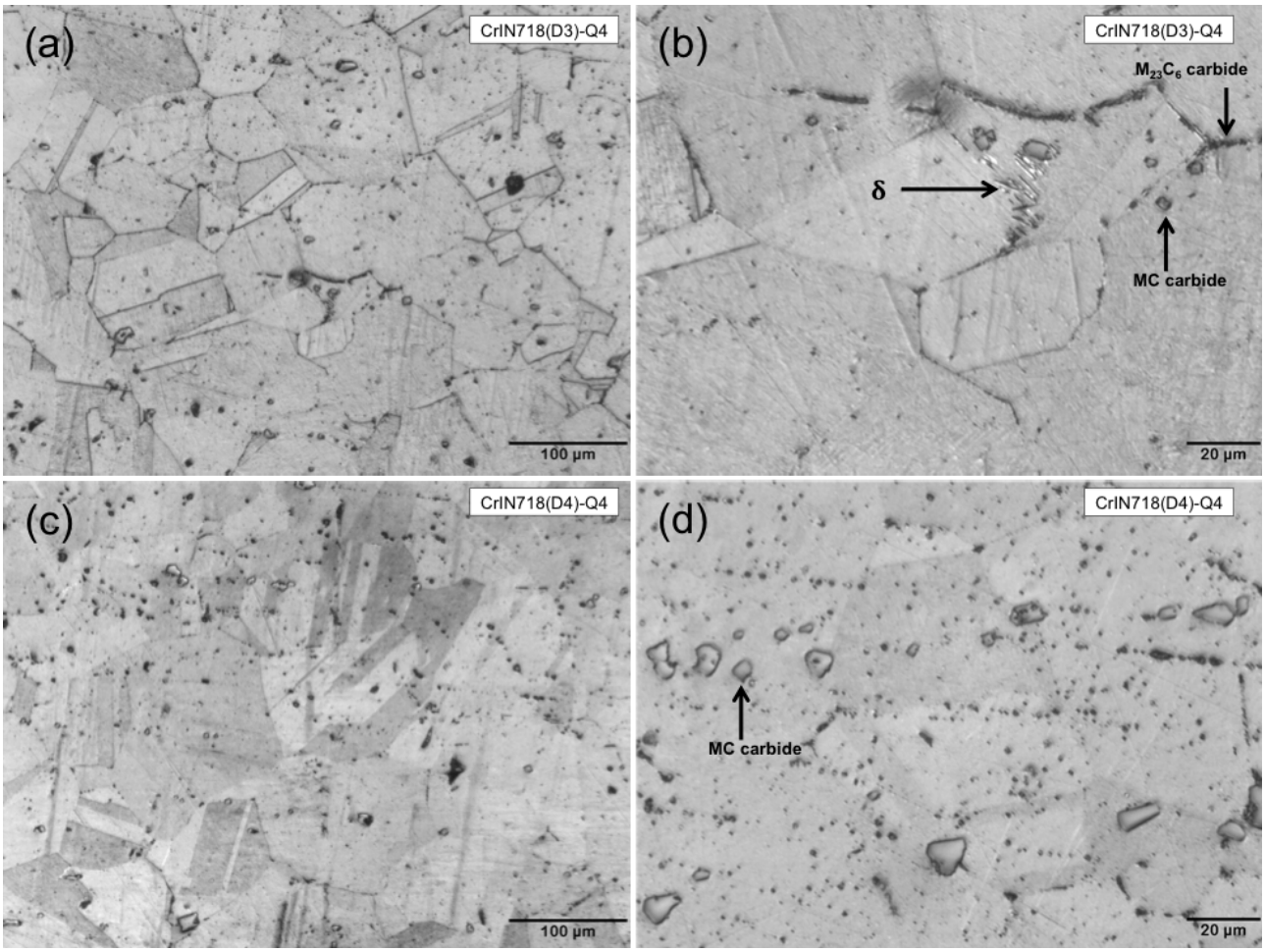

Fig. 3.40. Micrograph of CrIN718(D)-Q1 in (a) D3 region of bulk reaction at the front edge surface, 100X, (b) 500X (c) D4 region of bulk away from reaction front, 100X, (b) 500X; Kalling's No. 2.

Fig. 3.41 depicts the microstructure of IN718(G)-Q1 at the reaction surface and represents the structure observed throughout IN718(G)-Q1 and CrIN718(D)-Q4, at and away from the reaction front. The austenite grains contain twins and dispersed fine γ' precipitates throughout the matrix. The microstructure exhibits banding where Mc-type carbide segregation was present likely due to grain

refinement within unidirectional shear bands resulting from plastic deformation working process and subsequent annealing at 950-1120 ˚C (1750-2050 ˚F).

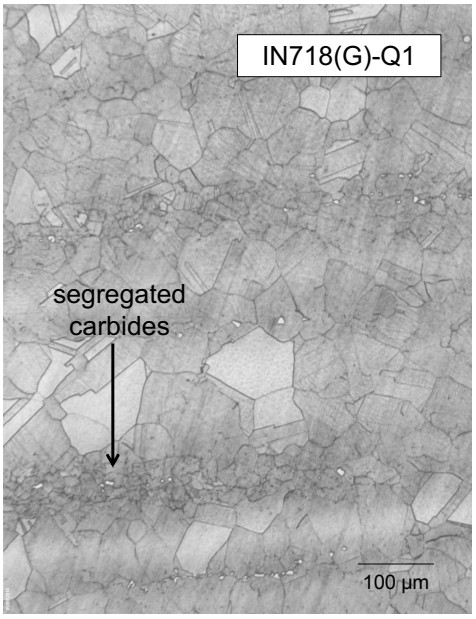

Fig. 3.41. Micrograph of IN718(G)-Q1 in G1 region of bulk, 100X; Kalling's No. 2.

3.2.8. Microstructural Analysis of Arc-jet Specimens

The arc-jet plates were examined through their cross section with the arc-jet flow facing the bottom of the image and the back side of the plate at the top of Fig. 3.42a-d which depict the microstructural features of the arc-jet samples. The unaffected plate, Fig. 3.42a contained globular α and intergranular β. The grains are slightly elongated, likely the result of the working process. The

unaffected plate structure serves as the representative original microstructure of the tested samples from Class I-III.

Alpha-case was observed on the leading edge of the tested samples, Fig. 3.42b. suggesting Class I to have the thickest α-case layer compared to Class II and Class III. The α-case edge surface on the Class I sample was smooth and the α-case layer was relatively uniform and featureless with minor cracking apparent. The α-case layer transitioned into a coarsened plate morphology, that appeared as finger-like projections, before transitioning into a Widmanstätten structure.

The Class II edge surface was rough and the α-case layer, also exhibiting a featureless full-α composition, similarly contained finger-like coarse plate-like α that transitioned into a Widmanstätten structure. Moving into the bulk, the basketweave colonies transformed into a partial martensitic structure with a prior β grain boundary appearing as a boundary between the two morphologies.

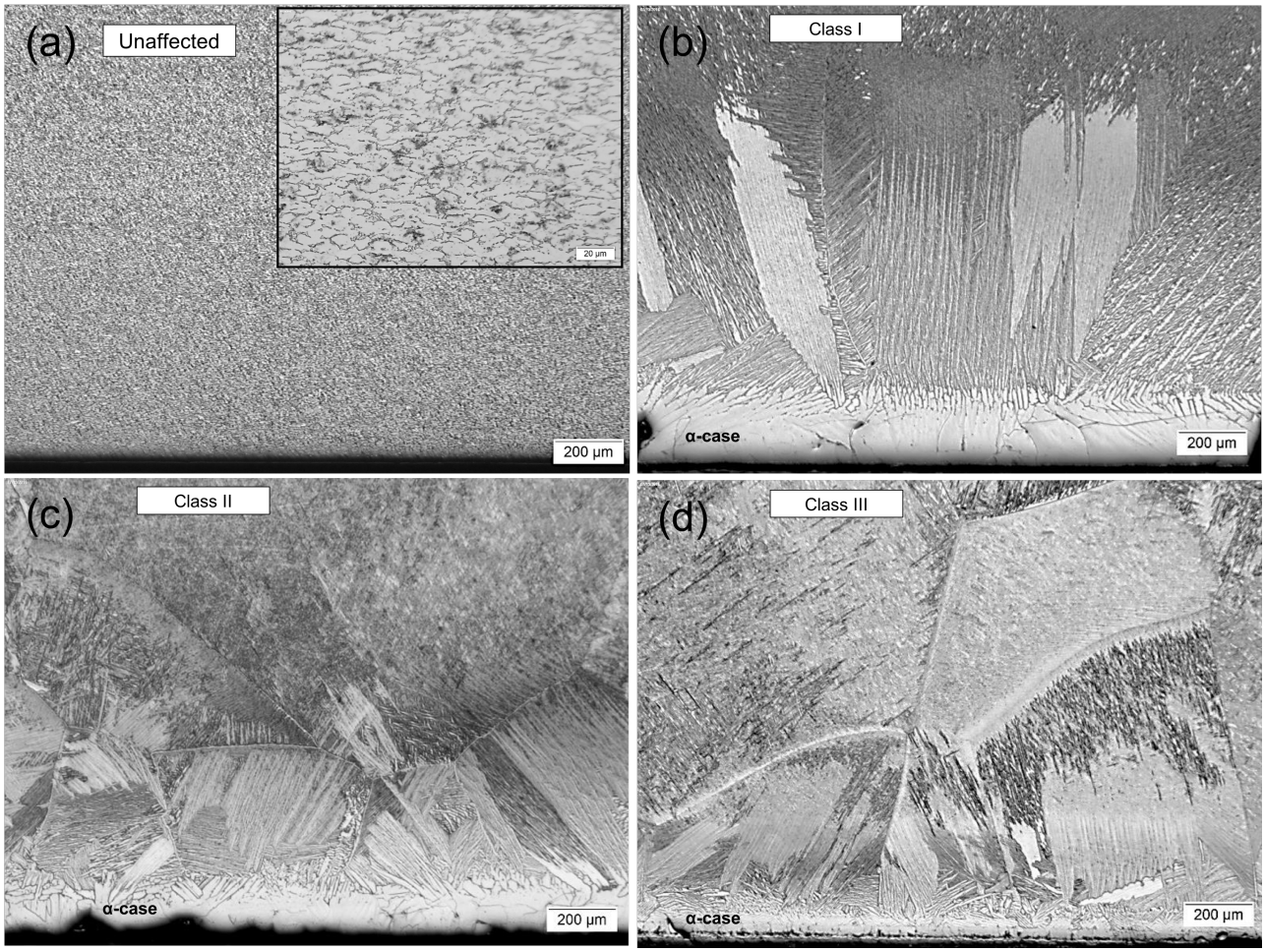

Fig. 3.42. Micrographs of arc-jet samples, (a) unaffected (b) Class I (c) Class II, (d) Class III; Kroll's.

The α-case layer of Class III contained voids and longitudinal cracking along its length and the finger-like coarse α plates appeared more woven as it transitioned into a Widmanstätten structure beyond which partial to fully martensitic grains were apparent. Grain boundaries at the interface between

Widmanstätten and the martensitic structure were distinct, appearing light in appearance with the enrichment of α phase.

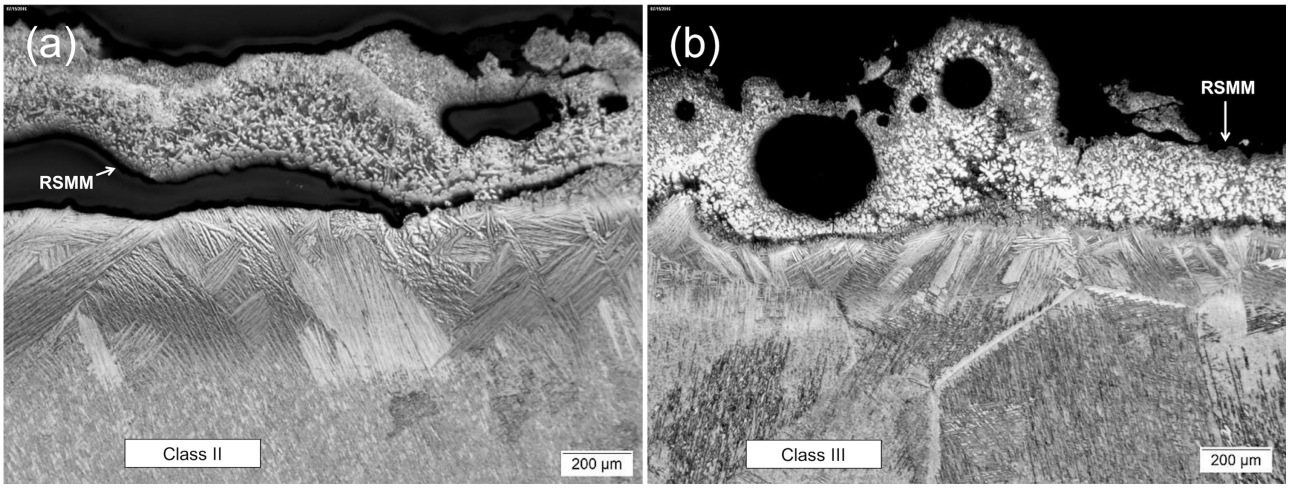

Fig. 3.43. Micrographs of (a) Class II and (b) Class III arc-jet samples; Kroll's.

On the surface of Class II and Class III samples, RSMM was observed and characterized by a globular, dendritic morphology. The RSMM shown in Fig. 3.43a-b, contained spherical and irregular pores of various sizes along with cracking and interdendritic voids. Void coalescence appeared to be the cause of the weak adherence seen in Fig. 3.43a where the RSMM was separated from the bulk surface. Beyond the RSMM, the edge bulk surface contained coarsened plate-like α, similar to that previously described for Ti6Al4V(E) and Ti6Al4V(F). The region of coarsened plate-like α appeared lighter in color nearest to the surface

and exhibited a basketweave morphology as it transitioned into large grains of acicular α and martensite.

3.3. Discussion

3.3.1. PLBD Roller Surface Features

The sloped pattern of the roller resulting from material loss of titanium and nickel sleeves supports the theory of aft-end travel of the forebody during shuttle breakup. The formation of the degradation product may point to orbiter flow during breakup and directionality of reaction propagation. The area of initial thermal excursion may be narrowed to the region of Ti6Al4V(E) sleeve where material loss is greatest. Thus, in addition to its in-flight proximity to the crew module overhead windows, the characterization of damage to PLBD roller further substantiates the likelihood that the titanium of the PLBD roller served as a source of the char layer deposition.

The presence of non-native elements observed on the surface of the roller is likely due to a combination of contamination from the atmospheric debris field during shuttle break up and/or ground impact, (soil is known to contain phosphorus, zinc, copper and silicon). The significant amount of aluminum found on the reaction front surfaces suggests the incorporation of ablated

material from the adjacent bulkhead regions, where significant material loss was present or the presence of Al_2O_3. from high temperature oxidation of titanium as previously described.

It can be well-reasoned that the oxygen-rich, superheated hypersonic flow conditions experienced by the orbiter during re-entry and subsequent vehicle breakup allowed for high temperature oxidation to occur within various regimes. Chemical analysis showing a variation in relative oxygen concentrations can be attributed to the variable degree to which oxidation occurred resulting in the diverse surface morphology observed along the reaction front. The globular oxide morphology and surface voids observed throughout the reaction front appear to be the result of oxygen dissolution at the surface. The spherical structures are likely hollow, and the pore may represent an interior look into the oxidation reaction products - the most notable surface pore containing a purple patina interior coating [64]. Velten et. al. reported purple color of TiO_2 upon increased thickness of oxide formation (150-180 nm) [65] and Strobridge et al. analyzed solidified ejected droplets obtained from titanium combustion reaction and reported the solid droplets to be hollow spheres of TiO_2. [66]

The RSMM composition suggests that the Ti-6Al-4V and IN718 sleeves as sources of the molten material, with microstructures representing a mixed elemental composition typical for both alloys. The solidification structures observed indicate localized heating to the associated alloy melting temperatures, the highest of which is chromium plating of CrIN718(D): T_m = 1370-1926 ˚C (2500-

3500 ˚F). Analysis of the cross-section revealed the distribution and nature of the RSMM. The RSMM was observed as deposition over the less degraded Ti6Al4V(F) and A286(H) sleeves, suggesting the melt travelled (or forced) downward, its thickest deposition positioned at the Q4 region. RSMM observed within inner sleeve spacing, is consistent with the hot gas flow direction previously outlined in Fig. 1.4d.

3.3.2. High Temperature Oxidation

High temperature oxidation, a precursor to combustion, is further evidenced by the α-case formations observed along the reaction front surface. The oxygen enriched α-case develops simultaneously with the formation of the oxide layer as interstitial oxygen (or nitrogen) migration in this area stabilizes the α phase leading to a brittle supersaturated α region, as well as increased hardness within and beyond the depth of the α-case layer. The α-case depth increases with thermal oxidation temperature and time, just as with the oxide layer [67], mainly following a parabolic relationship at 590 ˚C (1100 ˚F) and 700 ˚C (1290 ˚F) in Ti-6Al-4V. [67] The presence of multilayered α-case layers along the RSMM points to prolonged high temperature oxidation occurring after the initial high temperature excursion that caused melting, as well as to the occurrence of subsequent deposition of molten material over top material with an already formed α-case layer.

The difference in α thickness observed along the titanium surfaces and the RSMM provides insight into the varying extent of oxidation along the surface and the dynamic break up environment. With increasing temperatures, diffusivity of oxygen is increased, which serves as a possible explanation for the increased α-case thickness of the RSMM as compared to the bulk surface.

Increased hardness measurements obtained nearest to the reaction front is consistent with the α-case present in the region and the sustained hardness readings seen beyond the presence of α-case can be attributed to the martensitic microstructure and possible diffused oxygen [31]. Interstitial oxygen and nitrogen are known strong α-phase stabilizers in Ti-6Al-4V and influence the martensitic transformation of β-phase to α'-phase. [68] The first hardness value, followed by a decrease in hardness then subsequent high values, may be the result of multi-layered α-case formation within the RSMM.

The absence of distinct oxide layers may be explained by spalling as it has been shown that oxide scales composed of TiO_3 or TiO_2 may form a thick, porous, multi-layered oxide structure above 700 ˚C (1290 ˚F) and may become sintered and/or de-bonded from the surface at this elevated temperature. [27] Sefer et. al. described that at elevated temperatures, titanium oxides become porous and spall off, leading to an increase in oxidation rate. [69] In addition to this fact, the orbiter during re-entry is known to approach up to Mach 3 speeds, which would provide sufficient force to fracture and remove a thermally compromised oxide

layer, rendering the metal surface beneath unprotected and vulnerable to accelerated oxidation if the promoting conditions were satisfied.

3.3.3. Geometrical Factors Shown to Influence Ignition

Ignition of titanium has been shown to be dependent upon several factures such as oxygen pressure, sample temperature, sample geometry and oxide layer [69] fracture, [54] all factors that were more than likely present during break-up given the evidence presented thus far.

The roller design, in which the titanium components contain a machined lip at the roller face, provided a small cross-sectional area exposed to the re-entry flow. Strobridge described the occurrence of preferential combustion behavior for thin regions of turbine blades, postulating that localized damage to thin leading and trailing edges may be explained by several possible contributing factors: conduction away from the combustion site is inhibited by the small cross-sectional area, raising local temperature to a critical ignition temperature. [41] Of the materials discussed, titanium provides the lowest thermal conductivity capability. This thermal property of titanium tends to prohibit transfer of energy over a large volume, resulting in small regions of localized, elevated heating where ignition temperatures can be achieved.

The configuration of the roller is such that lip regions of the titanium sleeves overlap providing a notched area extending along the perimeter of the

roller face. The machined lip may have served as a protuberance in the oxidizing flow environment, a factor shown by Olivas to promote an ignition and/or combustion event. The protuberance may have provided a localized region of small volume where heat accumulation could occur, further promoted by the notch corner in which oxygen flow could impinge at increasingly high pressures. It is reasonable to expect ignition to occur more readily in this 'hot spot' with the consideration of titanium's low thermal conductivity.

Furthermore, it is well understood that as the oxidizing surface area to volume ratio (S_v) increases, ignition may occur more readily. If the available oxidizing surface area is large with a small bulk volume to absorb the energy produced, ignition is more likely as heat transfer away from the reaction region becomes less than the heat generated within the region. The exposed titanium surface area of the roller face upon which hypersonic flow may have impinged was approximated to be 7.6-cm^2 (3.0-in^2). From measurement approximations, S_v for the titanium at the reaction front surface was determined to be 0.22 throughout the radial bulk regions and 18.9 for the outermost ledge portion of Ti6Al4V(E). This area of the ledge has a markedly higher S_v due to the lack of overlap by adjacent sleeves, allowing exposure of oxygen to flow along all sides of the ledge.

If the titanium ignited at the ledge, this small region could serve as a kindling point, as its exothermic reaction may have released a sufficient amount of heat to raise the temperature of surrounding titanium to a critical ignition

temperature. Serving as a compounding effect, the CrIn718(D)-Ti6Al4V(E) ledge interface may have provided a confined space at which heat accumulation could have occurred. The material loss and melting of neighboring CrIN718(D) also provides reasonable basis for the argument that a localized heat excursion occurred at the lip region along with the observation that this theorized initiation site corresponds to the region that sustained the most thermal damage.

3.3.4. Microstructural Analysis

For high-purity titanium alloys and α-stabilized alloys, serrated α is produced upon quenching from above the β transus. As the concentration of β-stabilizing elements increase, the transformation upon quenching results in acicular α. [70] The Ti-Al-N alloys have also shown to form serrated α upon quenching. [71] The bimodal microstructure consisting of slightly elongated primary α within transformed β was concluded to be the initial microstructure of both titanium sleeves. Annealing to 650-815 ˚C (1200-1500 ˚F), results in recrystallization of elongated structures, providing reasonable basis for the assumed initial condition.

The microstructural gradient present within the microstructures suggests uneven transfer of heat within the roller components. Each component exhibited microstructural gradients at various depths moving away from the reaction front. The microstructures observed indicate a thermal gradient heating where the

reaction front experienced the highest temperatures and moving away from the surface into the bulk the temperature to which the roller was exposed decreased.

Heating to above the β transus 980 ˚C (1800 ˚F) with subsequent fast cooling yields the martensite microstructure observed beyond the α-case layers of the reaction front for both Ti-6Al-4V sleeves. The transition, moving away from the reaction front, into a coarse, lamellar α structure represents a slower cooling rate from above the β transus. Another transition occurs for Ti6Al4V(E)-Q1, as acicular α transforms into a bimodal microstructure that is typical for Ti-6Al-4V when heated to temperatures below the β transus. This remaining bulk of Ti6Al4V(E)-Q1 consisted of this bimodal microstructure and was assumed to represent the initial microstructure of Ti6Al4V(E).

The Ti6Al4V(F)-Q1 microstructure did not transition into a bimodal morphology but instead retained a lamellar structure that coarsened moving away from the reaction front. The Ti6Al4V(F) microstructure in the Q4 region closely mirrors that of the Q1 with the same transition of martensite – acicular α occurring at a depth closer to the reaction front and no bimodal microstructure present. To the extent of the author's knowledge, Ti6Al4V(F) was not processed differently than Ti6Al4V(E). Assuming the initial microstructure is the same for both Ti-6Al-4V sleeves, it can be implied that the initial bimodal microstructure of the Ti6Al4V(F) sleeve experienced a complete transformation during breakup due to relatively bulk heating above the β transus. This is supported by observed deposition of RSMM along the reaction front surfaces of Ti6Al4V(F), suggesting

intimate contact with, and heating of, Ti6Al4V(F) by the molten metal flow, followed by slow cooling.

The presence of α_2 observed in both Ti6Al4V(E) and Ti6Al4V(F) appears to be the result of gas dissolution of both oxygen and nitrogen. When Ti-6Al-4V is over aged at 500-600 ˚C (930-1110 ˚F), fine ordered α_2 precipitates form homogenously within the α phase. [72, 73]

The volume fraction of β increases when heat treated above the β transus temperature and quenched. The β phase is known to contain less aluminum than the α phase. Rapid cooling rates result in the increase in β and increase in diffusion of aluminum to α-Ti. With the increased concentration of aluminum within the remaining α phase, the formation of α_2 is possible. [74] What was observed within the Ti-6Al-4V sleeves of the roller was in good agreement with the findings reported by Lee [72, 73]. For the Ti-6Al-4V sleeves, α_2 was present within region that contained acicular or lamellar structures, corresponding to heating above the β transus. Within the region where a bimodal microstructure is present, representing heating below the β transus, α_2 is absent.

The TiN is the result of nitrogen dissolution from the re-entry environment, which has a composition that is close to that at sea level. The relative intensities of both α_2 and TiN varied between the Ti6Al4V(E) and Ti6Al4V(F), corresponding to the variation in gradient observed between the two sleeves. The presence of TiN appears to coincide with the acicular microstructure present nearest to the reaction front and the lamellar basketweave structures

that were observed throughout the bulk of the Ti6Al4V(F) sleeve, but for Ti6Al4V(E), the TiN peaks were absent in regions corresponding to acicular and lamellar structures and Ti_2N became apparent within the bimodal structure located in regions farthest away from the reaction front.

3.3.5. Comparison to Arc-jet Specimens

Although the re-entry conditions to which the PLBD rollers were exposed are not well-defined, the arc-jet samples still served as a baseline reference for ignition/combustion characteristics, given the known test parameters under which the samples reacted.

Other possible factors that do not allow for a direct correlation to the arc-jet samples include titanium sleeve geometry, sleeve configuration with a multi-alloy construction, and unknown initial microstructural state or in-flight thermal history.

The microstructure along the reaction front surface bore similarities to that of arc-jet samples, the greatest resemblance being to that of Class II and Class III specimens. Partial martensite was apparent within the bulk of the arc-jet samples and α-case formation along the reaction surface was present, along with the transitional region extending of plate-like α extending into the bulk. The RSMM, although not incorporated with other alloy systems, was similar in that pores were present, representing oxygen dissolution.

These observations, relating the microstructural features of Ti-6Al-4V within the PLBD roller to arc-jet samples, are in good agreement to the findings reported from a forensic study of thermally degraded Ti-6Al-4V X-links recovered from the *Columbia* accident. [75]

3.4. Conclusions

An extensive characterization of a recovered PLBD latch roller from Space Shuttle *Columbia* was performed to evaluate material behavior during atmospheric re-entry of Ti-6Al-4V with an emphasis on the identification of ignition and/or combustion behavior. The nature of the damage observed on the roller provided an opportunity to compare features of heavily degraded region to regions that appeared nearly un-affected. The construction of the roller also offered a unique perspective in that Inconel 718 and A-286 superalloys of the roller were also evaluated. Features suggestive of accelerated oxidation were observed for the Ti-6Al-4V sleeves along with the fulfillment of several geometrical factors that have been shown to promote ignition. It is understood by the author that due to the complexity of the break-up environment conditions, conclusions must be drawn with caution. The following summarizes observations from this study:

1. Surface features represent dynamic break up environment, reaction initiation, directionality.
2. Re-solidified molten material deposition on. roller consisted of Ti-6Al-4V and IN-718.
3. Material loss of chromium plating (highest melting constituent of PLBD roller) suggests roller experienced temperature as high as 1926 ˚C (3500 ˚F).
4. High temperature oxidation confirmed by presence of α-case layer formation and hardness values.
5. PLBD roller configuration of Ti-6Al-4V sleeves contained features conducive to the onset of ignition.
6. Microstructural features of ignition and combustion observed on arc-jet samples were similar to those observed in analysis of Ti-6Al-4V sleeves of PLBD roller.

Titanium alloys are widely used in the aerospace industry and can be found in many structural components of modern spacecraft. Sub-structural components of space vehicles are not designed to withstand all conditions that arise during space flight, and given the difficulty involved with simulating re-entry conditions, there remains a dearth of knowledge regarding titanium behavior in the high-temperature, low-pressure environment. As an unpredictable response may contribute to accelerated vehicle damage in the event that the TPS is compromised, it is of paramount importance that materials

analyses continue in order to better appreciate the manner in which aerospace alloys may behave during atmospheric re-entry and possible influence on the integrity of surrounding material systems.

Chapter 4

X_o 582 Bulkhead Examination

4.1. Experimental Methods

4.1.1. X_o 582 Bulkhead Surface Characterization

After removal of the PLBD roller, the X_o 582 bulkhead was sectioned into three samples, Sample BhA, Sample BhB and Sample BhC, using an abrasive cut-off saw. A visual inspection of the rollers was performed in the as-received state and high-resolution photographic documentation of all surfaces was obtained using a Nikon D700 digital camera. Through chemical surface surveying, with use of a portable XRF device, a zonal map of element composition was developed as part of the nondestructive inspection. The XRF instrument was unable to make full contact with the surface of the base plate, without also making contact with the surface of the X_o 582 bulkhead, which led to inaccurate and inconsistent results. These and other like situations limited the elemental analysis obtained

by the XRF, therefore elemental analysis is not available all areas, including the base plate and the neck of the outermost sleeve.

4.1.2. X_o 582 Bulkhead Microstructural Evaluation

Samples BhA, BhB, and BhC were further sectioned into sub-sections using a waterjet cut-off saw as shown in Fig. 4.1a. Transverse (T) cross-sectional planes are oriented normal to the laminar broom-straw features will bear the notation, BhA-T and BhC-T. Axial surfaces of which the longitudinal (L) microstructure was evaluated is oriented parallel to fracture surfaces and will be referred to as BhA-L and BhC-L. The same notation will be applied for BhB, where (T) will refer to the transverse cross-section and (L) will refer to the longitudinal sample surface. All sample cross-sections were spot etched with Keller's reagent (95-mL H_2O, 2.5-mL HNO_3, 1.5-mL HCl, 1-mL HF) and analyzed using LOM with an Olympus PME 3 inverted light optical microscope. Use of SEM also provided analysis of the microstructure, including BSE imaging, both with the previously listed instrument parameters applied. Second-phase particles were chemically typed using the EDAX EDS capability of the SEM.

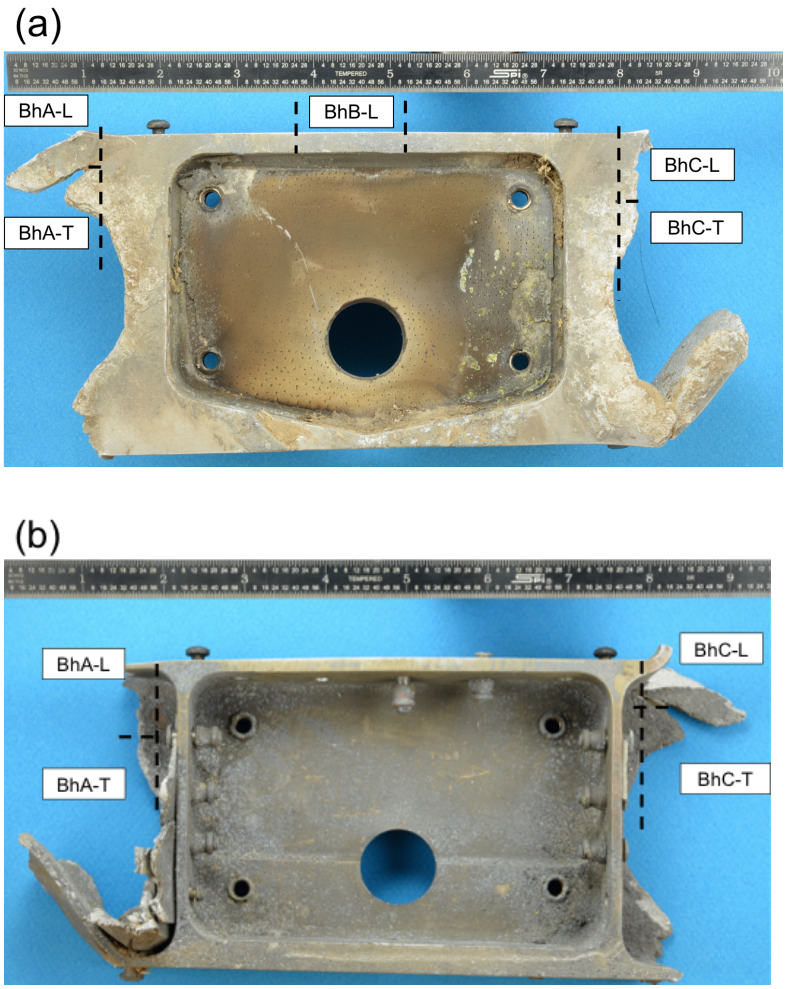

Fig. 4.1. Portion of X_o 582 ring-frame bulkhead with PLBD latch roller removed. Black dashed lines outline sectioning implemented to isolate samples BhA, BhB and BhC. Black arrows indicate surfaces of which microstructural evaluation was carried out and notation refers to longitudinal “L” surfaces the cross sectional, transverse “T” surfaces.

4.2. Results

4.2.1. X_o 582 Bulkhead Fractographic Analysis

From the fractographs obtained by SEM, different fracture surface features were revealed. The fractograph in Fig. 4.2 shows large elongated grains with deformation consistent with features observed macroscopically in Fig. 1.5. Moving away from this area, features of mixed mode fracture were observed. Adjacent to the broom-straw features, the fracture surface was characterized by elongated dimples, indicative of a ductile fracture mode.

4.2.2. X_o 582 Bulkhead Microstructural Evaluation

Fig. 4.3-Fig. 4.5 present microstructures of the broom-straw fracture region which consisted of elongated, slightly dendritic grains with intergranular cracking and heavy precipitation. Partial recrystallization was also apparent, as shown at high magnification in Fig. 4.3b. Liquated precipitates were prevalent at grain boundaries, adjacent to which a PFZ was evident, measuring approximately 10- to 15-μm, Fig. 4.3b. Coarse and irregular-shaped particles were also seen located at grain boundaries, as well as within the grains where evenly distributed spherical particles were present, some of which exhibited a rosette morphology as outlined in Fig. 4.3b.

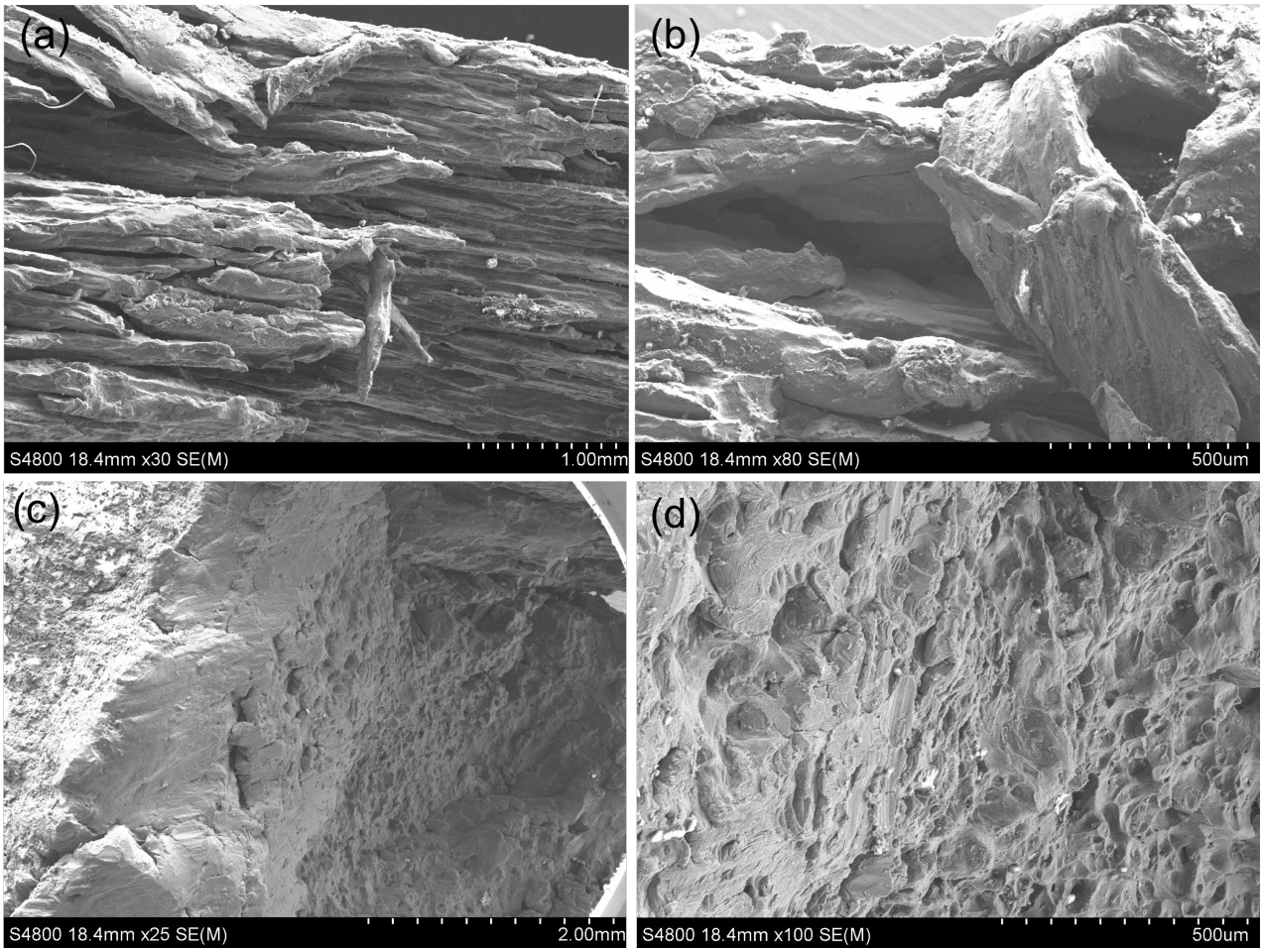

Fig. 4.2. Fractographs of (a) broomstraw features and (b) ductile mode fracture features observed on BhA.

Fig. 4.5a-b display the microstructure of the deposition observed on the backside of the bulkhead contained a mixed morphology of globular grains with dark, charred regions apparent throughout along with gray coarse gray particles. White globular grains were seen along the outside edge surface of the deposition and closely resembled the partially recrystallized aluminum grains of the

bulkhead microstructure. Adjacent to the deposition, dendritic grains with inter-dendritic particles characterized the microstructure, as shown in Fig. 4.5c. In some regions, the deposition appears to be incorporated into the bulk structure of the bulkhead, Fig. 4.5d.

Grain morphology and orientation observed on longitudinal and transverse microstructures indicated a flattened, elongated grain structure that extended along the axis of the bulkhead. The elongated grain structure was also apparent in regions away from the fracture surface, Fig. 4.6, suggesting the original bulkhead was constructed with a cold-worked aluminum product.

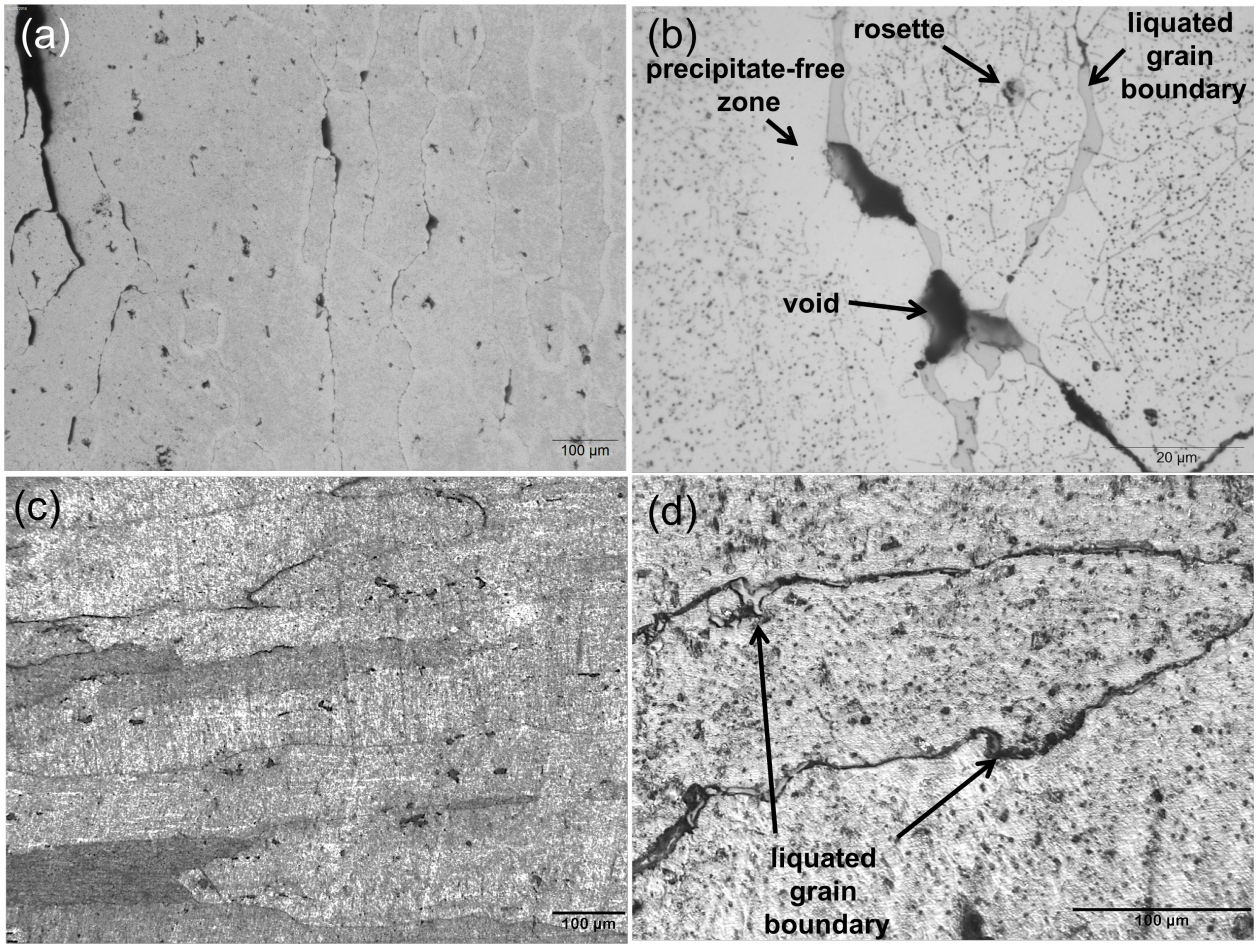

Fig. 4.3. Transverse broom-straw microstructure, BhA-T; etched with Keller's reagent (a) 100X and (b) 1000X; longitudinal broom-straw microstructure, BhA-L; etched with Keller's reagent (c) 100X and (d) 500X.

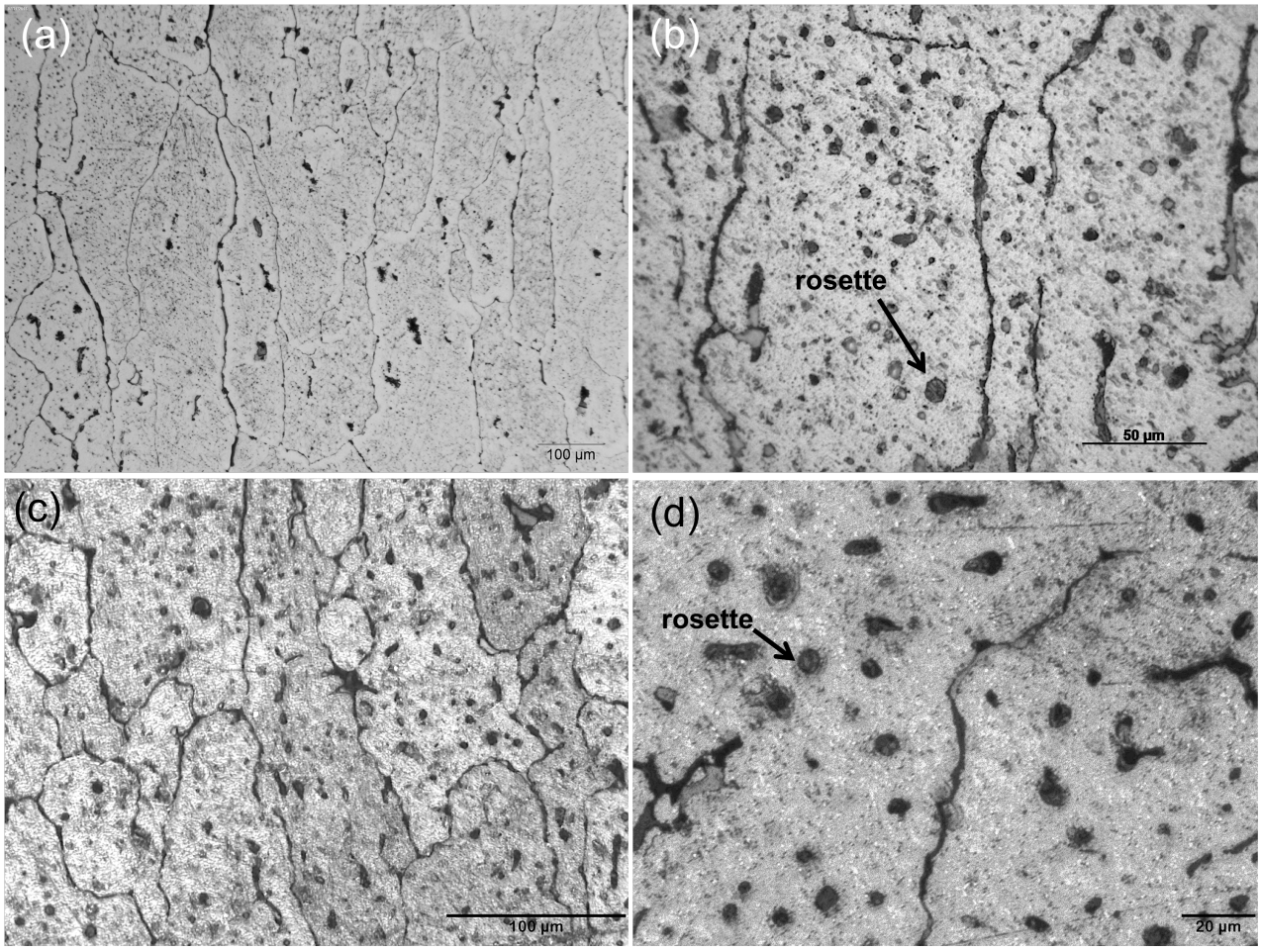

Fig. 4.4. Micrograph of broom-straw microstructure observed on sample BhA-T: (a) 100X (b) 500X and sample BhC-T: (c) 250X (d) 500X; etched with Keller's reagent.

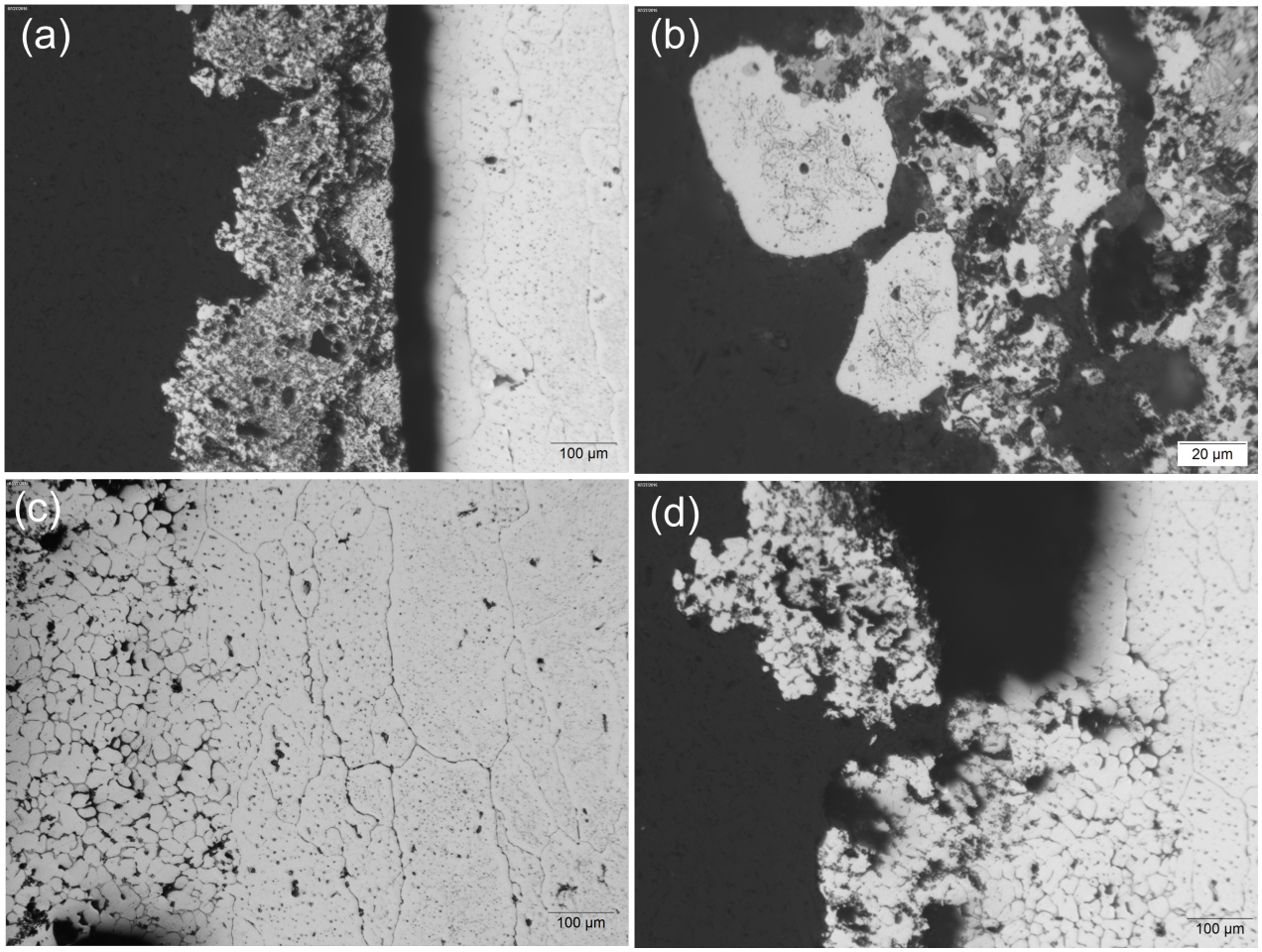

Fig. 4.5. Light optical micrograph of sample BhA-T: deposition on backside surface of bulkhead (b) microstructure adjacent to deposition; etched with Keller's reagent, 1000X.

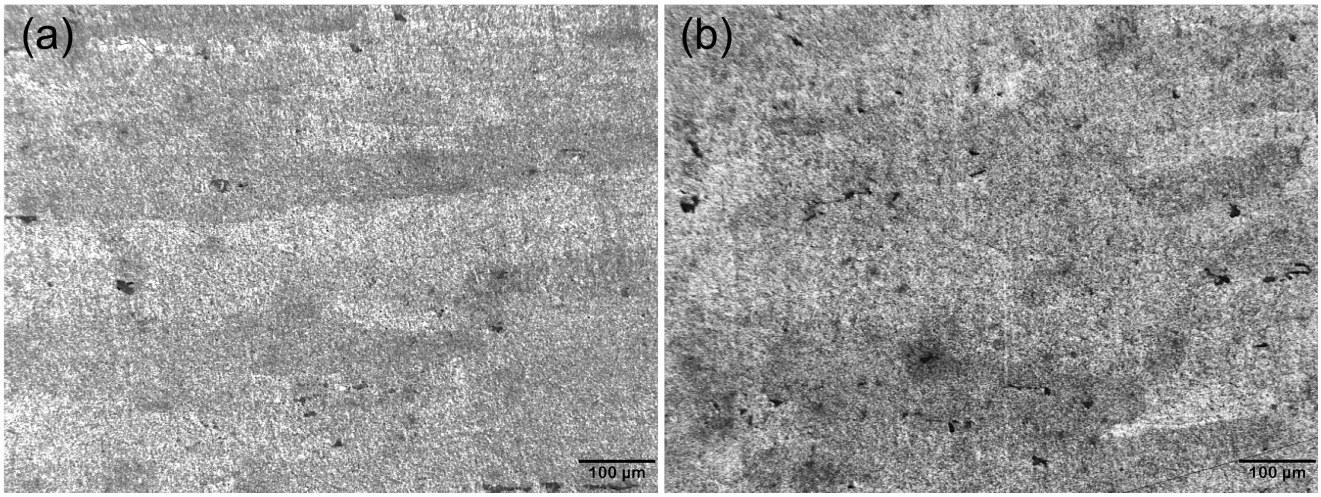

Fig. 4.6. Micrograph of samples located away from fracture: (a) BhB-L and (b) BhB-T; etched with Keller's reagent, 100X.

Elemental analysis using EDS revealed liquated precipitates of the grain boundary to be aluminum-, copper- and magnesium-rich, (Fig. 4.7a-d) likely corresponding to the primary strengthening precipitates, Al_2CuMg (*S* phase), which is spherical and evenly distributed within the matrix upon aging and tends to form at grain boundaries during elevated aging temperatures.

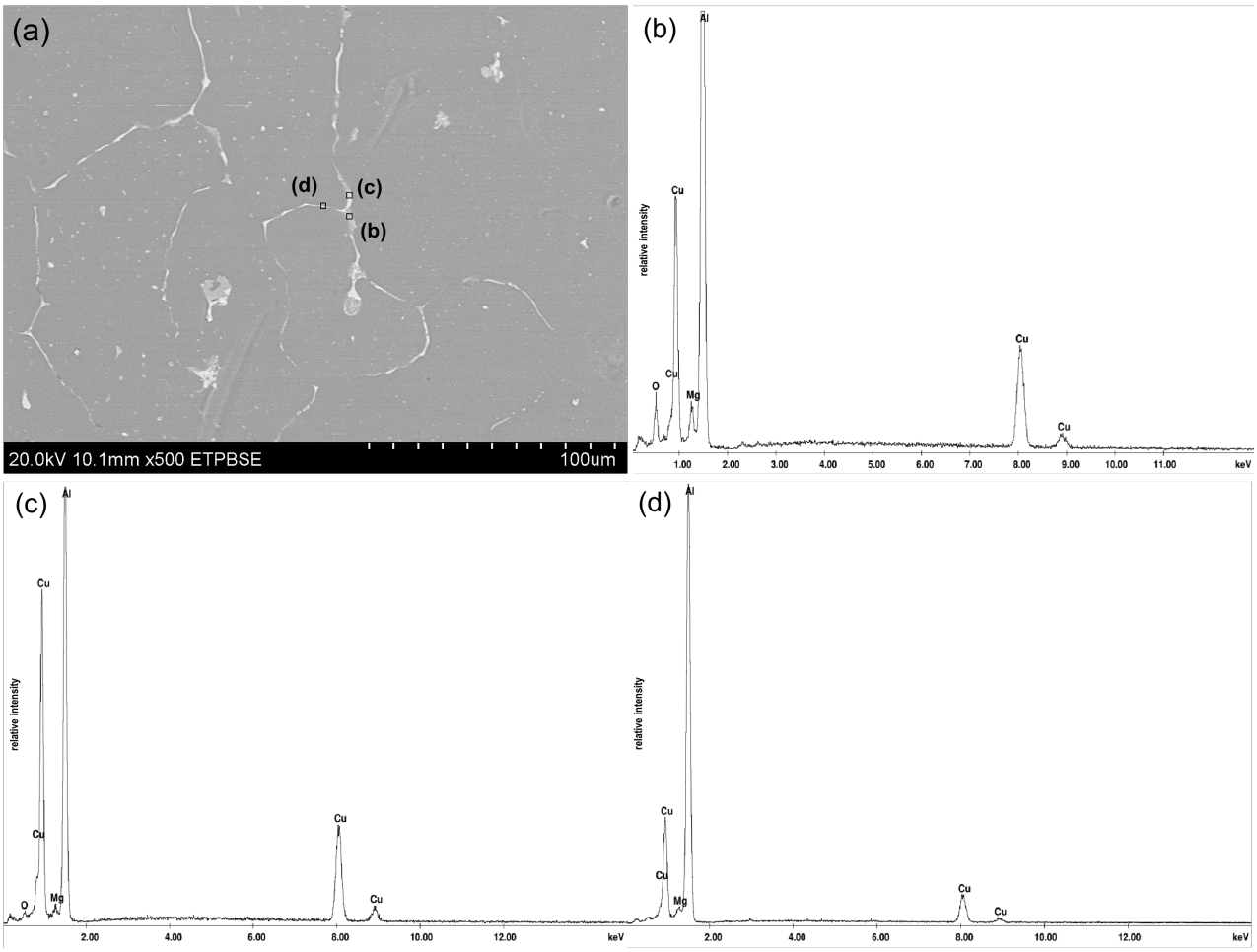

Fig. 4.7. (a) Backscatter electron micrograph of liquated grain boundaries observed at broom-straw fracture (BhA-T) with EDS analysis regions outlined in black boxes (b)-(d) EDS spectrum of associated regions outlined in (a).

The coarse, irregular-shaped gray and white precipitates were primarily composed of iron, manganese and silicon, illustrated in Fig. 4.8-Fig. 4.13; the morphology and elemental composition suggests the iron-rich particles to be

Al_7Cu_2Fe or $(MnFe)_3SiAl_{12}$ and the manganese-rich precipitates can be reasonably identified as Al_{20} Mn_3Cu_2, Fig. 4.12(e) and (f). Iron- manganese- and silicon-containing particles are understood to form during the solidification process (i.e. casting) and remain undissolved upon SHT.

Micro x-ray analysis of the spray-like deposition, displayed in Fig. 4.14a-f, revealed aluminum, magnesium, copper and iron intensity peaks that likely correspond to AA 2024. Titanium, vanadium, and chromium were also detected and may be the presence of Ti-6Al-4V from the PLBD roller components. Calcium, chlorine, and silicon concentration could be contamination from flow through the debris field during orbiter breakup or from ground impact. The presence of oxygen was also detected throughout the surface deposition.

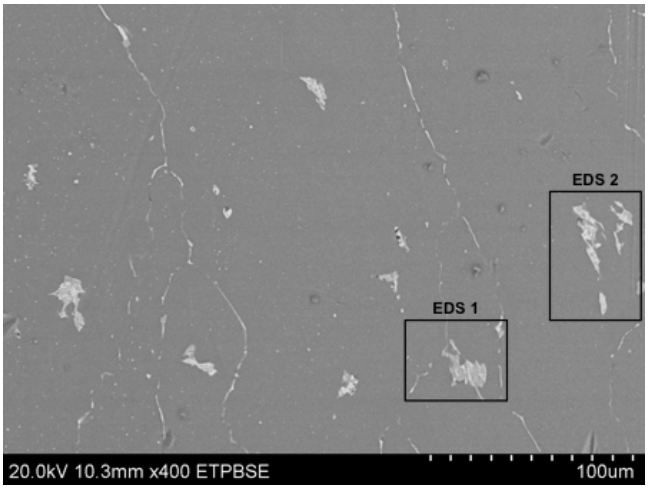

Fig. 4.8. Backscatter electron micrograph of BhA-T; EDS analysis was performed on precipitates outlined in black.

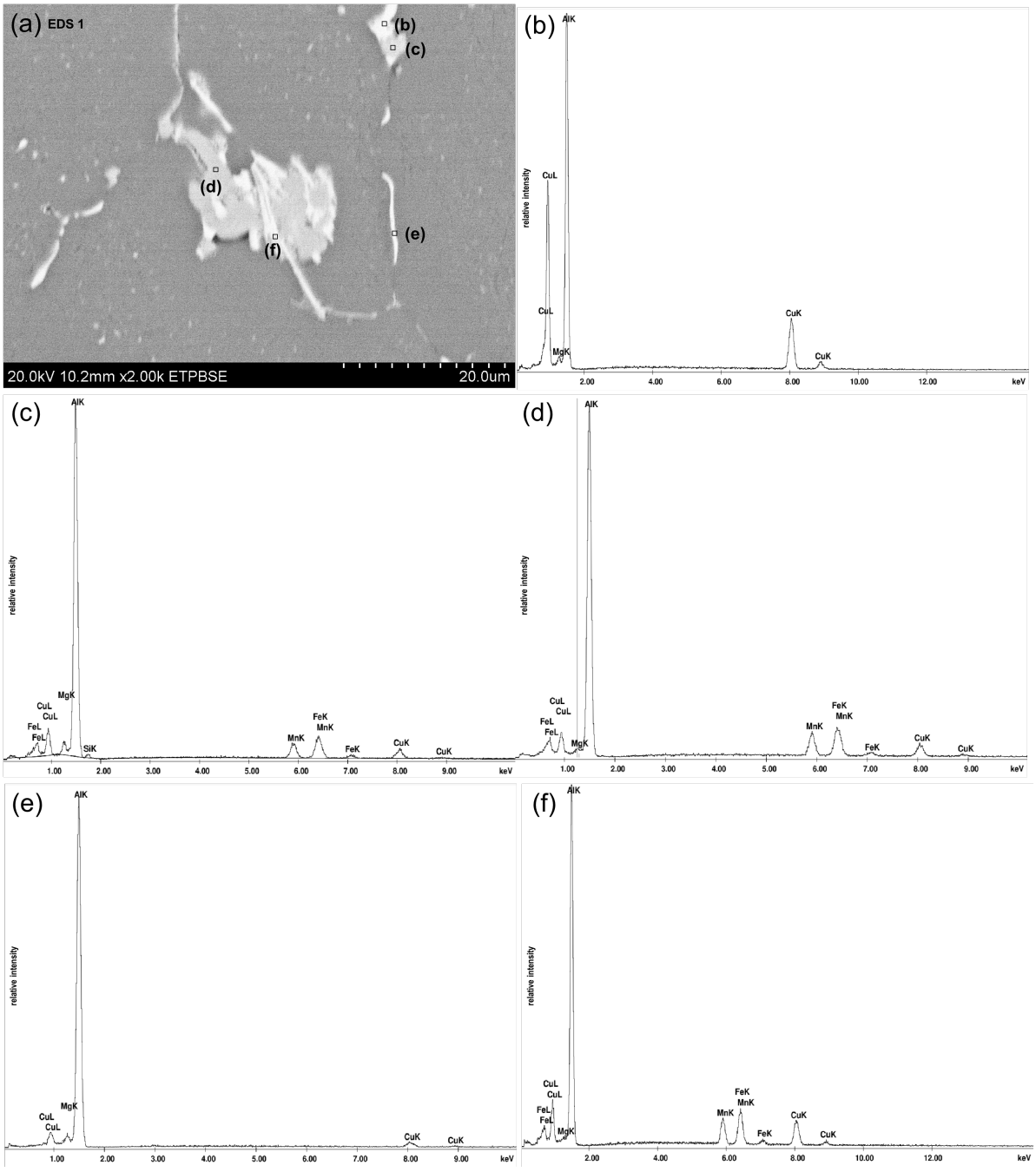

Fig. 4.9. (a) Backscatter electron micrograph of coarse, irregular precipitate observed at broom-straw fracture (BhA-T); (b)-(f) EDS spectrum of corresponding regions outline in (a).

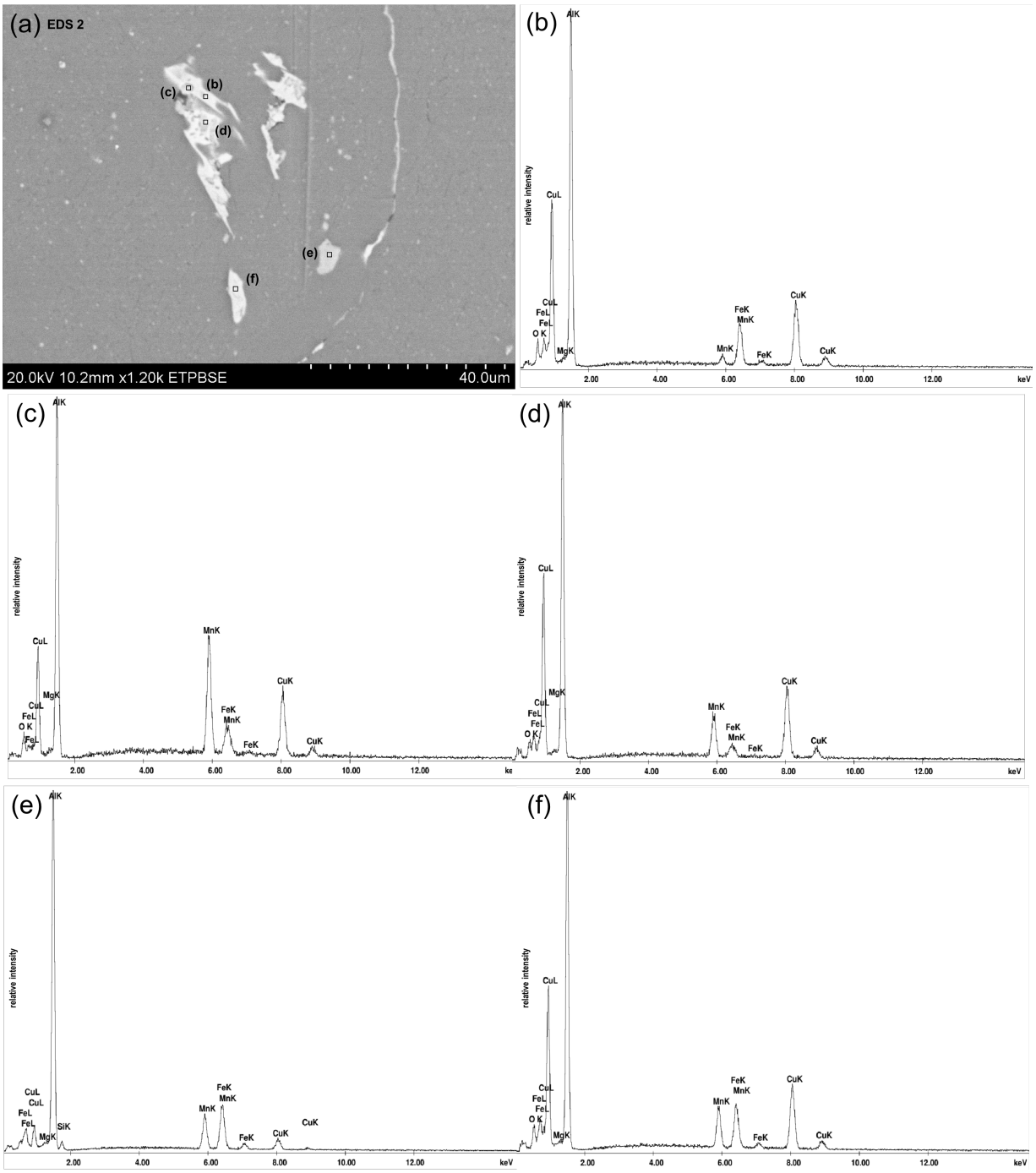

Fig. 4.10. (a) Backscatter electron micrograph of coarse, irregular precipitates and liquated grain boundaries observed at broom-straw fracture (BhA-T); (b)-(f) EDS spectrum of corresponding regions outline in (a).

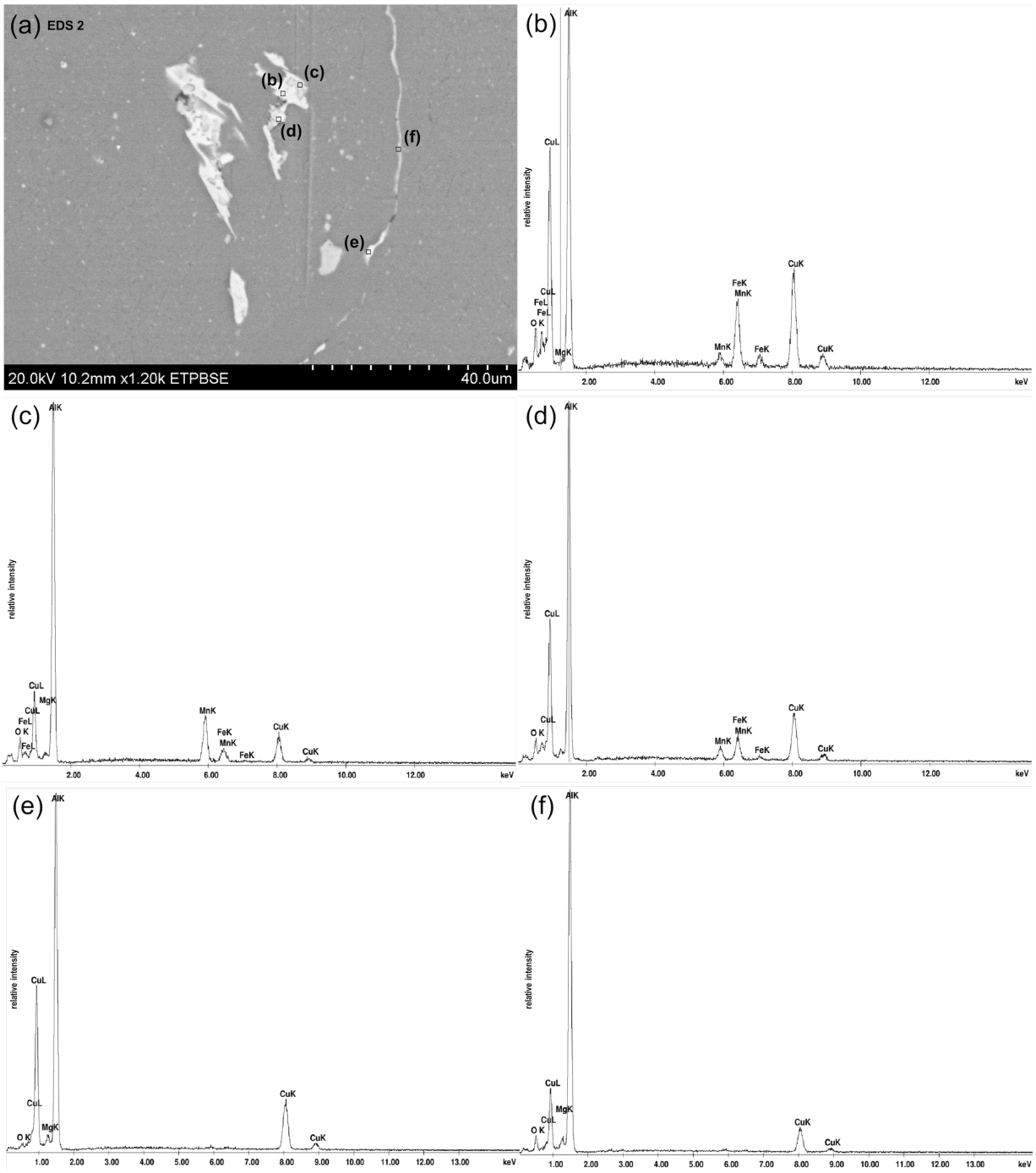

Fig. 4.11. (a) Backscatter electron micrograph of coarse, irregular precipitates and liquated grain boundaries observed at broom-straw fracture (BhA-T); (b)-(f) EDS spectrum of corresponding regions outline in (a).

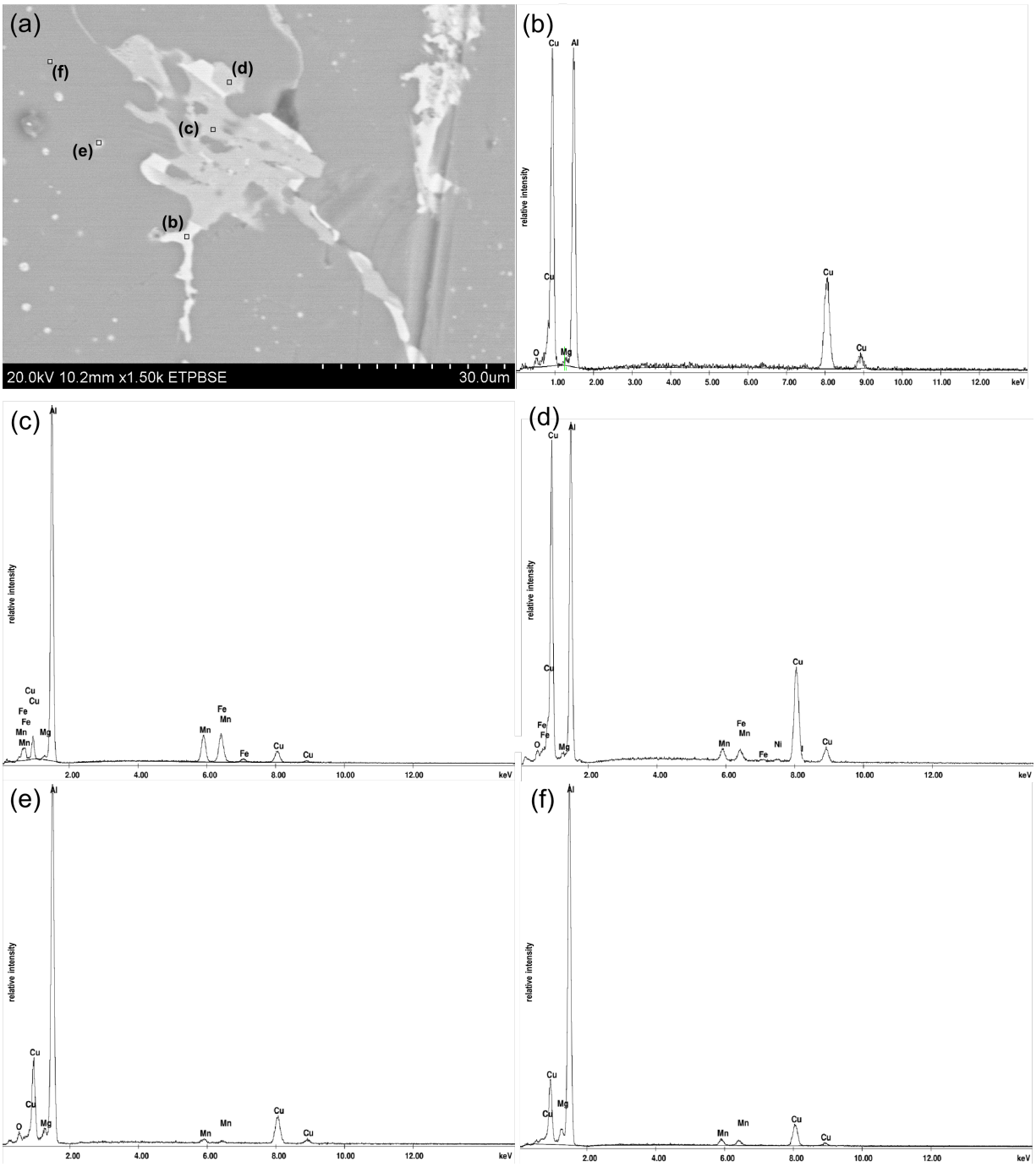

Fig. 4.12. (a) Backscatter electron micrograph of coarse, irregular precipitates and liquated grain boundaries observed at broom-straw fracture (BhA-T); (b)-(f) EDS spectrum of corresponding regions outline in (a).

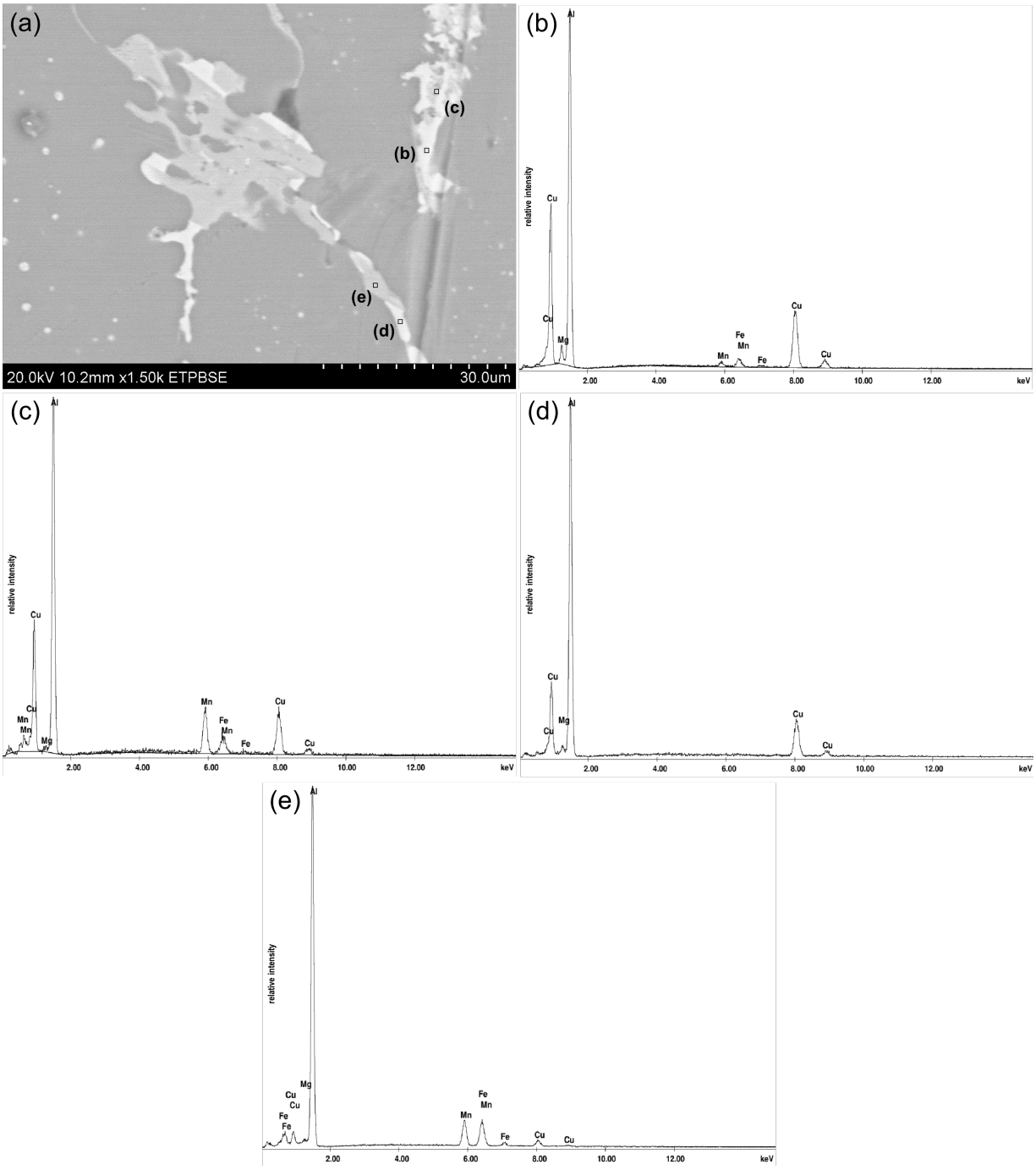

Fig. 4.13. (a) Backscatter electron micrograph of coarse, irregular precipitates and liquated grain boundaries observed at broom-straw fracture (BhA-T); (b)-(f) EDS spectrum of corresponding regions outline in (a).

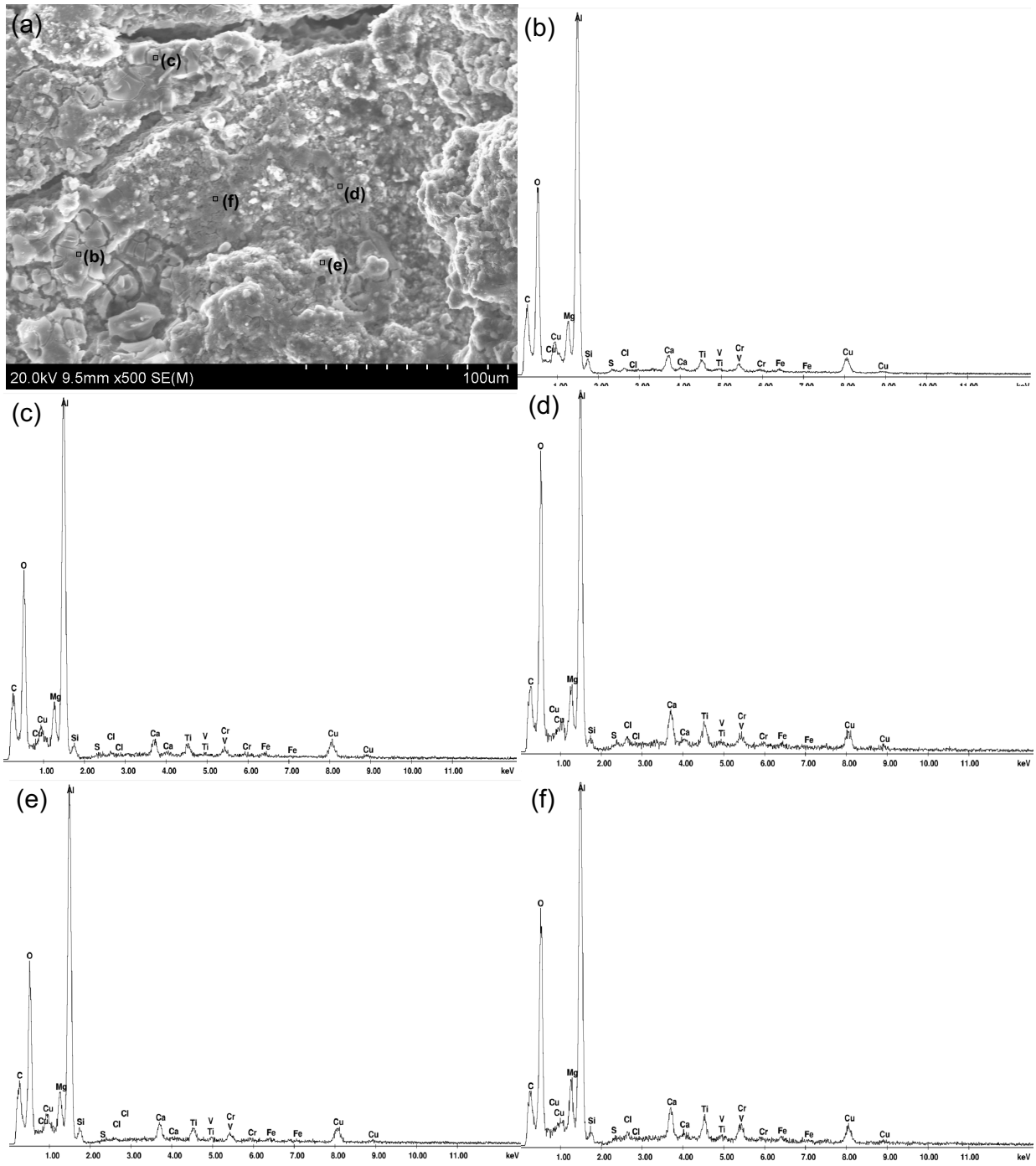

Fig. 4.14. (a) Backscatter electron micrograph of deposition located on backside of bulkhead; (b)-(f) EDS spectrum of associated regions outlined in (a).

4.3. Discussion

The broom-straw feature appeared to be the result prevalent intergranular voids and cracks cracking due to liquid flow, attributing to a fibrous, delaminated structure. As shown in Fig. 4.2, a single fiber or broom-straw at the fracture surface may be thought of simplistically, as an individual grain that is "sticking out" due the lack of the surrounding grain boundary that would ordinarily yield a solid bulk structure of contiguous grains.

Failure occurring in a region absent of grain boundary liquation would follow more classic mechanisms, exhibiting fracture surface characteristics consistent with ductile (dull appearance, microscopic dimples), brittle (shiny surface, microscopic cleavage steps), or fatigue (radial marks, beach marks, catastrophic rupture features) modes of failure.

The presence of liquated grain boundaries suggests heating to and above 500 ˚C (932 ˚F), the temperature at which incipient melting occurs. The intergranular void formation can be reasonably attributed to the grain boundary precipitation transforming from solid to liquid. Assuming fracture occurred subsequent to grain boundary liquation, a free surface introduced within the bulk by fracture, may have provided a path for grain boundary liquid to flow out of the bulk, rendering the grain boundary between grains a void space.

Eutectic melting is further substantiated by the presence of rosette structures, the typical morphology of the eutectic phase for AA 2024, *S* phase, which forms cooling of the grain boundary melt occurs before the opportunity

for the eutectic phase to re-equilibrate into the matrix [10, 76]. Grain boundary precipitation occurs at elevated temperatures and is often accompanied by a PFZ as copper is depleted from the matrix to form the *S* phase.

The elongated microstructure observed at the fracture surface, and away from fracture, provides insight into the possible forming process of the bulkhead. A forming process, such as cold-rolling, produces an elongated grain structure with constituent segregation aligning parallel to the rolling direction. It is likely that grain boundary precipitation and subsequent liquation occurred in a preferential orientation aligned with the forming direction.

This observation is in good agreement with the results reported by Smith et. al., whom examined *Columbia* debris items composed of 2XXX and 7XXX series aluminum. Inverse pole figures generated for the debris revealed crack propagation along high angle grain boundaries with a relative mis-orientation greater than 15° for all samples while cracking was not observed at sub-grain boundaries. Adjacent to areas of prevalent intergranular cracking, the grain boundaries contained heavy precipitation.

Luo found a strong correlation between high angle grain boundaries and intergranular corrosion for 2XXX aluminum alloys. It is well known that grain boundaries serve as preferential sites for precipitation, and high angle grain boundary density increases upon deformation processes so there may exist a link between mis-orientation and broom-straw behavior.

It should also be noted that Smith observed increased intergranular precipitation in fracture areas for AA2124[2]-851 versus AA2124-351, which researchers attributed to exposure to higher temperatures or extended heating duration. This observation may also be attributed to the difference in thermo-mechanical processing between the two samples as it is well understood that -T3 provides better resistance to intergranular corrosion than -T8.

Although oxygen was detected on the surface of the deposition seen on the backside of the bulkhead, along with elements consistent with the Ti-6Al-4V alloys, further examination is required to adequately identify the composition and nature of the deposition in order to compare to the char layer deposit observed on overhead windows.

4.4. Conclusions

Delaminated fracture surfaces, termed broom-straw fracture, were observed on sections of the X_o 582 ring-frame bulkhead arch recovered from Space Shuttle *Columbia*, believed to occur upon incipient melting at grain boundaries. This investigation attempts to further elucidate the phenomenon, as

---

[2] AA2124 is the high purity form of AA2024, containing lower concentrations of Si and Fe

broom-straw fracture not been fully described or referenced in metallurgy literature at the time of this writing.

Characterized by fractography, microscopy and x-ray micro-analysis, liquation of grain boundaries was evident and was accompanied with intergranular cracking, likely the cause of void coalescence. The microstructure consisted of an α-Al matrix of fine, unevenly distributed, spherical precipitates, *S* phase, as well as coarse, irregular-shaped particles, Al-Cu-Fe-Mn particles. Liquated *S* phase particles were identified by EDS, pointing to eutectic melting.

Broom-straw fracture was observed to be the result of impact occurring in a region of prevalent grain boundary eutectic liquation. Although conclusions may not be reasonably drawn given small sample size and unknown re-entry conditions during the time of failure for all debris, the influence of thermo-mechanical processing and impurities on the susceptibility of broom-straw fracture for 2XXX series should be further investigated. A probe into broom-straw fracture occurrence for other aluminum allows to understand the influence of initial microstructure, and impact behavior.

Chapter 5

Future Work

- Further analysis of the aluminum oxide deposition of the bulkhead is necessary to assess similarities to aluminum oxide of the char layer deposition.
- Forensic examination of starboard PLBD latch roller that exhibits similar thermal damage to evaluate similarities to the port lath roller.
- Electron microprobe analysis (EMPA) to further identify phase transformations within titanium.
- Impact testing of 2XXX and 7XXX series aluminum in over-aged, semi-molten conditions to further understand the broom-straw fracture mechanism and the microstructural features and thermo-mechanical processing that may contribute to the phenomenon.

References

[1] National Aeronatics and Space Administration, "Columbia Crew Survival Investigation Report NASA/SP-2008-565," 2008.

[2] American Society for Metals International Technical Book Committee, Elements of Metallurgy and Engineering Alloys, F. C. Campbell, Ed., ASM International, 2008.

[3] American Society for Metals, ASM International. Handbook Committee, "Vol. 2: Properites & Selection: Nonferrous Alloys and Special Purpose Materials," in *ASM Handbook, 10th edition*, 10th edition ed., ASM International, 1990.

[4] F. C. Campbell, Elements of Metallurgy and Engineering Alloys, Materials Park: ASM International, 2008.

[5] R. Pederson, "Microstructure and Phase Transformation of Ti-6Al-4V, Doctoral Thesis, Lulea," Lulea University of Technology, 2002.

[6] L. M. Gammon, R. D. Briggs, J. M. Packard, K. W. Batson, R. Boyer and C. W. Domby, "ASM Handbook, Volume 9: Metallography and Microstructures," in *Metallography and Microstructures of Titanium and Its Alloys*, ASM International, 2004, pp. 899-917.

[7] American Society for Metals, ASM International. Handbook Committee, "Vol. 3: Alloy Phase Diagrams," in *ASM Handbook, 10th edition*, Metals Park, American Society for Metals, 1992.

[8] R. F. Muraca and J. S. Whittick, "Materials Data Handbook on Inconel 718," NASA Marshall Space Flight Center, Huntsville, 1973.

[9] W. L. Fink, F. Keller, W. E. Sicha, J. A. Nock Jr. and E. J. Dix Jr., Physical Metallurgy of Aluminum Alloys: A series of 5 Educational Lectures on Physical Metallurgy of Aluminum Alloys Presented to Members of the A.S.M. During the 28th National Congress & Exposition, Atlantic City, Cleveland: American Society for Metals, 1949.

[10] J. E. Hatch, Aluminum properties and physical metallurgy, ASM International, 1984.

[11] J. Olivas, M. Wright, R. Christoffersen, D. Cone and S. McDaniels, "Crystallographic oxide phase identification or char deposits obtained from space shuttle Columbia window debris.," *Acta Astronautica,* vol. 67, pp. 553-560.

[12] J. Olivas, B. Mayeaux, D. Cone and P. Melroy, "Material Behavior of Titanium in Space Entry Environments," in *3rd AIAA Atmospheric Space Environmetns Conference*, Honolulu, 2011.

[13] National Transportation Safety Board, "Aircraft Accident Brief LAX01MA272," Washington D.C., 2004.

[14] J. M. Kuchta and R. G. Clodfelter, "Aircraft mishap fire investigations, AFWAL-TR-85-2057, AD-A161 094," AF Wright Aeronautical Laboratories, Wright-Patterson AFB, 1985.

[15] C. R. Morin, R. P. O'Shea, W. Holmes and R. Schaeffer, "Techniques and procedures for structural and material aircraft failure investigation," Engineering Systems, Inc, Aurora, 1991.

[16] S. W. Smith, R. S. Piascik, R. E. Crooks and R. N. Snenoy, "Destructive Examinations of Aluminum Alloy Debris Items," NASA - Langley Research Center Metals and Thermal Structures Branch, Langley, 2003.

[17] M. Kampner, R. M. Deacon and A. R. Marder, "Failure analysis of an aluminum sandwich panel skin from the space shuttle columbia," *Journal of Failure Analysis and Prevention,* vol. 6, no. 1, pp. 46-50, 2006.

[18] I. Lam, L. Brundage, L. Velcheck, R. M. Deacon and A. R. Marder, "Failure analysis of aluminum structural members on the space shuttle Columbia," *Journal of Failure Analysis and Prevention,* vol. 6, no. 1, pp. 32-38, 2006.

[19] H. Guleryuz and H. Cimenoglu, "Oxidation of Ti-6Al-4V alloy," *Journal of Alloys and Compounds,* vol. 472, pp. 241-246, 2009.

[20] P. Kofstad, "High-temperature Oxidation of Titanium," *Journal of Less Common Metals,* vol. 12, no. 6, pp. 449-464, 1967.

[21] P. Kofstad, P. B. Anderson and O. J. Krudtaa, "Oxidation of titanium in the temperature range 800-1200˚C," *Journal of Less Common Metals,* vol. 3, no. 2, pp. 89-97, 1961.

[22] J. Stringer, "Some observation on the kinetics of oxidatioon of titanium at high temperatures," *Journal of the Less Common Metals,* vol. 6, pp. 207-213, 1964.

[23] J. Stringer, "The effect of pressure on the 2nd stage parabolic rate in the oxidation of titanium," *Acta Metallurgica,* vol. 8, pp. 810-811, 1960.

[24] A. E. Jenkins, "The oxidation of titanium at high temperatures in an atmosphere of pure oxygen," *Journal of the Institute of Metals,* vol. 82, pp. 213-221, 1954.

[25] M. H. Davies and C. E. Birchenall, "Oxidation of Titanium," *Journal of Metals (N.Y.)* , vol. 3, 1951.

[26] I. Vaquila, L. I. Vergara, A. C. G. Passeggi Jr., R. A. Vidal and J. Ferron, "Chemical reactions at surfaces: titanium oxidation," *Surface and Coatings Technology,* vol. 122, pp. 67-71, 1999.

[27] A. Biswas and J. Majumdar, "Surface characterization and mechanical property evaluation of thermal oxidized Ti-6Al-4V," *Materials Characterization,* vol. 60, pp. 513-518, 2009.

[28] S. Frangini and A. Mignone, "Various aspects of the air oxidation behaviour of Ti6Al4V alloy at temperatures int he range 600-700C," *Journal of Material Science,* vol. 29, pp. 714-720, 1994.

[29] B. Sefer, R. Gaddam, R. Pederson, A. Mateo and M. L. Antti, "Characterization of the oxide scale and alpha-case layer in Ti-6Al-4V and Ti-6Al-2Sn-4Zr-2Mo in the temperature range 500-700 C".

[30] H. L. Du, P. K. Datta, D. B. Lewis and J. S. Burnel-Gray, "Air oxidation behaviour of Ti-6Al-4V alloy between 650 and 850 C," *Corrosion Science,* vol. 63, pp. 631-642, 1994.

[31] F. Pitt and M. Ramulu, "Influence of grain size and microstructure on oxidation rates in titanium alloy Ti-6Al-4V under superplastic forming conditions," *Journal of Material Engineering and Performance,* vol. 13, no. 6, pp. 727-734, 2004.

[32] D. B. Lee, I. Pohrelyuk, O. Yaskiv and J. C. Lee, "Gas Nitriding and subsequent oxidation of Ti-6Al-4V alloys," *Nanoscale Research Letter,* vol. 7, no. 21, pp. 1-5, 2012.

[33] J. R. Cuthill, W. D. Hayes and R. E. Seebold, "Nitriding Phenomena in Titanium and the 6Al-4V Titanium Alloy," *Journal of Research of the*

National Bureau of Standards - A. Physics and Chemistry, vol. 64A, no. 1, pp. 119-125, 1959.

[34] E. L. Dreizin, "Phase changes in Metal Combustion," *Progress in Energy and Combustion Science,* vol. 26, pp. 57-78, 2000.

[35] S. Deevi and Z. A. Munir, "The mechanism of synthesis of titanium nitride by self-sustaining reactions," *Journal of Res,* vol. 5, no. 10, pp. 2177-2183, 1990.

[36] R. Montanari, G. Constajnza, M. E. Tata and C. Testani, "Lattice expansion of Ti-6Al-4V by nitrogen and oxygen absorption," *Materials Characterization,* vol. 59, no. 3, pp. 334-337, 2008.

[37] A. V. Grosse and J. B. Conway, "Combustion of metals in oxygen," *Industrial and Engineering Chemistry ,* vol. 50, no. 4, pp. 663-672, 1958.

[38] M. Branch and A. Abbud-Madrid, "A study of ignition phenomena of bulk metals by radiant heating," in *The Second International Microgravity Combustion Workshop*, Lewis Research Center, Cleveland, 1993.

[39] G. Markstein, "Combustion of Metals," *AIAA Journal,* vol. 1, no. 3, pp. 550-562, 1963.

[40] W. A. Riehl, C. F. Key and J. B. Gayle, "Reactivity of Titanium with Oxygen," in *National Meeting of Society of Materials and Process Engineers*, Los Angeles, 1962.

[41] R. T. Strobridge, J. C. Moulder and A. F. Clark, "Titanium Combustion in Turbine Engines, FAA-RD-79-51, NBSIR 79-1616," U.S. Department of Transportation Federal Aviation Administration Research and Development, Washington, D.C., 1979.

[42] A. H. Tench, H. M. Roder and A. F. Clark, "Combustion of metals in oxygen, Phase II: Bulk burning experiments, NBSIR 73-345," NASA Marshall Space Flight Center, National Bureau of Standards, Huntsville, 1973.

[43] J. S. Wolf and J. M. Grochowski, "Nature of Gas-metal reactions under conditions of anisothermal oxidation," in *Stress effect and the oxidation of metals*, TMS-AIME, 1975, p. 274.

[44] J. S. Wolf, "Exploratory development on oxidation beha vior of titanium alloys under high heating rates, AFML TR-74-265," Air Force MAterials Laboratory, Wright Patterson AFB, Ohio, 1975.

[45] J. S. Wolf, "Anisothermal oxidiation of titanium and its alloys, AFASR-76-2919," Clemson University, Clemson, 1977.

[46] J. S. Wolf, D. D. Moyle, A. B. Pruitt and J. H. Bader, "Anisothermal oxidation of titanium: Initial reactivity and igntion," in *Preceeding of the Symposium on Properties of High Temperature Alloys*, 1976.

[47] P. R. Hill, D. Adamson, D. H. Foland and W. E. Bressette, "High-Temperature Oxidation and Ignition of Metals, RM L55L23b," National Advisory Committee for Aeronautics, Langley Field, 1956.

[48] V. I. Rozenband and N. I. Vaganova, "A strength model of heterogenous ignition of metal particles," *Combustion and Flame,* vol. 88, no. 1, pp. 113-118, 1992.

[49] T. A. Andrzejak, E. Shafirovich and A. Varma, "On the mechanisms of Titanium Particle reactions in O2/N2 and O2/Ar Atmospheres," *Propellants, Explosives, Pyrotechnics,* vol. 34, no. 1, 2008.

[50] F. Littman, F. Church and E. Kinderman, "A study of metal ignitions: the spontaneous igntion of titanium," *Journal of Less Common Metals,* vol. 3, pp. 367-378, 1961.

[51] E. A. Borisova and K. V. Bardanov, "Ignition of Titanium in Media Containing Oxygen," *Metallovedenie i Termicheskaya Obrabotka Metallov,* vol. 2, pp. 37-40, 1963.

[52] A. Abbud-Madrid, M. C. Branch and J. W. Daily, "Ignition and Combustion of Bulk Metals, Under Elevated, Normal and Reduced Gravity Conditions, N96-15552-03-29," in *3rd International Microgravity Combustion Workshop*, Cleveland, 1995.

[53] A. Abbud-Madrid, G. J. Fiechtner, M. C. Branch and J. W. Daily, "Ignition and Combustion Characteristics of Pure Bulk Metals: Normal Gravity Test

Results, NASA-CR-202S89," in *32nd Aerospace Sciences Meetign and Exhibit*, Reno, 1994.

[54] V. I. Bolobov, "Mechanism of Self-Ignition of Titanium Alloys in Oxygen," *Combustuion, Explosion, and Shock Waves,* vol. 38, no. 6, pp. 639-645, 2002.

[55] V. I. Bolobov, "Mechanism of Metal Ignition in an Oxygen Flow," *Combustion, Explosion, and Shock Waves,* vol. 34, no. 1, pp. 44-50, 1998.

[56] P. L. Harrison, "The combustion of titanium and zirconium," *Special Fuels,* pp. 913-918.

[57] V. Tanguay, P. Batchelor, E. Ramzi and A. Higgins, "Metal Combustion in High-Speed FLow," in *43rd Aeropsace Sciences Meeting*, Reno, 2005.

[58] A. J. Higgins, D. L. Frost, C. Knowlen, F. Zhang and S. B. Murray, "Combustion of Supesonic Metallic Spheres," in *18th International Colloquium on the Dynamics of Explosions and Reactive Systems*, Seattle, 2001.

[59] D. A. Gordon, "Combustion Characteristics of Metal Particles," in *Solid Propellant Rocket Research*, New York, Academic Press, 1960, pp. 271-278.

[60] I. E. Molodetsky, E. Vicenzi, E. L. Dreizin and C. K. Law, "Phases of Titanium Combustion in Air," *Combustion and Flame,* vol. 112, pp. 522-532, 1998.

[61] A. Devito, "The combustion of bulk metals in a high speed flow, M.E. thesis," McGill University, Montreal, 2014.

[62] V. G. Anderson and B. A. Manty, "Titanium alloys igntion and combustion, NADC76083-30," Department of the Navy, Warminster, 1977.

[63] ASM Handbook Committee, "Atlas of Microstructures of Industrial Alloys," in *Metals Handbook*, 8th ed., vol. 7, T. Lyman, Ed., Metals Park, Ohio: American Society for Metals, 1972.

[64] M. Diamanti, B. Curto and M. Pedeferri, "Interference Colors of Thin Oxide Layers on Titanium," *Color Research and Application,* vol. 33, no. 3, p. 221, 2008.

[65] D. Velten, V. Biehl, F. Aubertin, B. Valeske, W. Possart and J. Breme, "Preparation of TiO2 Layers on cp-Ti and Ti6Al4V by Thermal and Anodic Oxidation and by Sol-Gel Coating Techniques and Their Characterization.," *J. Biomedic. Mater. Res. ,* vol. 59, pp. 18-28, 2002.

[66] T. R. Strobridge, J. C. Moulder and A. F. Clark, "Titanium combustion in turbine engines FAA-RD-79-51," Federal Aviation Administration, Washington D.C., 1979.

[67] R. Gaddam, B. Sefer, R. Pederson and M. L. Antti, "Study of alpha case depth in Ti-6Al-2Sn-4Zr-2Mo and Ti-6Al-4V," in *IOP conference Series: Materials Science and Engineering*, 2013.

[68] H. Miura, Y. Itoh, T. Ueamtsu and K. Sato, "The influence of density and oxygen content on the mechanical properties of injection molded Ti-6Al-4V alloys," *Advances in Powder Metallurgy and Particulate Materials,* vol. 1, pp. 46-53, 2010.

[69] B. Sefer, Oxidation and Alpha Case Phenomenoa in Titanium Alloys used in Aerospace Industry: Ti-6Al-2Sn-4Zr-2Mo and Ti-6Al-4V, M.S. Thesis, Lulea: Lulea University of Technology, 2014.

[70] F. H. Froes, Titanium: Physical Metallurgy, Processing, and Applications, First Edition, Materials Park: ASM International, 2015.

[71] H. D. Kessler, W. Rostoker and R. J. Van Thyne, "Titanium Phase Diagrams, WADC Technical Report 52-335," Wright Air Development Center, Materials Laboratory, Wright-Patterson Air Force Base, 1953.

[72] D.-G. Lee, S. Lee and Y. Lee, "Effect of precipitates on damping capacity and mechanical properties of Ti-6Al-4V alloy," *Materials Science and Engineering A ,* vol. 486 , pp. 19-26, 2008.

[73] D.-G. Lee, S. Lee and Lee, "Effects of nano-sized α2 particles on quasi-static and dynamic deformation behavior of Ti-6Al-4V alloy with bimodal structure," *Journal of Materials Science ,* vol. 40, no. 15 , pp. 4077-4084, 2005.

[74] L. M. Wang, H. C. Lin and C. J. Tsai, "Characterization and Mechanism of α2-Ti3Al and γ-TiAl precipiation in Ti-6Al-4V Alloy following Tungsten Arc Welding," *Key Engineering Materials,* vol. 520, pp. 320-329, 2012.

[75] J. L. Buckner, S. W. Stafford, D. M. Cone and J. D. Olivas, "Investigation of Ti-6Al-4V alloy response to atmospheric re-entry exposure; in Proceedings of the 8th IAASS Conference," in *International Associaiton for the Advancement of Space Safety*, Melbourne, 2016.

[76] D. T. Alexander and A. L. Greer, "Formation of eutectic intermetallic rosettes by entrapment of liquid droplets during cellular columnar growth," *Acta Materialia,* vol. 52, no. 20, pp. 5853-5861, 2004.

[77] R. Wood and R. Sweginnis, Aircraft Accident Investigation, Endeavor Books, 2006.

[78] J. Olivas, B. Mayeaux, D. Cone and P. Melroy, "Material Behavior of Titanium in Space Entry Environments," in *3rd AIAA Atmospheric Space Environments Conference*, Honolulu, 2011.

[79] J. Olivas, B. Mayeaux, D. Cone, P. Melroy and W. Rochelle, "Material Behavior of Titanium in Space Entry Environements," *American Institute of Aeronautics and Astronautics.*

[80] G. Lutjering and J. Williams, Titanium, Berlin: Springer, 2003.

[81] W. Harwood, " “The Fate of Challenger’s Crew.” http://www.space-shuttle.com/ challenger1.htm".

[82] C. Coddet, A. Chaze and G. Beranger, "Measurements of the adhesion of thermal oxide fils: application to the oxidation of titanium," *Journal of Materials Science,* vol. 22, pp. 2969-2974, 1987.

[83] R. Boyer, "Titanium for aerospace: rationale and applications," *Advanced Performace Materials,* vol. 2, no. 4, pp. 349-368, 1995.

[84] "Effects of Hypersonic Flow during Reentry of the Space Shuttle. http://www.columbiassacrifice.com/index.html".

[85] W. C. Rochelle, "Survey of Titanium Testing at NASA, DOE and DOD Facilies," ESCG-4380-06-AFD-MEMO-0011, 2006.

[86] I. Glassman, A. M. Mellor, H. F. Sullivan and N. M. Laurendeau, "A review of Metal Ignition and Flame Models," in *Propulsion and Energetics Panel, 34th Meeting, 8th Colloquium*, Wright-Patterson AFB, 1969.

[87] P. Batchelor and A. J. Higgins, "Ignition of Reactive Metal Particles in Supersonic Flow," in *Combustion Institute/Canadian Section Spring Technical Meeting*, Kingston, 2004.

[88] I. Lam, G. Ganot, D. Brundage, L. Velcheck, R. M. Deacon and A. R. Marder, "Failure Analysis of Aluminum Structural Members on the Space Shuttle Columbia," *Journal of Failure Analysis and Prevention,* vol. 6, no. 1, pp. 32-38, 2006.

[89] D. A. Stewart, "Temperature control coatings, Paper No. 247-A," in *10th NASP Techonolgy Symposium*, Monterey, 1991.

[90] The Metallurgical Society of AIME Proceedings, "Titanium and Titanium Alloys," in *Internation Conference on Titanium*, Moscow State University, 1976.

[91] ASM Handbook Committee, "Vol. 7: Atlas of Microstructures of Industrial Alloys," in *Metals Handbook, 8th edition*, 8th ed., vol. 7, T. Lyman, Ed., Metals Park, Ohio: American Society for Metals, 1972.

[92] G. Lutjering, "Influence of processing on microstructure and mechanical properties of alpha beta titanium alloys," *Materials Science and Engineering,* vol. A243, pp. 32-45, 1998.

[93] W. C. Reynolds, "Investigation of Ignition Temperatures of Solid Metals; NASA TN D-182," 1959.

[94] Z. Liu and G. Welsch, "Literature survey on diffusivites of oxygen, aluminum, and vanadium in alpha titanium, beta titanium, and in rutile," *Metallurgical Transactions A,* vol. 19A, pp. 1121-1125, 1988.

[95] P. K. Hauffe and H. Kjollesdal, "Investigation on the Oxidation Mechanism of Titanium," *Acta Chemica Scandinavica ,* vol. 12, no. 2, pp. 239-266, 1958.

[96] T. Smith, "Oxidation of titanium between 25 ˚C and 400 ˚C," *Surface Science ,* vol. 38, no. 2, pp. 292-312, 1973 .

[97] T. Hurlen, "Oxidation of titanium," *Journal of the Institute of Metals,* vol. 89, pp. 128-136, 1960.

[98] E. A. Gulbransen and K. F. Andrew, "Kinetics of the reactions of titanium with O2, N2 and H2," *Transactions of the American Institue of Mining and Metallurgical Engineers,* vol. 185, pp. 741-748, 1949.

[99] A. S. Khanna, Introduction to High Temeprature Oxidation and Corrosion, 1st ed., Materials Park: ASM International, 2002.

[100] M. D. Bhandarkar and W. B. Lisagor, "Metallurgical characterization of the fracture of several high strength aluminum alloys, NASA-TP-1086," NASA Langley Research Center, Hampton, 1977.

[101] J. M. Kuchta and R. G. Clodfelter, "Aircraft mishap fire investigations," AF Wright Aeronautical Laboratories, Wright-Patterson AFB, 1985.

[102] M. Donachie and S. Donachie, Superalloys: A Technical Guide, ASM International, 2002.

[103] Department of Defense, "Military Handbook: Metallic Materials and Elements for Aerospace Vehicle Structures, MIL-HDBK-5H," Department of Defense, Wright-Patterson AFB, 1998.

[104] N. W. Hale, K. Lulla, H. W. Lane and G. Chapline, Wings In Orbit: Scientific and Engineering Legacies of the Space Shuttle., 2010, pp. 182-199.

[105] S. J. McDaniels, B. M. Mayeaux, R. W. Russell, T. E. Collins, S. R. Jerman, S. R. Shah and R. S. Piascik, "An overview of the Space Shuttle Columbia Accident from Recovery Through Reconstruction," *Journal of Failure Analysis and Prevention,* vol. 6, no. 1, pp. 82-91, 2006.

[106] P. H. Morton and W. M. Baldwin, "The scaling of titanium in air," *Transactions of the American Society of Metals,* vol. 44, pp. 1004-1029, 1952.

[107] I. O. Khomenko, A. S. Mukasyan, V. I. Ponomaryev, I. P. Borovinskaya and A. G. Merzhanov, "Dynamics of phase forming processes in the combustion of metal-gas systems," *Combustion and Flame,* vol. 92, no. 3, pp. 201-208, 1993.

[108] M. Jacobson, A. R. Cooper and J. Nagy, "Explosibility of metal powders, No. 6516," U.S. Dept. of the Interior, Bureau of Mines, Washington D.C., 1964.

Vita

Ngozi Ubani Ochoa earned her Bachelor of Arts degree in Spanish from The University of Texas at Austin in 2008. In 2013, she received a Bachelor of Science degree in Industrial Engineering from The University of Texas at El Paso (UTEP) and joined the doctoral program in Materials Science and Engineering at UTEP in 2014.

Dr. Ochoa was a Louis Stokes Alliance for Minority Participation (LSAMP) Bridge to the Doctorate fellow. While pursuing her degree, she interned at Vallourec in 2014 and at Holloman Air Force Base High Speed Test Track through TRAX in 2015. She also worked as a teaching assistant and is currently a co-op with Jacobs at NASA White Sands Test Facility.

Dr. Ochoa presented her doctoral research at the LSAMP Student Research Conference in 2014 and at the AeroMat Conference in 2016. She was co-author of a paper published in the Journal of Failure Analysis and Prevention and is currently submitting papers to the Journal of Space Safety Engineering.

Dr. Ochoa's research, "Investigation of Material Response to Atmospheric Re-Entry Exposure for Sub-Structural Ti-6Al-4V, Inconel 718, A-286 & Al 2024 Components Recovered from the Space Shuttle *Columbia* Accident," was supervised by Dr. Stephen Stafford.

Contact Information: <ncubani@miners.utep.edu>

This thesis/dissertation was typed by <Ngozi Chinoyerem Ubani Ochoa>.